Quantum Magnetic and Electronic Heterojunctions for Ultrasensitive Magnetic Sensing and Novel Electrical Rectification

By Shu Wang

B.S., Tongji University, 2008

A dissertation submitted in partial fulfillment of the

requirements for the degree of Doctor Philosophy

in Department of Physics at Brown University

Providence, Rhode Island

May 2018

The dissertation by Shu Wang is accepted in its present form

by Department of Physics as satisfying the

dissertation requirement for the degree of Doctor of Philosophy.

Date_____ _____

Prof. Gang Xiao, Advisor

Recommended to the Graduate Council

Date_____ _____

Prof. Brad Marston, Reader

Date_____ _____

Prof. Rashid Zia, Reader

Approved by the Graduate Council

Date_____ _____

Andrew G. Campbell, Dean of the Graduate School

The Vita of Shu Wang

Shu Wang was born on May 22, 1986 in Zhenjiang, China. She received her Sc.B. in physics from Tongji University in Shanghai, China in 2008. The research for this thesis started in 2011. **Her scientific publications include**:

1. "A Heterojunction composed by doped Mott Insulators" Shu Wang, Brad Marston and Gang Xiao, in preparation for submission to *Journal of Applied Physics.*
2. "Anomalous Hall effect and magnetic properties of FexPt100-x alloys with strong spin-orbit interaction" Qiang Hao, Wenzhe Chen, Shu Wang, and Gang Xiao, *Journal of Applied Physics* **122**, 033901 (2017).
3. "Piezo-strain induced non-volatile resistance states in (011)-La2/3Sr1/3MnO3/0.7Pb(Mg2/3Nb1/3)O3-0.3PbTiO3 epitaxial heterostructures" Yuanjun Yang, Z. L. Luo, Meng Meng Yang, Haoliang Huang, Haibo Wang, J. Bao, Guoqiang Pan, C. Gao, Qiang Hao, Shu Wang, Michael Jokubaitis, Wenzhe Zhang, Gang Xiao, Yiping Yao, Yukuai Liu, and X. G. Li, *Applied Physics Letters* **102**, 033501 (2013).
4. "Time-Resolved Energy-Momentum Spectroscopy of Electric and Magnetic Dipole Transitions in Cr3+: MgO" Sinan Karaveli, Shu Wang, Gang Xiao and Rashid Zia, *ACS Nano* **7(8)**, 7165 (2013).
5. "Controlling the conformations and transport of DNA by free energy landscaping" Elijah Shelton, Zhijun Jiang, Shu Wang, and Derek Stein, *Applied Physics Letters* **100**, 033501 (2012).

Honors and Awards:

1. The Forrest Award (for excellent work related to experimental apparatus), Physics Department, 2017
2. The Outstanding Thesis Award, Tongji University, 2008
3. Scholarship for Undergraduate Student Excellence, Tongji University, 2004-2008

Acknowledgement

First of all, I want to express my deep gratitude to my thesis advisor, Professor Gang Xiao. I really appreciated he gave me the precious opportunity to work in his group and supported me financially over my stay in Brown for graduation study. Professor Gang Xiao not only introduced me to the field of spintronics and helped me academically to be an independent scientist, but also showed me the methodology to become outstanding in any field. His advisor in both research and life will be great treasure for me. I would also like to thank Professor Brad Marston and Rashid Zia for their valuable insight discussion during the cooperation and reading my thesis and serving on my dissertation committee.

Next, I would like to thank my colleagues in our lab, Wenzhe Zhang, Qiang Hao, Wenzhe Chen, Guanyang He and Lijuan Qian for their assistance, discussion and advices in the lab. There is great fun to work with them all. Especially I need to thank Dr.Wenzhe Zhang for teaching me how to operate all the equipment in our lab and in the cleanroom and showing me the fabrication process.

I would also like to thank Michael Jibitsky, manager of the Micro Electronics Facilites for helping me in using all the photolithography and processing equipment in the cleanroom. He always showed up immediately once we reported any unusual during the processing and help us to resolve the problem. Without his dedicated work, my research cannot carry on at all.

Many friends in Brown have made my life full of happiness and memories. Thank you for the companion. I cannot list all the names here. I really appreciate knowing those excellent people and becoming friends with them.

In the end, I would like to thank my parents from the bottom of my heart. My whole life journey is fulfilled with their unselfish love and support. It is not about what they say and what they do. All of my accomplishment cannot be done without their respect and belief in me.

Contents

List of Figures

List of Tables

Chapter 1
Motivation and Outline

1.1 Motivation

Spintronics, the study of the intrinsic spin and its associated magnetic moment, has rapidly developed over the last few decades, not only in terms of the discovery of new physics but also the development of novel applications [1-3]. There is an important phenomenon in spintronics called the magnetoresistance effect, in which resistance can be changed by an external magnetic field. Many magnetic memory devices and sensors are built on this effect. In 1988 the discovery of giant magnetoresistance (GMR) [4] opened a new era for spintronics research. The GMR effect was discovered in the multilayer structures composed of alternating ferromagnetic material and nonmagnetic metals. In 1995, a large tunneling magnetoresistive (TMR) effect [5, 6] was discovered at room temperature in a structure of two ferromagnetic electrodes separated by a thin Al_2O_3 insulating layer. This came to be known as a magnetic tunnel junction (MTJ).

As a novel quantum mechanical device, the MTJ has attracted a huge amount of interest and motivated significant experimental and theoretical activities. In 2001, a theoretical work predicted that there would be extremely large TMR in MTJs using (001)-oriented MgO as the insulating barrier [7, 8]. In 2004, the room temperature experiment demonstrated that MTJs based on textured MgO barriers exhibited large TMR [9].

Nowadays MTJs have evolved from the simple three layer structure to dozens of layers. The specific structure and thickness of layers are tailored to the MTJ application, for example, for the purpose of large TMR, temperature reliability, high sensitivity and other applications. However, the performance of MTJs is still far from theoretical optimization and the fabrication of reliable high quality MTJs remains challenging.

With the development of thin film technology, thousands of MTJ devices can be easily fabricated on standard silicon wafers, thus enabling high spatial resolution and low fabrication costs. That is one of the reasons MTJ devices took a large market share in hard disk drive and magnetoresistive random access memory devices [10]. In the sensor market, the applications of MTJ sensing devices [11, 12] are limited by the sensibility. Recently, the ultrasensitive sensors with low fabrication cost are in an extremely high demand, driven by their medical applications. For example, the human heart generates a magnetic field in the range of 10^{-10} tesla. The normal electrocardiographic method, through measuring the electrical current generated by the human heart, relies on electrical leads through the human body. The contact leads can affect the diagnosis and make it obscure. Magnetocardiography, by measuring the magnetic field generated by human heart, does not require any physical contact and provides an accurate diagnosis. Current magnetocardiography technique is based on superconducting quantum interference devices. Obviously they are expensive and require low temperature environment. If the MTJ sensibility can reach 10^{-10} tesla, it can be applied in magnetocardiography and become an affordable home device.

The sensitivity of MTJs is related to TMR ratio and magnetic anisotropy. In order to achieve high sensitivity, scientists are currently focusing on a few approaches. First, multiple temperature annealing process is introduced to the sensor fabrication. Usually one-step high-temperature annealing is necessary to achieve high TMR ratio. A secondary low-temperature annealing using a relatively small magnetic field, in the perpendicular direction to the first annealing, can be used to reduce the anisotropy of the free layer caused by the first annealing. Now, even three-step annealing process has been implemented. At the same time, scientists are looking for new materials or synthetic layer structures, with intrinsic low magnetic anisotropy, to be applied in the free layer. In 2013, Tohoku University used amorphous $Co_{70.5}Fe_{4.5}Si_{15}B_{10}$ ferromagnetic material in the free layer and employed a double annealing process. They achieved 40%/Oe sensitivity while maintaining the linearity of the magnetoresistance curve without the bias field [13]. The development of fabrication technique enables the study of the sensors with perpendicular magnetic anisotropy (PMA) in the free layer. The sensors with PMA always show good linearity if characterized by planar magnetic field and their sensitivity can be easily modified by changing the thickness of the free layer. However, the discovery of new materials in MTJs and the improvement for fabrication technology is still costly and time-consuming. More effective and direct approaches are needed for realizing ultrasensitive sensing. One of our objectives is to improve the magnetic sensibility by reducing the magnetic anisotropy of the free layer through a novel magnetic amplifying components based on flux concentrators.

Thin film technology plays a very important role, not only in the manufacturing of new devices, like GMR and MTJ devices, but also in the exploration of new fundamental physics. Thin film technique, in our case the high vacuum magnetron sputtering, can help us in the aspects of material synthesis and creation of any artificial heterojunction structures.

Scientists have studied the bulk properties of doped Mott insulator material for decades, for example, high temperature superconductivity and magnetoresistivity. In the heterojunctions composed by doped Mott insulators, the artificial interface with this strong correlated electron system may present a much more interesting phenomenon [14-17]. A theoretical work [18] predicted the solar cell device based on dope Mott insulators have much higher quantum efficiency. The classical solar cell devices have low quantum efficiency. Only the amount of energy of the band gap is absorbed to create one electron-hole pair. The extra energy carried by photons is actually wasted as heat. However, in Mott system one photon absorbed can create more than one electron-hole pair because of the interaction of strong correlated electrons. In addition, semiconductor devices only work in a low frequency because the mechanism is based on charge diffusion. Mott devices have the potential to work at a much higher frequency because of the intrinsic short time scale for strong correlated systems. The conventional p-n junction has been well studied because of highly developed semiconductor industry. However, p-n junctions composed of doped Mott insulators are still in the preliminary stage and a huge difference is anticipated. That's the reason why we have made a major effort to fabricate

high quality epitaxial Mott-insulator heterojunctions and want to demonstrate its potential for future applications in electronics and in solar rectification devices.

1.2 Outline

In this dissertation, we will present two achievements both using the high vacuum magnetron sputtering system and the thin film technique. First, we have increased the magnetic sensing capability of MTJ sensors significantly by introducing magnetic flux concentrators. The flux concentrator is a "soft" magnetic material with certain geometry working directly on the free layer of MTJ sensors as a magnetic field amplifier. A special "soft" magnetic material ($Co_{88}Nb_8Zr_4$) in the thin film form has been successfully fabricated utilizing our high vacuum magnetron sputtering technique, and characterized using magnetometry measurement. The "soft" magnetic concentrators have been added to the MTJs using lithography technique. Furthermore, we have included additional magnetic concentrators outside of the thin film MTJ devices. With these approaches, we have improved the magnetic sensing capability significantly.

Second, based on the same magnetron sputtering technique, we have successfully developed high-quality heterojunctions of epitaxial $La_{1.9}Sr_{0.1}CuO_4$ (LSCO) thin films on a 0.5wt% Nb doped $SrTiO_3$ (NSTO) single-crystal substrate. The heterojunction shows good rectification and expected temperature dependency. We have investigated the capacitance of the junctions over a broad frequency range under different bias voltages. The results were explained by considering the LSCO/NSTO junctions as a Schottky

barrier with deep-level impurities. This doped Mott insulator system is quite different from traditional p-n heterojunctions and exhibited interesting interfacial properties.

This thesis is organized as follows.

Chapter 2 describes all the fabrication and characterization techniques required for MgO-barrier magnetic tunnel junction devices. The fabrication techniques include substrate oxidization by oxygen furnace, deposition by high-vacuum magnetron sputtering system, processing techniques using ion milling, photolithography and high temperature magnetic annealing. The characterization techniques include x-ray diffraction (XRD), atomic force microscope (AFM), physical property measurement system (PPMS), and vibrating sample magnetometer (VSM).

Chapter 3 describes the basic physics concepts behind the MgO-barrier MTJs and its sensor devices. All the details of the experiment techniques and procedures to produce high-quality MTJ device are reviewed in the fabrication sequence. In the end, the fabricated MTJ device is characterized.

Chapter 4 presents the further improvement of magnetic sensors based on our MTJs. The "soft" magnetic material $Co_{88}Nb_8Zr_4$ as flux concentrator is introduced to our sensor design based on the COMSOL simulation. The fabrication method of this new material is presented in detail. Then, the preliminary test of combining this new design with a secondary flux concentrator using the material of Conetic ($Ni_{77}Fe_{14}Cu_5Mo_4$) is presented.

Chapter 5 describes a new system consisting of a $La_{1.9}Sr_{0.1}CuO_4$ thin film on a 0.5wt% Nb doped $SrTiO_3$ single-crystal substrate also fabricated by our high vacuum magnetron sputtering system. We conducted theoretical simulations and experimental characterizations of these heterojunctions. The synthesis of heterojunctions of $La_{1.9}Sr_{0.1}CuO_4$ thin film on 0.5wt% Nb doped $SrTiO_3$ is reported in detail. This includes how to build the high-temperature substrate holder inside our sputtering system. The electrical transport and capacitance properties are investigated and discussed.

Reference

1. S. Wolf, D. Awschalom, R. Buhrman, J. Daughton, S. Von Molnar, M. Roukes, A. Y. Chtchelkanova and D. Treger, Science **294** (5546), 1488 (2001).

2. I. Žutić, J. Fabian and S. D. Sarma, Reviews of modern physics 76 (2), 323 (2004).

3. B. Schrag, X. Liu, W. Shen and G. Xiao, Applied physics letters **84** (15), 2937 (2004).

4. M. N. Baibich, J. M. Broto, A. Fert, F. N. Van Dau, F. Petroff, P. Etienne, G. Creuzet, A. Friederich and J. Chazelas, Physical review letters **61** (21), 2472 (1988).

5. J. S. Moodera, L. R. Kinder, T. M. Wong and R. Meservey, Physical review letters **74** (16), 3273 (1995).

6. T. Miyazaki and N. Tezuka, Journal of Magnetism and Magnetic Materials **139** (3), L231-L234 (1995).

7. W. Butler, X.-G. Zhang, T. Schulthess and J. MacLaren, Physical Review B **63** (5), 054416 (2001).

8. J. Mathon and A. Umerski, Physical Review B **63** (22), 220403 (2001).

9. S. S. Parkin, C. Kaiser, A. Panchula, P. M. Rice, B. Hughes, M. Samant and S.-H. Yang, Nature materials **3** (12), 862 (2004).

10. S. Parkin, K. Roche, M. Samant, P. Rice, R. Beyers, R. Scheuerlein, E. O'sullivan, S. Brown, J. Bucchigano and D. Abraham, Journal of Applied Physics 85 (8), 5828 (1999).

11. J. E. Lenz, Proceedings of the IEEE **78** (6), 973 (1990).

12. P. Ripka, Journal of Magnetism and Magnetic Materials **320** (20), 2466 (2008).

13. D. Kato, M. Oogane, K. Fujiwara, T. Nishikawa, H. Naganuma and Y. Ando, Applied Physics Express **6 (10)**, 103004 (2013).

14. A. Ohtomo, D. Muller, J. Grazul and H. Y. Hwang, Nature **419** (6905), 378 (2002).

15. E. Dagotto, SCIENCE **318** (5853), 1076 (2007).

16. J. Heber, Nature News **459** (7243), 28 (2009).

17. J. Mannhart and D. Schlom, Science **327** (5973), 1607 (2010).

18. E. Manousakis, Physical Review B **82** (12), 125109 (2010).

Chapter 2
Experimental Techniques

The principal experimental methods and techniques applied in our experiment are introduced in this chapter. The fabrication techniques include substrate oxidization by oxygen furnace, deposition by high vacuum magnetron sputtering system, processing techniques using ion milling, photolithography and magnetic annealing. The characterization techniques include x-ray diffraction (XRD), atomic force microscope (AFM), physical property measurement system (PPMS) and vibrating sample magnetometer (VSM).

2.1 Oxygen Annealing Furnace

Substrate is very important for generating high quality thin film devices. For our MTJs fabrication, the substrate should be very flat to make sure the multilayer structure built on it can achieve good roughness. It also has to be a good insulator so that individual junctions can be electrically isolated from each other. The fabrication and annealing process will also require a substrate with good thermal conductivity, adhesion property and temperature stability. Silicon wafer has been selected considering the cost and the availability. However, as we just mentioned, silicon is not a good insulator. Therefore,

the thermal oxidization is introduced here to create a good insulating layer of SiO_2 on silicon wafer.

For our heterojunctions composed of doped Mott insulator, the requirement for substrates is even more strict. The single crystal substrate $SrTiO_3$, with pure TiO_2 termination, works as a template for the epitaxial growth. However, the commercially available single crystal substrate always has certain contamination, oxidization and a mixture surface of TiO_2 and SrO. Therefore the chemical and temperature treatment is necessary. Thermal annealing is very critical for our heterojunction growth. More details will be presented in chapter 5.

Oxygen Annealing Furnace is used to anneal samples with temperature and gas flow control. The 3-zone temperature controllers can provide very good temperature uniformity over the whole chamber. Different gases can be chosen and the gas flow is controlled by a mass flow controller. The annealing time and temperature depend on the experiment requirements. For example, about 1.5μm thickness of SiO_2 insulating layer can grow on one-side polished Si wafers at 1150^{o}C with 0.5sccm O_2 flow for 24 hours. SiO_2 starts to grow as the oxidization reaction happens. There will be less oxygen at Si/SiO_2 interface and oxidization reaction happens at an increasingly slow rate. Oxygen furnace is used to create perfect surface terrace structure of $SrTiO_3$. The annealing process is at 950^{o}C in air and the annealing time is sensitively related to the substrate miscut.

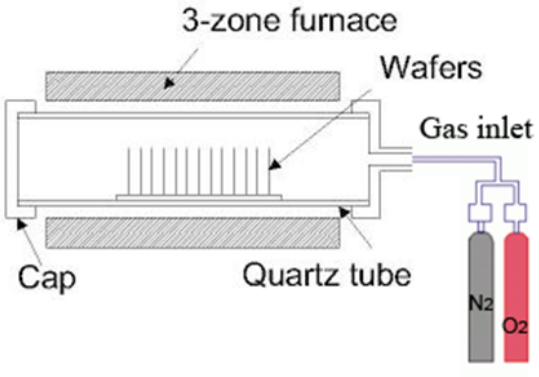

Figure 2.1 Schematic drawing of a high-temperature oxidation furnace system

2.2 High Vacuum Magnetron Sputtering

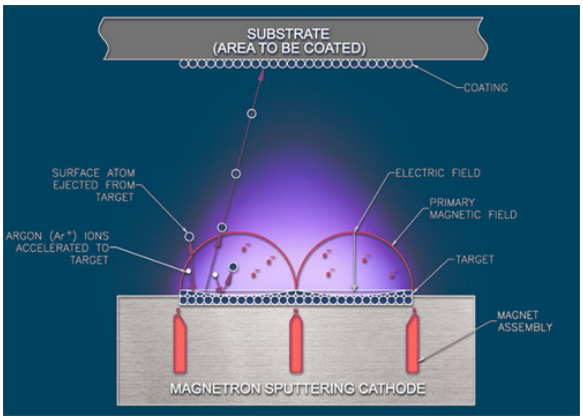

Figure 2.2 Schematic drawing of the magnetron sputtering process (DC) (image from Wikipedia)

Sputtering technology [1] is a physical vapor deposition process, which is widely used in industry for mass production of high quality thin films. The deposited material is released from a solid source at the temperature far below the vaporization point. This technique can be used to deposit metals, semiconductors and insulators. The system normally includes a high vacuum chamber, a gun where the target material is placed and substrate holders. The substrate holder can either be sitting in the ambient environment, or be heated or cooled for specific purposes. For example, in MTJs deposition the substrate

holder is just sitting inside the chamber while in $La_{1.9}Sr_{0.1}CuO_4$ deposition the substrate holder has to be heated up.

DC diode sputtering is the most well-known sputtering configuration. The schematic diagram of DC sputtering system is similar to Figure 2.2 except the permanent magnets. The material to be sputtered is called the target and is negatively biased (cathode). The substrate is positively biased (anode). When the applied voltage between the cathode and anode reaches a certain threshold, the inert gas, Argon, in the chamber will ionize and become plasma form. The Ar^+ will be accelerated by the electric field towards the cathode and its momentum will be transferred to the target material atom. The collision will cause not only the release of the target material but also the electrons emitted, and these electrons can further help ionization of Ar. In order to sustain this ionization process, a large space between cathode and anode and a relatively high sputtering pressure are needed. Obviously DC sputtering cannot apply to insulator target because the positive charge will quickly build on the surface of the insulator target and therefore no secondary emission of electrons will be released.

If a magnetic field is applied along the target surface, the electron emitted by the collision between Ar^+ and the target will travel in a spiral path due to the Lorentz force $v \times B$. The travel distance of electrons has been dramatically increased and so as the possibility of the collision with Ar. This process is called magnetron sputtering, which is schematically shown in Figure 2.2. Magnetron sputtering can happen in a much lower sputtering pressure and produce thin film with fewer impurities.

The MgO layer in MTJs is only about 2nm. Any impurity can damage the junction, resulting in no tunneling effect. Low sputtering pressure is intended to produce a high-quality MgO barrier. As an insulator target, the sputtering of MgO can be realized using a radio-frequency power supply with magnetron sputtering mechanism. In MTJ structures there are different magnetic materials and non-magnetic materials. The target thickness of non-magnetic materials e.g., Ruthenium is 1/8 inch while the magnetic material e.g., $Co_{50}Fe_{50}$ is 1/16 inch. If the magnetic target is too thick, the magnetic field cannot penetrate through the target. Considering the mechanism of magnetron sputtering, the low possibility of collision will make the ionization challenging and plasma may not sustain.

2.3 Thermal Evaporation

Thermal Evaporation is also a physical vapor deposition technique. The source material is heated up from solid to vapor phase and travels freely in the vacuum chamber. The substrate is sitting at a much lower temperature using some cooling system. The vaporized source material will condense on the substrate once it reaches the cold substrate surface. The low pressure will not only help the material transition from solid phase to vapor phase but also give rise to less contamination, longer mean free path and high deposition rate. There are two methods to evaporate the source material. One is using a focused electron beam to heat up the source and the other is using large current. Therefore, there are two types of evaporators, E-beam evaporator and Resistive

evaporator. In our MTJs deposition, an e-beam evaporator is used to make the top electrodes composed by 10nm Cr or Ti and 80nm Au.

2.4 X-ray Diffraction

X-ray diffraction (XRD) is an efficient technique which is used to get information about crystal structures of the material without damaging it. For multilayer thin film structure, XRD can even measure the sublayers which are buried underneath [2]. The signature crystal peaks and their relative intensities from XRD patterns are the information source where you can explore the material type, lattice information and even impurities.

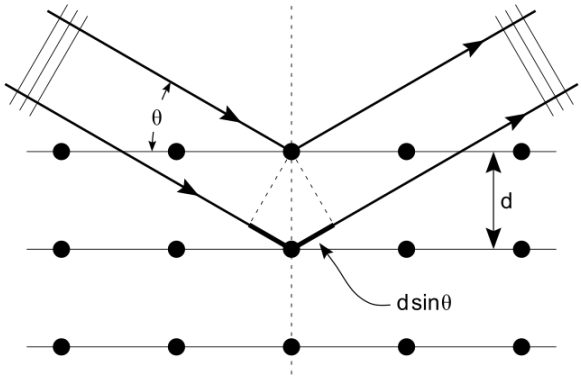

Figure 2.3 Schematic drawing of the principles of XRD (image from Wikipedia).

The basic principal of XRD is shown in Figure 2.3. The monochromatic X-ray beam with wavelength λ is incident on the crystalline material. The interference will only happen when the crystal lattice spacing d and the incident beam angle satisfies Bragg's law, $n\lambda=2d\sin\theta$. Therefore, the diffracted waves are constructively interfering and show characteristic peaks of the crystal.

The most common measurement is called θ-2θ scan in which the rotation between the sample stage and detector is in θ-2θ relation. During the XRD measurement, x-rays with a single wavelength, usually K_α line of copper, are collimated and injected into the sample. The diffracted x-ray signal will be collected using a photo detector. Before the measurement, the incident x-ray beams need to be carefully aligned with the sample surface by Z scan and rocking scan. The incident X-ray beam only has limited width and Z scan can adjust the sample position to make sure the center of the x-ray beam hits the sample surface. Rocking scan is used to rotate the sample to find the position where the sample surface is in parallel with x-ray beams. Otherwise, the characteristic peaks can be missed or off the position, making results obscure. If the θ-2θ scan happens in the low angle ($\theta<5^0$), the characteristic peaks are due to the interference between reflections from the top and bottom surfaces, which can be used to obtain film thickness, interface roughness, film density and some other information.

In MTJs fabrication, XRD is used to calibrate film thickness and check the crystalline structures for sublayers. In the epitaxial film $La_{1.9}Sr_{0.1}CuO_4$ on (001) single-crystal Nb doped $SrTiO_3$ substrate deposited at high temperature, XRD plays an even more important role. First, it is used to check the purity of $La_{1.9}Sr_{0.1}CuO_4$ target compound. Second, the epitaxial growth of $La_{1.9}Sr_{0.1}CuO_4$ on the substrate is checked using XRD. Figure 2.4 is an example of XRD pattern of an epitaxial film $La_{1.9}Sr_{0.1}CuO_4$. XRD is also used to measure film thickness to calculate deposition rate. In order to get the film thickness, we can use photolithography method with a stylus profilometer. The

photoresist has to be applied on the sample surface before the deposition. However, when the sample size is too small to go through the photolithography or the deposition happens at high temperature and all the photoresist becomes hardened and impossible to remove, the low angle X-ray diffraction becomes the only method. Figure 2.5 is an example of low-angle scan which the film thickness is revealed and the corresponding deposition rate can be calculated.

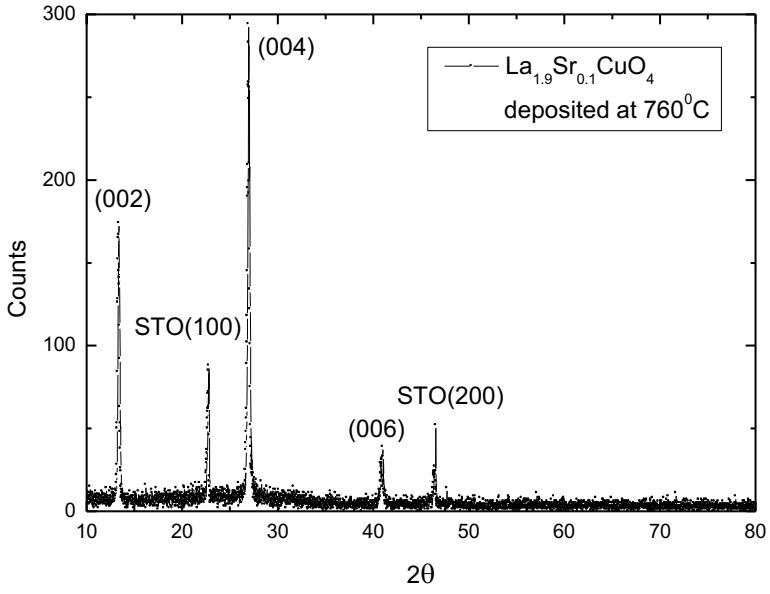

Figure 2.4 An example of XRD pattern. The sample is $La_{1.9}Sr_{0.1}CuO_4$ on single-crystal Nb doped $SrTiO_3$ substrate. The pattern means the $La_{1.9}Sr_{0.1}CuO_4$ is epitaxial.

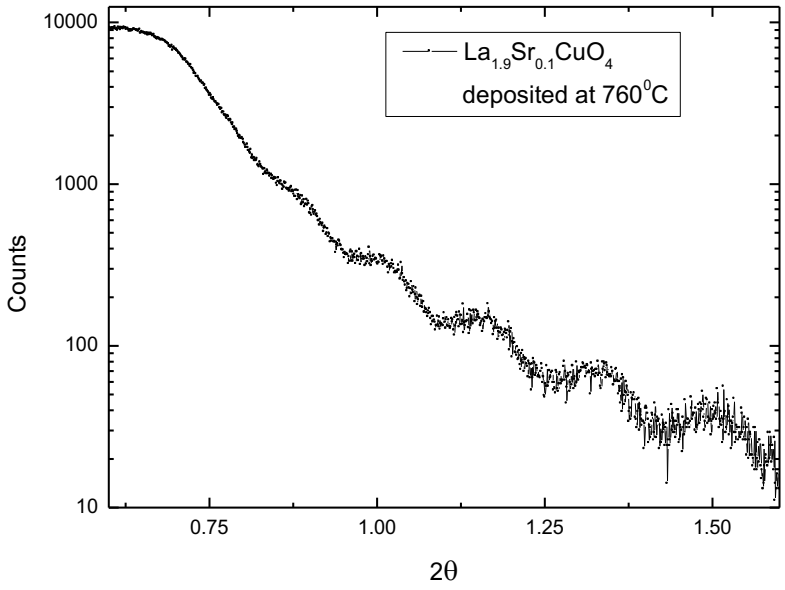

Figure 2.5 An example of low angle scan which reveals the film thickness. The thickness cannot get by traditional photolithography method because the deposition happens at high temperature.

2.5 Atomic Force Microscope

Atomic force microscope (AFM) is a microscopy technique which is used to explore sample surface information. The basic components of AFM usually include a force detective system, a laser transition system, and a feedback and control system. The force detective system usually contains a sensitive cantilever spring and a fine probe tip. The interaction force between the tip and the sample surface can cause the cantilever spring to bend. In order to measure the bending information, the laser transition system is needed. The basic configuration is that a laser beam is injected onto the cantilever and its reflected beam is captured by a position-sensitive photodetector. So the change of the position for the cantilever is recorded by the photodetector and then interpreted as the surface information. During the measurement, if the tip was scanned at the same height,

this may damage the tip or sample if any collision happened. Therefore, the feedback and control system is introduced. The sample under measurement is sitting on the sample stage which actually is a piezoelectric transducer. During the scan, if the tip feels too much force due to the small separation between tip and sample surface, the feedback introduced by the piezoelectric transducer can move the sample slightly farther away to protect both tip and sample.

Compared to scanning electron microscope and transmission electron microscope, AFM has the certain advantages. First of all, there is no sample preparation. There is no requirement for the sample to be conducting or not. Second, the measurement happens at the ambient environment and no vacuum environment is needed. Mostly importantly, there is no damage to samples and samples can still be used for future measurement. We will use AFM to check the surface structure of Nb doped $SrTiO_3$ substrate after the surface treatment and make sure pure TiO_2-terminated surface is obtained. One example of AFM scan of Nb doped $SrTiO_3$ substrate before the treatment has been shown in Figure 2.7.

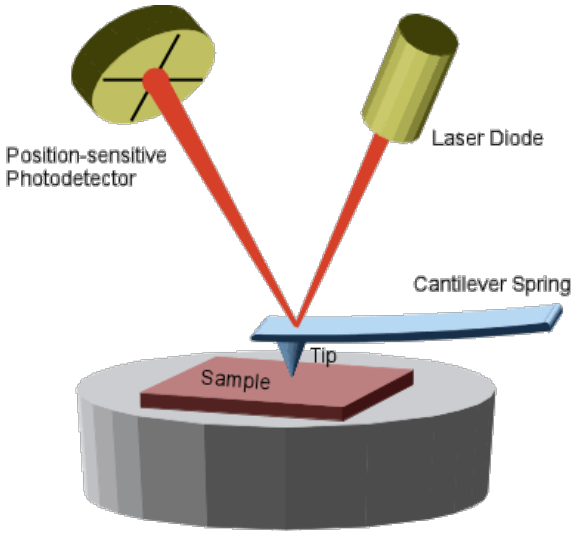

Figure 2.6 Schematic drawing of the AFM system.

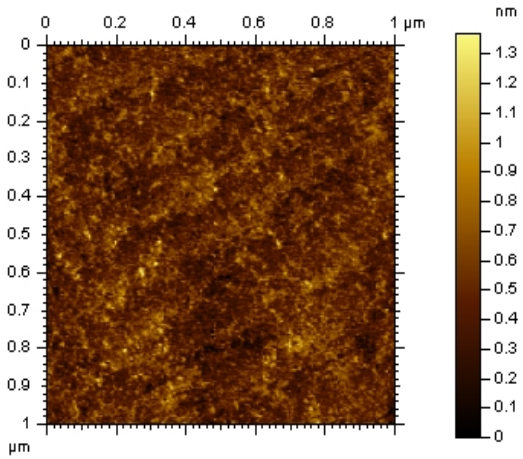

Figure 2.7 An example of an AFM image on a Nb doped SrTiO3 substrate before surface treatment.

2.6 Physical Property Measurement System

The physical property measurement system manufactured by Quantum Design is powerful modern equipment. It can perform a variety of automated measurement. It can provide the measurement environment with any temperature from 1.9K to 390K and magnetic field between ±9Tesla. It includes the functions of VSM Option (VSM), AC

Susceptibility &DC Magnetization Option (ACMS), Ultra Low Field Option (ULF), Electrical Transport Option (ETO), Resistivity Option and Thermal Transport Option (TTO).

In this section, the general principal and operation of PPMS will be discussed. Thera are four main parts including sample chamber, control station, compressor and the cooling system. The sample chamber and the control station are shown in Figure 2.8.

Figure 2.8 The real image of PPMS including the sample chamber and controller station only (from PPMS manual).

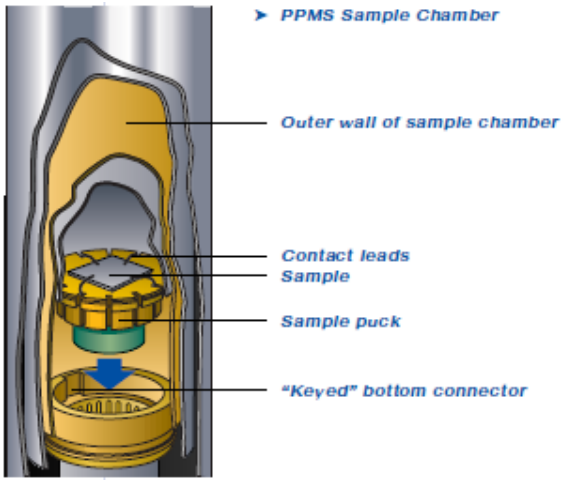

Figure 2.9 The drawing of the sample chamber in PPMS (from PPMS manual).

During the transport measurement, the sample is mounted on the puck shown in Figure 2.9. The puck is delivered to the bottom of the chamber and then connected to the bottom connector using a sample guide rod. The measurement-ready position is achieved when the bump on the puck matches the notch on the bottom connector. This feature provides the convenient access to the electrical leads, making automated measurement possible.

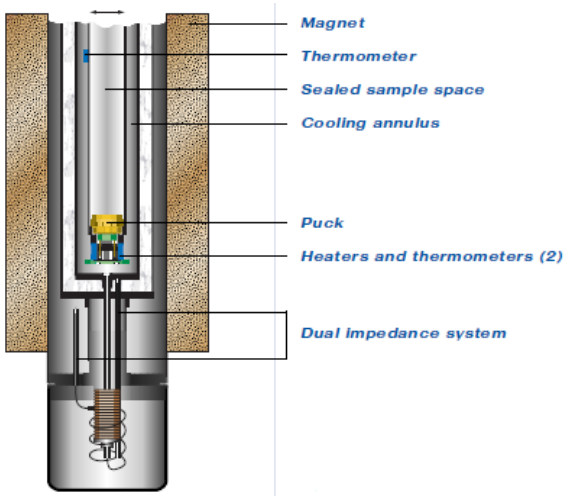

Figure 2.10 The cut off view showing PPMS sample chamber (from PPMS manual).

The temperature control is realized using the cooling annulus and heater mounted right next to sample puck. The vacuum pump will draw certain amount of helium into the annulus and the heater will heat the sample to right temperature through the dynamic feedback of thermometers. The helium is circulated in the annulus. Most of the helium gas is used when the system is first started and the liquid helium is generated. The helium can sustain the measurement for a long period, sometimes even over a year. That's why the system is named as EverCool. It has the continuous operation down to 1.9K and the total time is about 3 hours depending on the measurement. The magnetometer can

provide the longitudinal magnetic field up to ±9Tesla and the sensitivity down to 10^{-8} emu. Even though it only provides the magnetic field in longitudinal direction, it provides the different sample mounting fixtures. During the magnetic measurement, the sample surface can be mounted parallel or perpendicular to the magnetic field, which actually resolves the problem of single-axis magnetic field.

2.7 Photolithography

Photolithography is a technique widely used in the modern semicondcutor industry. Through spin coating, a continuous thin film of photoresist is transferred onto wafer surface. Then the wafer is exposed to UV light through photomasks. The exposed or unexposed area can be dissolved in a specific developer, depending on the type of photoresists. There are two types of photoresist, positive and negative. The UV exposure area of the positive photoresist will become polymerized and soluble in the chemical developer. The negative photoresist has the opposite property. The UV exposure area will become insoluble and the area protected by the mask will be dissolved in the corresponding developer. There are two types of photomasks, hard and soft. The hard photomask provides better accuracy of the images transferred. However the minimum feature size the photo lithography can deliver is restricted by the limit of light diffraction. The normal UV photolithography using wavelengths between 370nm and 410nm has a resolution of 1μm and some deep UV may have a resolution of 200nm.

Photo lithography is used throughout all our projects. It will help us to change the continuous thin film into isolated measurable micro-size devices. The photoresist, AZ5214E manufactured by Clariant, can be used as either positive or negative. But each

type requires different soft baking temperature, hard baking temperature and UV exposure time. The feature size we are generating is usually a few micrometers. They are invisible to the naked eye. In order to get the accurate patterns, photomicroscope and stylus profilometer, like Dektake, are required during the photolithography process.

2.8 Ion Milling

Ion milling is a physical etching process [3]. It is a widely used etching method because of its high directionality and low material selectivity. Compared to reactive ion etching, ion milling only employs Argon gas and has a relatively high etching rate. In our work, photo lithography can generate a photoresist template on the sample surface and ion milling is actually used to etch that template into the sample.

Ion milling machine is a vacuum system usually including the processing chamber and the pumping system. During the processing, electrons are introduced by a hot filament and are accelerated towards the anode grid. Impacted by the electrons, inert gas atoms (usually Argon) start to ionize. The positively charged Ar^+ ions move towards the sample under an accelerating potential, usually 500-1000V. Before the Ar^+ ions reach the sample, they have to be neutralized using a neutralizer to reduce the damage which is possibly introduced by charged atoms. When the neutralized Ar atoms with large momentum hit the sample surface, the material atoms are knocked out and the sample gets etched. A schematic drawing of an ion beam etcher is shown in Figure 2.11. As we mentioned, ion milling etching is a much stronger etching tool compared to reactive ion beam etching in terms of etching rate and the material it is able to etch. It may cause the

material oxygen deficiency or sub-stoichiometric surface, which we experienced for the heterojunction of LSCO/NSTO. The major problem we experienced for MTJs with ion milling is recoating or redeposition [4]. If the removed material is redeposited on the sidewall of the tunnel barrier, it can result in the shortage of the junction. In order to avoid or minimize this problem, the sample is mounted on a rotating fixture with an adjustable angle to the incident beam. In Figure2.11, the ion beam is perpendicular to the sample surface (wafer platen). In our process the sample is placed on a rotation stage and incident ion beam is injected onto the sample surface at a relative low angle. The method is effective to clean the sidewall and is very important to generate high quality MTJs.

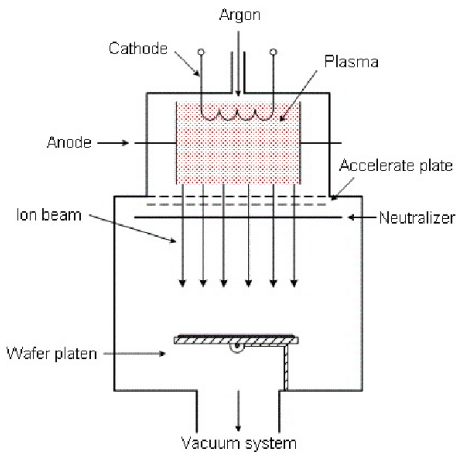

Figure 2.11 Illustration of an ion beam etching system.

2.9 Magnetic Annealing Station

Magnetic annealing is very important for our sample fabrication. The magnetic annealing is applied to remove the lattice disorder and crystallize the CoFeB layer using MgO (001) layer as a template. After magnetic annealing, the exchange coupling due to the synthetic

antiferromagnetic layers is achieved and can provide the pinning force for the bottom MTJs.

The annealing station is designed and built by ourselves shown in Figure 2.12. The chamber pressure can reach down to 10^{-6} Torr using a turbo pump. There is a sample holder box placed inside of two permanent magnets. A uniform magnetic field around 0.45 Tesla parallel to the ground surface is generated by the magnets over the sample box. The temperature of the sample box can be heated up to 400^{0}C. Annealing study is popular for MTJs because all the parameters of MTJs as TMR ratio, coercivity, sample stability, sensitivity and noise level in MTJs, can be easily modified through annealing procedures.

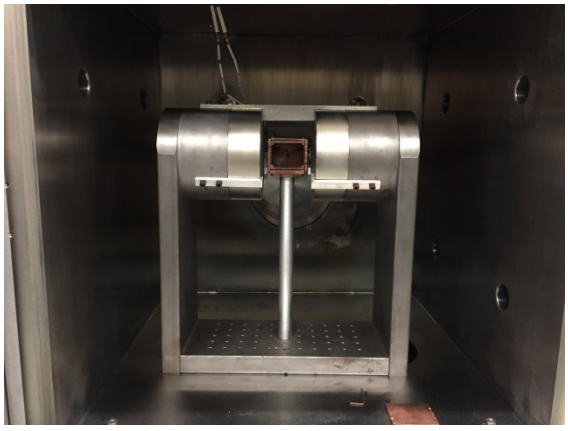

Figure 2.12 The image of Annealing Station

2.10 Vibrating Sample Magnetometer

Vibrating sample magnetometer (VSM), first invented in 1955, is an effective method to measure magnetic properties of the material [5]. The sample is sitting in a uniform magnetic field generated by the electromagnets. The movement of the sample will cause

the change of magnetic flux detected by the pick-up coils and therefore induce a small voltage. If the sample vibrates at certain frequency, the induced voltage will have the same frequency and can be captured by a lock-in amplifier. Basic VSM model provides a reference sample and the magnetization information of measured sample can be calculated by comparison. More advanced model has the reference sample placed on the same vibrating rod and the absolute magnetization can be output simultaneously.

Reference

1. K. Wasa and S. Hayakawa, (1992).

2. V. Holy, T. Baumbach and U. Pietsch, High-resolution X-ray scattering from thin films and multilayers, (1999).

3. P. G. Glöersen, Journal of Vacuum Science and Technology 12 (1), **28** (1975).

4. Y. Fu, N. K. A. Bryan, O. Shing and N. Hung, The International Journal of Advanced Manufacturing Technology **16** (12), 877 (2000).

5. S. Foner, Review of Scientific Instruments 27 (7), 548 (1956).

Chapter 3
Magnetoresistive Sensors Based on Magnetic Tunneling Junctions

In this chapter we will first review the basic physics concepts about MgO-barrier MTJ. The key procedures to produce high-quality MTJs are presented based on our decades of experience in the experimental sequences. In the end, we will characterize our MTJ sensors and explore the possibility of generating high-performance sensor devices.

3.1 Theoretical Background

3.1.1 Tunnel Magnetoresistive Effect

Tunneling magetoresistance is a quantum effect which happens in magnetic tunnel junction (MTJ). The MTJs are composed of two ferromagnetic layers separated by an insulator layer. If the magnetization directions of these two ferromagnetic layers are in parallel, the junction resistance is in the low resistance state R_p. If the magnetization directions of these two ferromagnetic layers are changed to the antiparallel state through an external magnetic field, the junction resistance is changed to the high resistance state R_{ap}. TMR is defined as $\frac{R_{ap}-R_p}{R_p}$. TMR is a very important and most straightforward parameter to characterize MTJs.

In 1975, tunnel magnetoresistance effect was first discovered by a French scientist, M. Jullière, in Fe/Ge-O/Co-junctions at 4.2 K. He achieved 14% TMR in low temperature

[1]. The first improvement happened in 1991. The 2.7% TMR was found at room temperature by the Japanese scientist, Terunobu Miyazaki [2]. In 1994, 18% TMR at room temperature was discovered in junctions composed of iron separated by amorphous aluminum oxide by Miyazaki et al. By the same time Moodera, *at el.*, discovered a large TMR effect using CoFe and Co as the ferromagnets at room temperature [3, 4]. In 2001, scientists theoretically predicted the high TMR effect in the junction composed by iron as the ferromagnet and crystalline MgO as the insulator [5, 6]. In the same year the experiment of Fe/MgO/FeCo(001) MTJ was reported and verified the high TMR effect [7]. After decades of efforts, TMR has been improved to over 1000% and devices based on that are widely used in modern industries, like MRAMs and sensor devices.

Magnetic tunnel junction is manufactured through thin film technologies. In industry, it is usually fabricated by magnetron sputtering technique while in the research lab molecular beam epitaxy, pulsed laser deposition and some other high-cost equipment are also applied to develop MTJs.

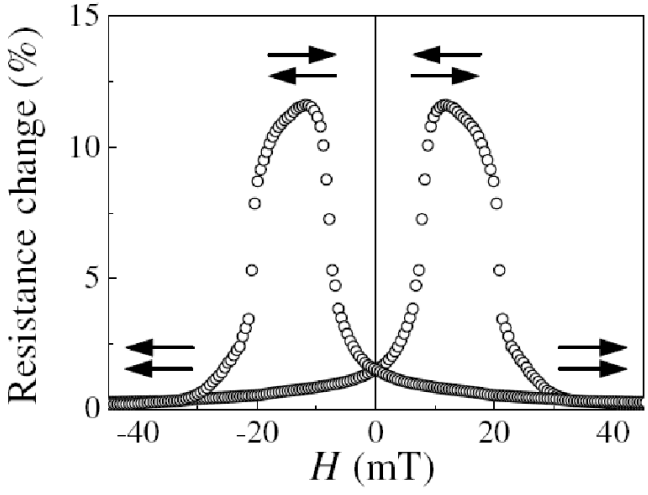

Figure 3.1 The first discover of large TMR effect at room temperature in the MTJ structure of $CoFe/Al_2O_3/Co$ in 1995[4].

3.1.2 Julliere's Model and Spin Dependent Tunneling

As we mentioned before, in 1975, TMR effect was discovered by French scientist, M. Julliere, in Fe/Ge-O/Co-junctions at 4.2 K. Julliere proposed an effective and straightforward model to interpret his results. He considered that the tunneling current is contributed from two spin-dependent channels [1]. One is the spin-up electrons and the other is the spin-down electrons. During the tunneling process, the spin of electrons is conserved. The electron in spin-up or spin-down state can only tunnel into the available corresponding states.

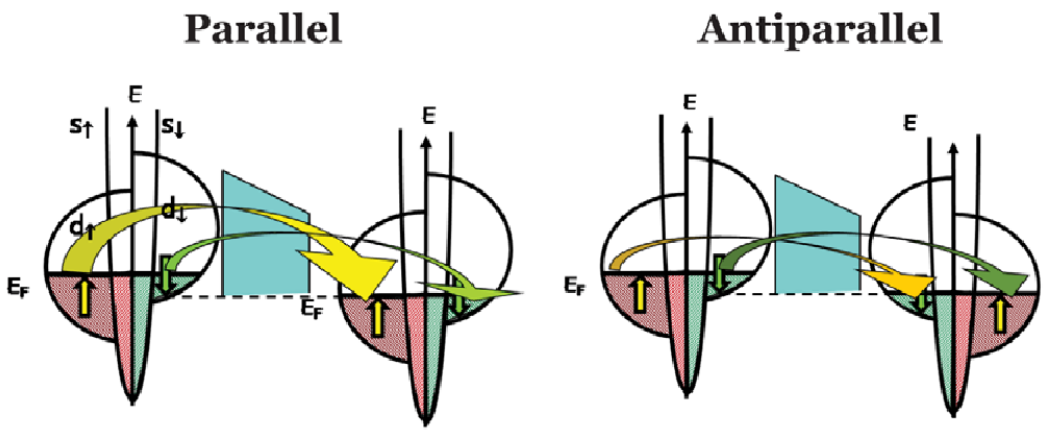

Figure 3.2 The tunneling process in MTJs (a) when magnetizations of two ferromagnetic electrodes in are parallel and (b) when magnetizations of two ferromagnetic electrodes are in antiparallel directions.

Based on the assumption of two spin-dependent channels, Fermi's golden rule and Fermi-Dirac distribution, the total tunneling probability can be written as:

$$T_{\uparrow\uparrow(P)} \sim D_{1\uparrow} D_{2\uparrow} + D_{1\downarrow} D_{2\downarrow}$$

Where $D_{\alpha\uparrow}$ is defined as the density of states at Fermi level for the majority spin state and $D_{\alpha\downarrow}$ is the density of states at fermi level for the minority spin state.

Therefore, the tunneling probability for antiparallel state can be expressed as:

$$T_{\uparrow\downarrow(AP)} \sim D_{1\uparrow}D_{2\downarrow} + D_{1\downarrow}D_{2\uparrow}$$

The conductivity σ is proportional to the tunneling probability T.

$$TMR = \frac{R_{AP} - R_P}{R_P} = \frac{\frac{1}{\sigma_{\uparrow\downarrow}} - \frac{1}{\sigma_{\uparrow\uparrow}}}{\frac{1}{\sigma_{\uparrow\uparrow}}} = \frac{\sigma_{\uparrow\uparrow} - \sigma_{\uparrow\downarrow}}{\sigma_{\uparrow\downarrow}} = \frac{(D_{1\uparrow} - D_{1\downarrow})(D_{2\uparrow} - D_{2\downarrow})}{D_{1\uparrow}D_{2\downarrow} + D_{1\downarrow}D_{2\uparrow}} = \frac{2P_1P_2}{1 - P_1P_2}$$

Where P_α is the corresponding spin polarization for each ferromagnetic electrode. The definition for spin polarization is:

$$P_\alpha = \frac{D_{\alpha\uparrow} - D_{\alpha\downarrow}}{D_{\alpha\uparrow} + D_{\alpha\downarrow}}$$

Julliere's Model works quit well for interpreting TMR effect. It also gives a good estimation of the maximum TMR which is possible to achieve in MTJ of 3d ferromagnets. However, it is just a simple model because it only considered the magnetizations of the two ferromagnetic electrodes and treated electron spin conserved.

3.1.3 Incoherent Tunneling and Coherent Tunneling

Julliere's model considered the tunneling probability only dependent on the spin polarization of the ferromagnetic electrodes. Furthermore, spin polarization is simplified to be only dependent on the spin-dependent densities of states on Fermi level in Julliere's model. This will result in completely incoherent tunneling. In reality, the spin polarization of Co and Ni is negative according to the band structure calculation, however it is experimentally observed positive. It actually shows the tunneling probability depends

on the each Bloch state symmetry. To calculate tunneling probability, we have to consider not only the spin polarization of ferromagnetic electrodes, but also the symmetry of Bloch waves in two ferromagnetic layers and the symmetry of evanescent states in the barrier.

Figure 3.3(a) shows the tunneling process for amorphous Al-O barrier. There is no crystallographic structure for amorphous Al-O. Therefore, Bloch states with different symmetries in the ferromagnetic electrodes can couple with the evanescent states in Al-O barrier. All Bloch states will all contribute to the polarization, either in positive way or in negative way. This actually lowers the net polarization and therefore total TMR for Al-O barrier MTJs.

Figure 3.3(b) schematically shows the tunneling process for Fe(001)/MgO(001)/Fe(001) junction [8]. Considering the conservation of the coherence of electron wave function, Bloch states with Δ_1 symmetry have a finite tunneling probability while Bloch states with Δ_2 and Δ_5 symmetry decays rapidly and the tunneling process is almost terminated. Moreover there is no minority spin state at Fermi level for Δ_1 state electrons. Therefore, in this epitaxial MTJ with a crystalline MgO (001) tunneling barrier, it only allows the coherent tunneling of $\Delta_1$band electron to dominate the TMR effect and therefore results in high TMR ratio.

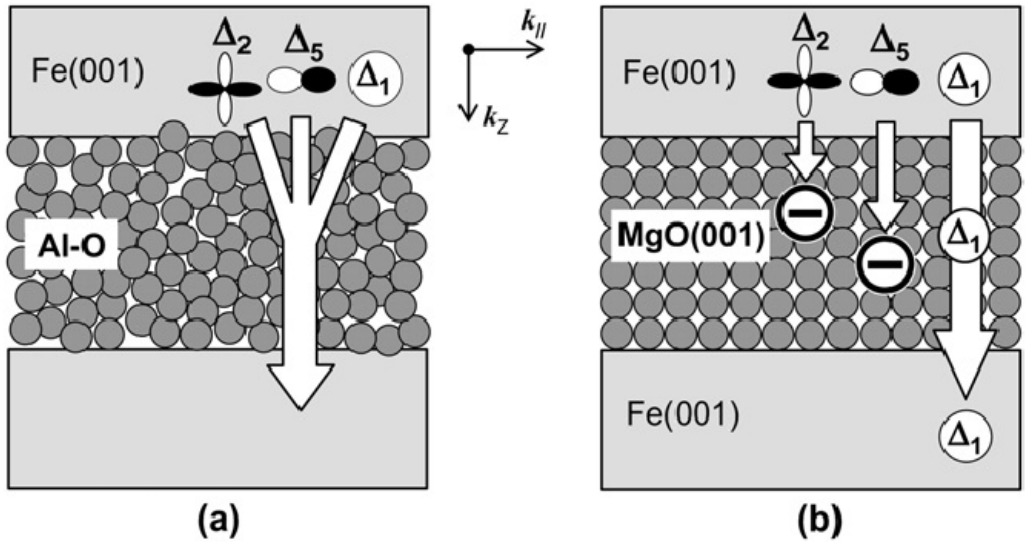

Figure 3.3 Two electron tunneling processes for (a) incoherent tunneling in amorphous Al-O barrier and (b) coherent tunneling through a crystalline MgO (001) barrier [8].

3.2 Experimental Methods

The major experimental methods used for the fabrication of MgO-barrier MTJs are introduced in this section, roughly in the order they are applied in the experiments. It includes SiO_2 substrate preparation, magnetron sputtering deposition, photolithography patterning and ion milling, SiO2 deposition, gold deposition and magnetic thermal annealing.

3.2.1 Oxidization of Si wafer

We are using one-side polished, 2-inch silicon wafer from Silicon Quest International, Inc. As we already explained before, high-quality MgO MTJs have to be deposited on top of SiO_2. After the silicon wafers go through the standard cleaning procedure, they are

loaded into high temperature oxygen furnace. It can generate around 1.5μm thickness of SiO_2 with setting the furnace at 1150^0C for 20 hours. The operation procedure is presented in Appendix A in the end of this chapter.

3.2.2 Sputtering Deposition of MTJ multilayer stacks

In our lab we have two high vacuum magnetron sputtering systems. Both of them can be used to deposit MTJ multilayer structures. Now the new system is exclusively used for the MTJ deposition and the old system can also be used for SiO_2 and electrode deposition. The new system is totally automatic and controlled by Labview software. The base pressure can reach down to 1×10^{-8}Torr. The old system can only reach 1×10^{-7}Torr and is manual controlled. Both the operation procedures are presented in Appendix B.

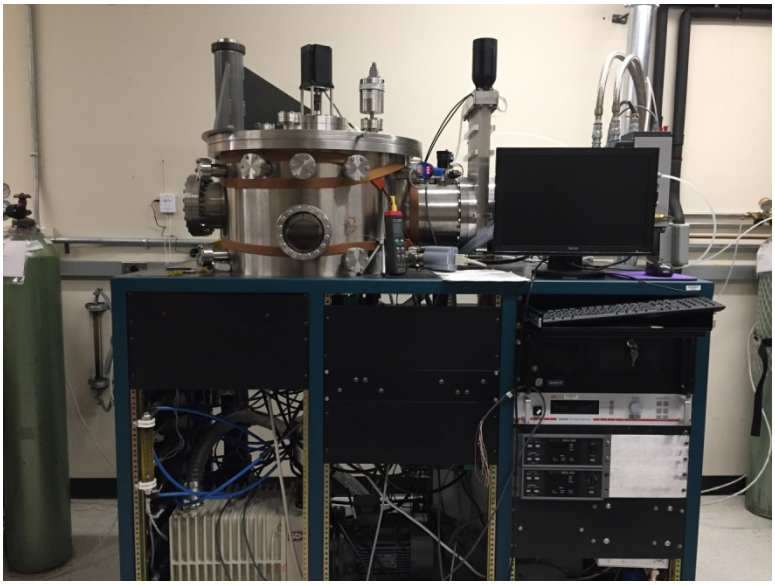

Figure 3.4 The image of new magnetron sputtering system.

The MTJ stack has the following structure (thickness in angstroms): SiO_2/50 Ta/300 Ru/50 Ta/30 CoFe/180 IrMn/30 CoFe/8.5 Ru/30 CoFeB/t MgO/25 CoFeB/3 Ta/400 Conectic/50 Ta/100 Ru (the unit is Angstrom). Before the MTJ stack deposition, all the

material has to be calibrated individually to get the deposition rate. A few examples of thickness calibration are shown in Figure 3.5.

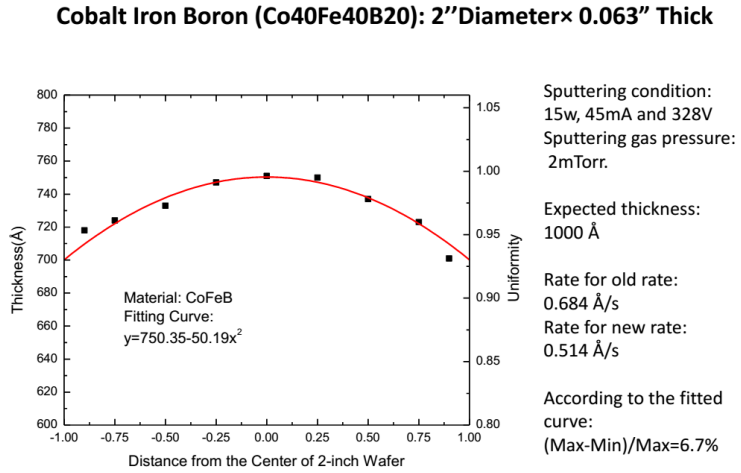

(a) Thickness calibration for CoFeB material over two-inch substrate wafer.

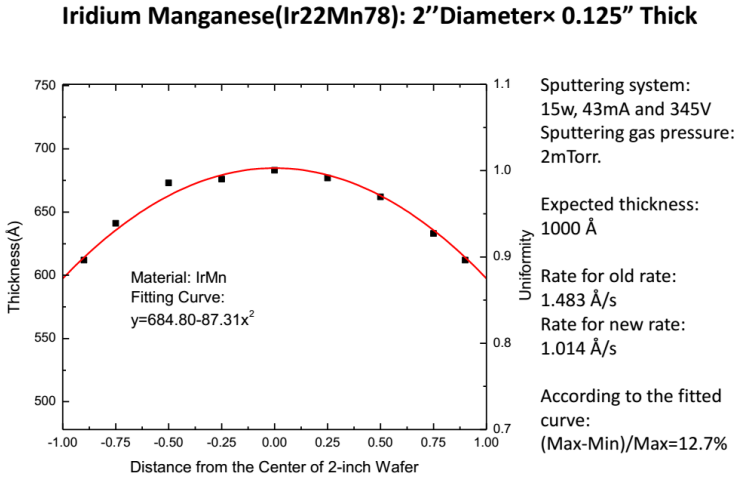

(b) Thickness calibration for IrMn material over two-inch substrate wafer.

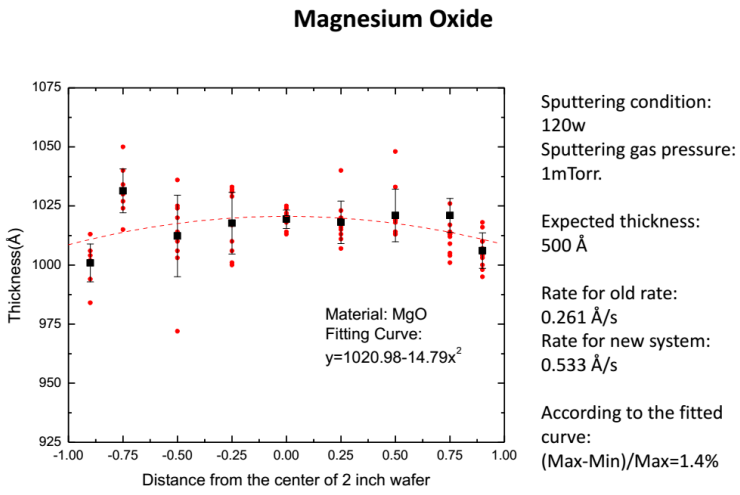

(c) Thickness Calibration for MgO material over two-inch substrate wafer.

Figure 3.5 A few calibration examples over two-inch substrate wafers.

3.2.3 MTJ fabrication: first patterning

The standard processing steps are described in Figure 3.6. The photolithography is used to define the ion-milling area or deposited area. The photoresist we are using is AZ5214. The photolithography procedure through MTJ processing is all done by Karl Suss Mask aligner (Figure 3.7) in the cleanroom. The photolithography procedure is described in Appendix C.

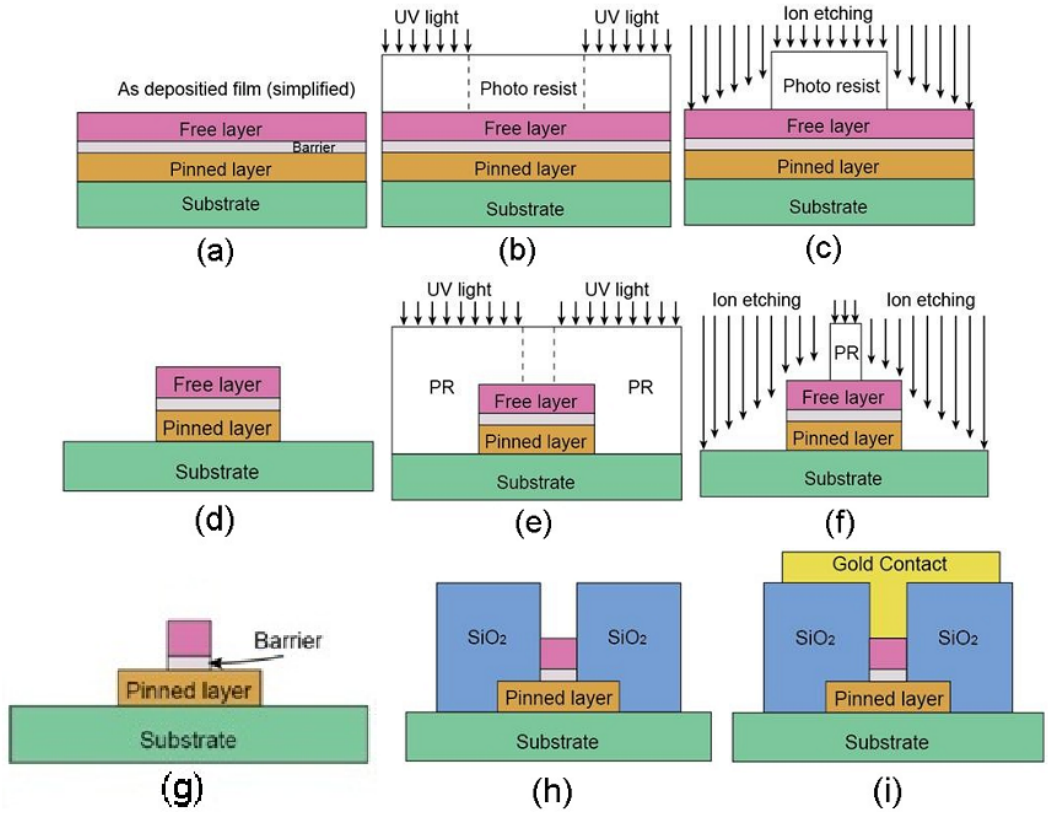

Figure 3.6 Schematic diagram of the MTJ processing (a) as-deposited film after sputtering. (b, c, d) the 1st patterning and ion milling are used to define the bottom layer. (e, f, g) the 2nd patterning and ion milling are used to define the junction area. (h) SiO_2 layer is deposited to insulate the top and bottom layer. (i) lift-off method is used to create the top gold electrodes.

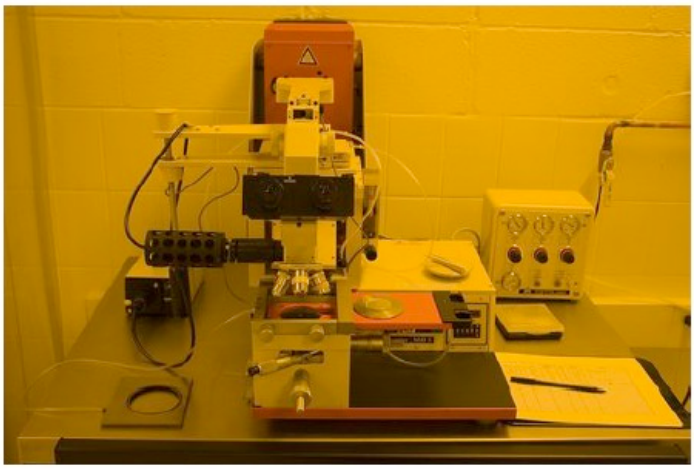

Figure 3.7 The image of Karl Suss Mask Aligner

3.2.4 MTJ fabrication: first ion milling

The operation procedure is presented in Appendix D.

3.2.5 MTJ fabrication: second patterning

The second patterning is used to define the junction area. The very first thing is that we have to remove all the residue photoresist and dust from the 1st patterning and ion milling. Sample will be sonicated in sequence of Acetone, Methanol, IPA and DI water. The process details are similar to Section 3.2.3. However, it requires the mask alignment in this step.

3.2.6 MTJ fabrication: second ion milling

The second ion milling is used to create the junction area. This is the most important step to generate high-quality MTJ junctions. The rotation etching method is developed to reduce the re-deposition or sidewall effect. The detail processing procedure is similar to Section 3.2.3. The etching angel is changed between high angle and low angle. The high angle etching is mainly on removing the surface while low angle etching is actually more focused on cleaning the sidewall.

3.2.7 MTJ fabrication: SiO_2 deposition

Before the deposition of top electrodes, one layer of SiO_2 has to be deposited to insulate the bottom layer and the top electrode. Right after the second ion milling, the sample will

be loaded into the old sputtering system. The sputtering procedure is quite similar to Section 3.2.2. For SiO_2 deposition, Si target is used with Argon and Oxygen as the sputtering gas. The sputtering power is 150W and sputtering pressure is 4mTorr. 1800Å SiO_2 is deposited.

3.2.8 MTJ fabrication: third patterning

The purpose of this step is to define the deposition window for Ti and Au. It is the same as Section 3.2.4. First we need to do the lift off to open the junction windows. After the SiO_2 deposition, the junction area is submersed under the photoresist and deposited SiO_2. Therefore it will take a long time sonication. The detail procedure of the lift-off method is described as below:

1. Soak the sample in Acetone for 1 hour. It is better to heat the sample up to 40^0C. This is very important during winter time.
2. Sonicate the sample in the sequence of Acetone, Methanol, IPA and ID water.
3. Use Q-tip with Acetone to scrub the sample surface gently. Use microscope or Dektak to make sure all photoresist residues have been removed.
4. Use Acetone and DI water to rinse the sample for 10 minutes.
5. Blow the sample dry using nitrogen gun.

Then the sample can go through the spin coating and mask alignment as usual.

3.2.9 MTJ fabrication: Gold Deposition

The top electrode is 100Å Ti and 1000Å Au. E-beam Evaporator or Sputtering can be used in this step. Ti is first deposited to provide better adhesion for Au. After the

deposition, the sample will go through the lift-off procedure to remove the extra photoresist and Ti/Au.

3.2.10 Magnetic thermal annealing

This is the final step in MTJs fabrication. The magnetic thermal annealing station is a high vacuum system which can provide 0.5Tesla magnetic field and up to 400^0C temperature capability. The magnetic field over the sample area is uniform. Aluminum sample holder box is placed between permanent magnets. The temperature over the sample box is uniform during the heating process. The magnetic thermal annealing will not only set the exchange bias in the synthetic antiferromagnetic trilayer but also help to crystallize the CoFeB layer using MgO (001) as a template and remove the lattice disorder. The detail procedure is described in Appendix E. Until this step, the whole procedure for MTJs fabrication has finished. Following this procedure, we have successfully developed single MTJ sensors, series MTJ sensors and all other kinds of MTJ devices.

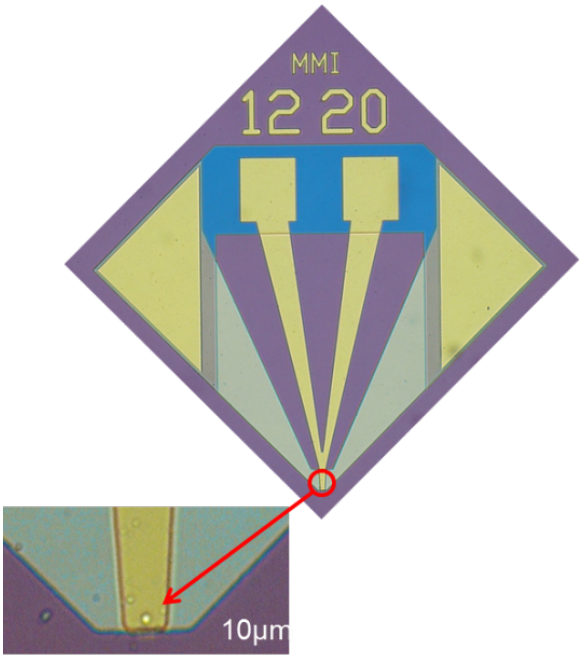

(a) Single MTJ image

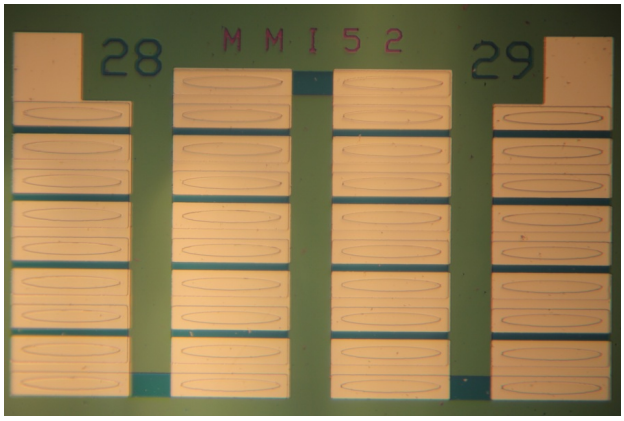

(b) 38-MTJ Array image

Figure 3.8 The image of (a) single MTJ and (b) 38MTJ sensor in series.

3.3 Characterization

The layer structure of our fabricated MTJs is Substrate /Ta(50) /Ru(300) /Ta(50) /$Co_{50}Fe_{50}$(30) /$Ir_{22}Mn_{78}$(180) /$Co_{50}Fe_{50}$(30) /Ru(8.5) /$Co_{40}Fe_{40}B_{20}$(30) /MgO(t) /$Co_{40}Fe_{40}B_{20}$(30) /Ta(3) /Conetic($Ni_{77}Fe_{14}Cu_5Mo_4$)(400) /Ta(50) /Ru(300)(thickness in

Angstrom) shown in Figure 3.9. The most critical structure is the MgO barrier layer and the two adjacent ferromagnetic layers, usually named as top layer (free layer) and bottom layer (pinned layer). The bottom layer will be pinned after magnetic thermal annealing. The Ta/Ru/Ta/CoFe layer acts as a seeding layer for IrMn antiferromagnetic (AFM) layer. The AFM layer will pin the adjacent ferromagnetic layer through exchange bias. The direction of exchange bias field can be set using the external magnetic field by cooling the AFM material through Neel temperature. In order to provide better pinning effect, a tri-layer structure of CoFe/Ru/CoFeB which is called synthetic anti-ferromagnetic (SAF) layer is selected to replace the normal one layer of ferromagnetic CoFeB. There are three important reasons to use this SAF layer. First, this structure increases the separation between IrMn and MgO layer. During high temperature annealing, there will be less Mn which can diffuse to MgO layer. This kind of diffusion can damage the MgO barrier. Second, this tri-layer structure has stronger and more thermally stable exchange bias. In the end and most importantly, SAF layer can reduce the stray field effects and then reduce the asymmetry problem of magnetoresistance hysteresis loop for the junction.

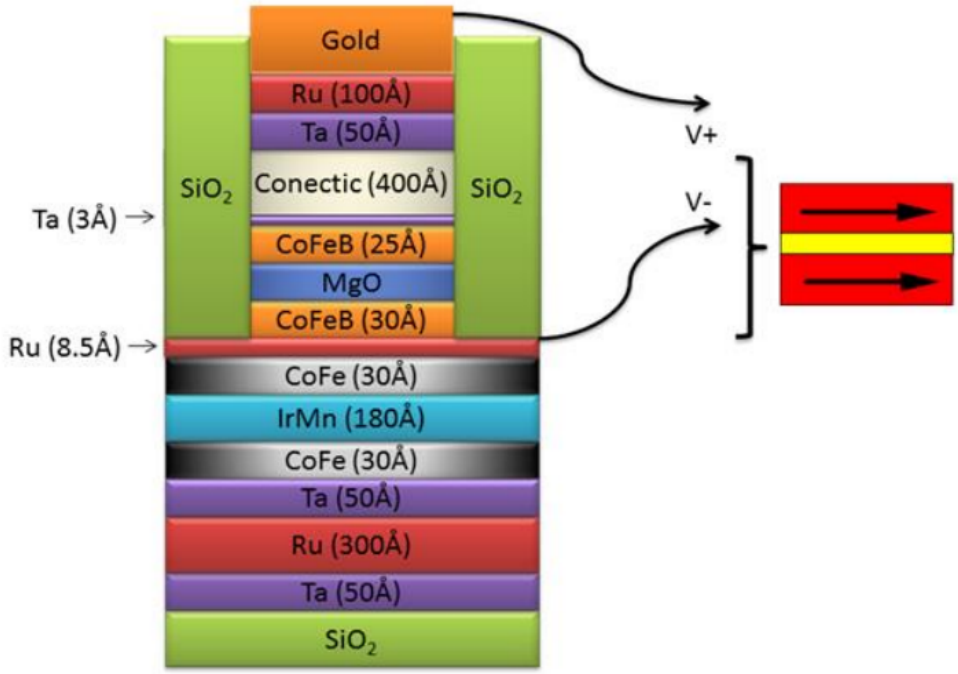

Figure 3.9 Schematic drawing of the MgO-barrier magnetic tunneling junctions.

3.3.1 Vibrating Sample Magnetometer (VSM) Measurement

Vibrating sample magnetometer (VSM) is not only a good method to characterize the magnetic properties of MTJ sample without patterning but also a good trouble-shooting method. The hysteresis loops, exchange bias coupling strength and synthetic antiferromagnetic coupling strength can be extracted from VSM measurement. In Figure 3.10, there is a VSM result for a representative structure as Substrate /Ta(50) /Ru(300) /Ta(50) /$Co_{50}Fe_{50}$(30) /$Ir_{22}Mn_{78}$(180) /$Co_{50}Fe_{50}$(30) /Ru(8.5) /$Co_{40}Fe_{40}B_{20}$(30) /MgO(23) /$Co_{40}Fe_{40}B_{20}$(30) /Ta(3) /Conetic($Ni_{77}Fe_{14}Cu_5Mo_4$)(400) /Ta(50) /Ru(300)(thickness in Angstrom). The magnetic free layer of $Co_{40}Fe_{40}B_{20}$(30) /Ta(3) /Conetic($Ni_{77}Fe_{14}Cu_5Mo_4$)(400) shows a sharp magnetization reversal around the zero field indicated by the purple bar. The red bar represents the biasing field imposed on

CoFeB affected by the SAF coupling and the strength is 600Oe. As mentioned before, IrMn and the SAF layer structure can improve the exchange bias strength. The cyan bar shows the biasing field imposed on the CoFe seed layer. The green bar shows the biasing field of CoFe imposed by the exchange biasing and SAF coupling. This is the basic mechanism for MTJs. Only when all the magnetic layers have their hysteresis loops in expected positions, the free layer of MTJs can correspond to external field easily while the pinned layer of MTJs stays unaffected.

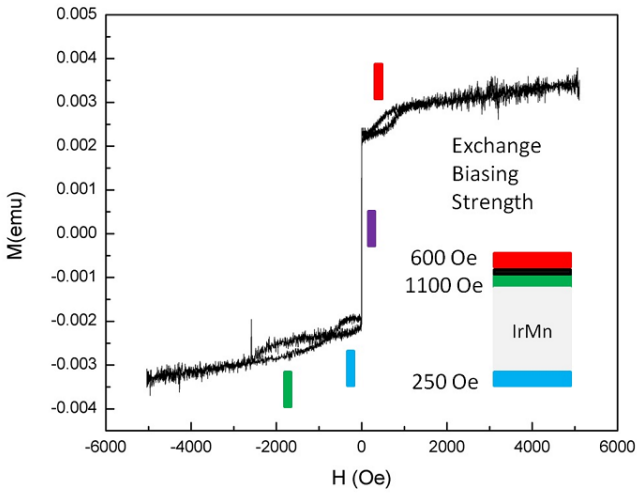

Figure 3.10 VSM measurement of a standard MTJ multilayer structure. Inset: the simplified MTJ layer structure(from bottom to top): $Co_{50}Fe_{50}(30)$ /$Ir_{22}Mn_{78}(180)$ /$Co_{50}Fe_{50}(30)$ /Ru(8.5) /$Co_{40}Fe_{40}B_{20}(30)$. The strength of the biasing field is labelled on the left.

We also fabricated a series of MTJs: Substrate /Ta(50) /Ru(300) /Ta(50) /$Co_{50}Fe_{50}(30)$ /$Ir_{22}Mn_{78}(180)$ /$Co_{50}Fe_{50}(30)$ /Ru(8.5) /$Co_{40}Fe_{40}B_{20}(30)$ /MgO(19, 20, 21, 22, 23, 24) /$Co_{40}Fe_{40}B_{20}(30)$ /Ta(3) /Conetic($Ni_{77}Fe_{14}Cu_5Mo_4$)(400) /Ta(50) /Ru(300)(thickness in Angstrom). The VSM results for this series sample showed how the MgO thickness will affect the position of the minor loops and coercivity field of each loop.

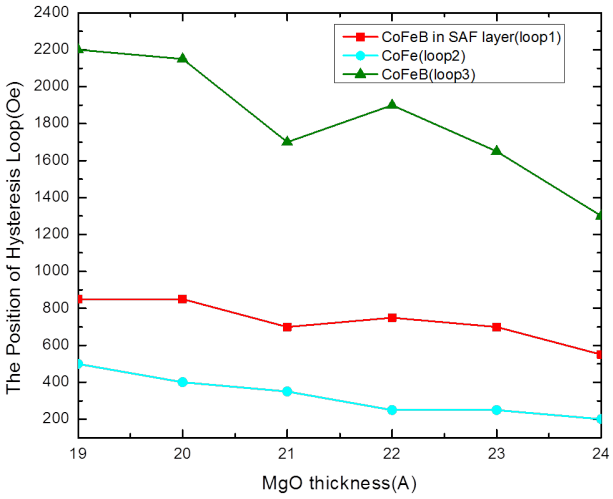

Figure 3.11 The relation between the center of hysteresis loops and MgO layer thickness.

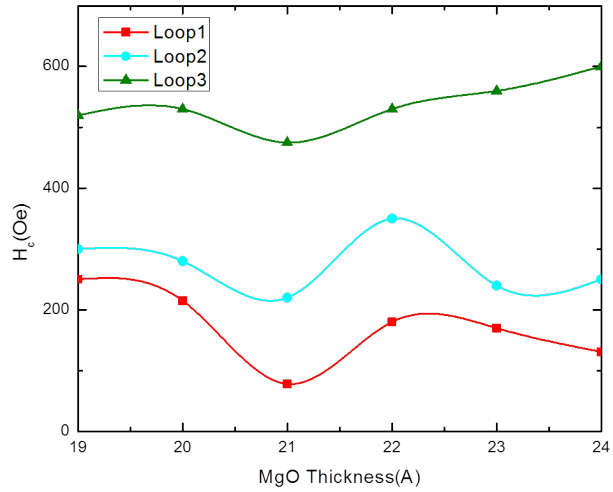

Figure 3.12 The relation between the coercivity field of each minor loop and MgO layer thickness.

3.3.2 Circle and Linear Transfer Curve Measurement

A series of standard MTJ samples of substrate /Ta(50) /Ru(300) /Ta(50) /$Co_{50}Fe_{50}$(30) /$Ir_{22}Mn_{78}$(180) /$Co_{50}Fe_{50}$(30) /Ru(8.5) /$Co_{40}Fe_{40}B_{20}$(30) /MgO(19, 21, 23, 25)

/$Co_{40}Fe_{40}B_{20}$(30) /Ta(3) /Conetic($Ni_{77}Fe_{14}Cu_5Mo_4$)(400) /Ta(50) /Ru(100)(thickness in Angstrom) have been fabricated and patterned. The sample is annealed along the short axis of the ellipse in Figure 3.8.

The circle transfer measurement is an angle-dependent resistance measurement. During the rotation of a constant magnetic field in plane, the resistance is recorded. If the external magnetic field is large enough to fully align the magnetization of the free layer, it will follow that external field. The resistance curve is sinusoidal. One example is shown in Figure 3.13. For this particular junction, the MgO thickness is 25Å. R_{ap} and R_p are $2.01\times10^4\Omega$ and $1.03\times10^4\Omega$ respectively. The MR is 95.8% calculated through this equation $\frac{R_{ap}-R_p}{R_p}$.

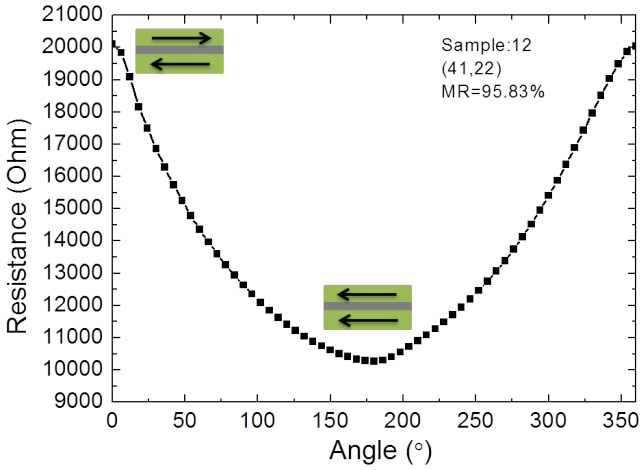

Figure 3.13 One circle transfer curve measurement. The magnetic field is 100Oe. By rotating it by 360° in the sample plane, the magnetization of the free layer will follow and the anti-parallel and parallel states can be achieved shown in the inset.

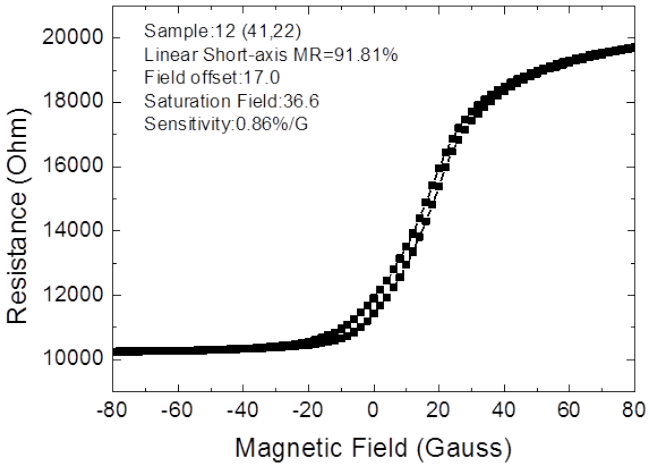

Figure 3.14 One linear transfer curve measurement. The magnetic field is 80Oe. The anti-parallel and parallel states can be achieved by applying 80Oe and -80Oe magnetic field.

There is another transfer characterization method called linear transfer measurement. The resistance is recorded while changing magnitude of external magnetic field in the same direction. The sample in Figure 3.14 is characterized using linear transfer curve method. For this sensor-mode sample, the annealing direction is along the short axis. After the annealing, without magnetic field the magnetization of bottom layer is kept along the short axis while the magnetization of free layer will come back along the long axis due to the shape anisotropy. During the linear transfer measurement, an external magnetic field is applied along the short axis and affects the magnetization of free layer. When the magnetic field reaches positive 80Oe, the magnetization of free lays is fully aligned in the direction of antiparallel to the bottom layer. When the magnetic field reaches negative 40Oe, the magnetization of free layers is fully aligned in the direction parallel to the bottom layer. Based on this linear transfer curve, MR is about 91.8%.

As you can see, the MR results are slightly different for circle and linear transfer measurement. That's because even the magnetic field in the linear transfer measurement is large enough to overcome all the anisotropy of the free layer, the magnetic field direction cannot be guaranteed to be perfectly aligned with the magnetization of the bottom layer. First, there is no way we can know the magnetization direction of bottom layer. It depends on the annealing process and the shape anisotropy. Second, even we know the pinning direction, during the measurement, there is no way to apply external magnetic field perfectly along the pining direction. In circle transfer measurement, through rotating the external magnetic field by 360^0, it will cover the two states of parallel and anti-parallel anyway. Therefore, circle transfer measurement is better method for MR calculation. However, the advantage of linear transfer measurement is that the coercivity and sensitivity can be extracted directly.

3.3.3 Sensitivity

The field sensitivity is given by $S = \frac{R_{\uparrow\downarrow} - R_{\uparrow\uparrow}}{R_{\uparrow\downarrow} + R_{\uparrow\uparrow}} \frac{1}{B_{sat}}$ where B_{sat} is the magnetic saturation field of free layer. It is the most important number for the sensor device and people have put a lot of efforts to improve. From this equation, the sensitivity can be improved through increasing MR and reducing the saturation field. The sensitivity of the sample in Figure 3.13 is 0.86%/Oe. This is the typical sensitivity we can achieve for our MTJ array sensors.

In Figure 3.14, the transfer curve is shifted to the positive side and there is about 17.0Oe offset. There are two reasons to cause this offset. First, during the annealing process some

pinning effect is introduced to cause the magnetization of free layer is no longer along the long axis. The major reason is due to the internal coupling field. There are two kinds of mechanism contributing to the internal coupling [9-12]. One is called Neel coupling due to interface roughness. That's one of the reasons why low pressure is preferred during MTJ stack deposition. The other internal coupling is called magnetostatic coupling. For small MTJs and over etched pinned layer, the free layer can feel a magnetic field generated by uncompensated poles on the edges of the pinned layer. The smaller the junction is, the larger the magnetostatic coupling field will be. The etching rate of ion milling has to be known very well in order to make sure the second ion milling can stop right before the pinned layer and therefore less uncompensated poles generated.

3.4 Single MTJs

The fabrication procedure of single MTJ is basically the same as MTJ arrays which we have described above. The brief procedure is presented in Figure 3.15. Because of the multiple junctions, the MTJ arrays carry more inherent local disorder or disorder which is introduced during the fabrication. For single MTJ, it has better space resolution and is more ideal for theoretical research.

Figure 3.15 The sample images showing the processing procedure.

We developed high-quality single MgO-barrier junction. Based on our sensor design shown in Figure 3.15, there are 2500 unit cells of single MgO-barrier junctions in a 2-inch wafer. Even though there is only one micro-size junction in the circuit, it is very robust and can go through different measurements for many times. The uniformity has been verified by the distribution study. The resistance, TMR ratio and the shape of transfer curves are similar all over the wafer. In Figure 3.16, there are a few examples of transfer curve measurement. MR is consistent over 100%. The parallel resistance is around $5.0\times10^{3}\Omega$ and antiparallel resistance is around $1.0\times10^{4}\Omega$ consistently.

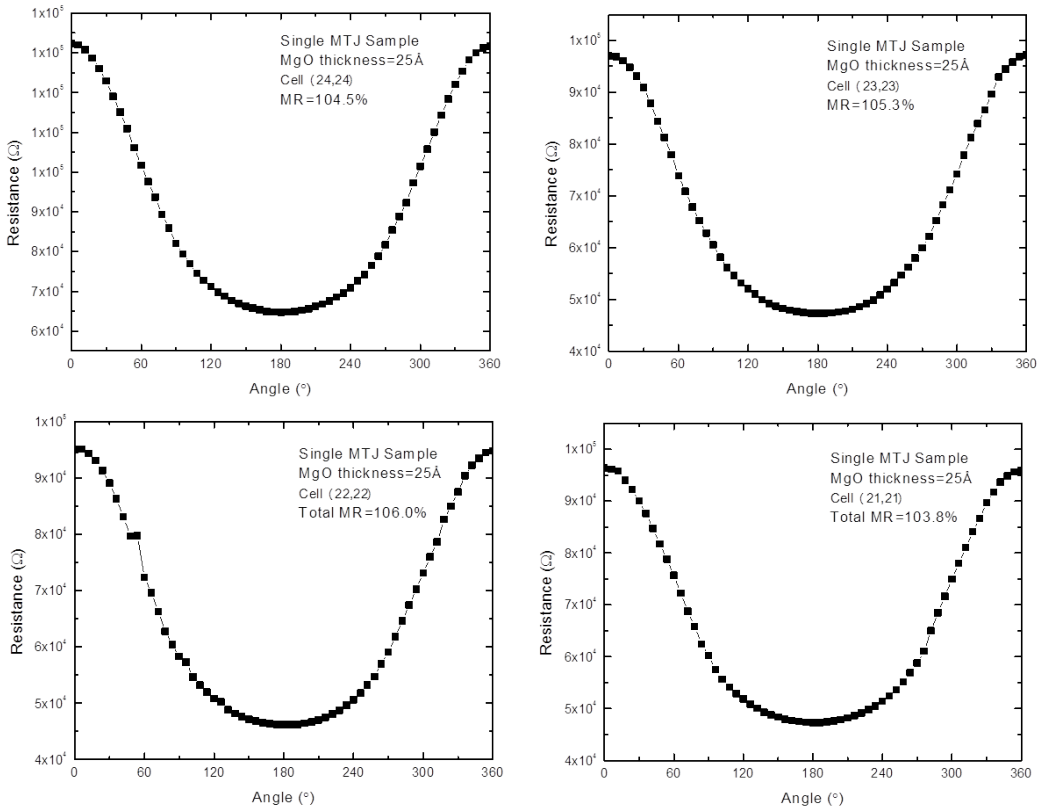

Figure 3.16 The examples of transfer curve measurement for single MTJ. All the MTJ units are from the same wafer. They are showing the similar shape of transfer curve, MR, ratio and resistance.

3.5 Summary

In this chapter, we first went through all the basic theory about MgO-barrier MTJs. Then in the sequence of the fabrication procedure, we discussed all the experiment techniques, including sputtering, photolithography, ion milling and annealing. Through these techniques, we successfully designed and fabricated two kinds of MTJ sensors, MTJ array and single MTJ. The magnetic characterization method, VSM, is used to review the intrinsic mechanism of MTJs. The electrical characterization method, transfer curve

measurement, is used to examine the sensor performance. The single sensor and array sensor have been studied and compared. Furthermore, we also compare the linear transfer curve and the circular transfer curve.

Appendix A

The oxygen furnace operation procedure is as below:

1. Raise the furnace temperature
   (a) Close the Nitrogen valve and fully open Oxygen valve.
   (b) Set the flow rate for Oxygen: 0.2×full range.
   (c) Turn on the Oxygen module on the flow controller panel.
   (d) Increase the temperature on temperature controller to 1150^0C.
   (e) Wait until the temperature reaches the set point.
2. Oxidize the sample.
   (a) Insert the sample into the middle area of the furnace tubing.
   (b) Turn on the Oxygen flow and make sure the actual flow rate is as the set point.
   (c) Wait until 24 hours to get the sample out.
   (d) Turn off the oxygen flow and decrease the temperature to 500^0C which is the default temperature for the furnace.

Appendix B

The old sputtering operation procedure is described as below:

Step 1: Sample Loading and Main Chamber Pump Down

1. Close the gate valve for cryopump.
2. Open the nitrogen tank and the vent valve which controls the gas in and out for the chamber. Wait until the pressure reaches 7.4×10^{2}Torr and then close the vent valve and the nitrogen tank.
3. Lift the top plate up and carefully load it on the dolly.
4. Load the wafers on the sample holders.
5. Clean the chamber using vacuum cleaner.
6. Reload the plate to the chamber. Make sure the self-rotation bar sitting inside of the transmission bar.
7. Pump the chamber pressure down to 2×10^{-1}Torr using mechanical pump. Always turn on the power first and then open the pump valve.
8. Close the pump valve and then turn off the mechanical pump.
9. Open the gate valve and wait until the pressure reaches below 2×10^{-7}Torr.

Step 2: Deposition

1. Check the ion gauge. Press the button "1G2" to check the pressure. Then press "Degas" and wait for the pressure to stabilize and record the actual pressure reading.
2. Turn on the main water supply and each flow for all the guns.
3. Open the gas flow controller. Before that, make sure to adjust Baratron gauge to zero using a screw driver at the back of the gauge.
    a) Open the Ar tank.

b) Turn on the power supply of gas control panel 247.

c) Switch the knob to Ch1 to open the gas line for Ar (this is gas controlled switch and the requirement gas pressure is 70psi.) and adjust the set point for Argon at 22.5ccm.

d) Adjust Baffle valve to 30^0.

e) Turn on CH1 on the panel 247.

4. Connect the stepper motor and turn on the power. Turn on the computer.
5. Click "system initialization.vi". (File→Recently opened→Run)
6. Rotate substrate holder 1 to the front. Carefully align the holder 1 to the most front position.
7. Click "set stepper variables". (Let the computer record the position.)
8. Stop the program. (Click the red button.)
9. Pre-sputtering

a) Make sure Panel 250 is on "manual" mode.

b) Adjust Baffle valve to make sure the read is 4mTorr on Baratron gauge.

c) Open the rotate program and input the times of rotation. (One circle is 11 seconds and 220 circles means 40 minutes. That's enough for pre-sputtering.)

d) Turn on the power supply for the sputtering guns and select the target.

e) Press "start" on the power supply.

If the plasma is on, adjust Baffle valve to 4.0mTorr and wait for 8 minutes for pre-sputtering. If the plasma is not on, shuffle the shutter. Or select a neighboring target and generate the plasma for it first. Or increase the chamber pressure to help to generate plasma.

Pre-sputtering MgO is different from metallic targets.

a) Make sure Panel 250 stays on “Manuel” mode.

b) Test no. 7 shutter. (pressure for opening no. 7 shutter is only 5psi)

c) Turn on the power supply(151w) and switch the matching network(Check Manual→0.5, Tune→0.5, Load→0.5. When the plasma is on, switch to “auto” mode. And adjust Buffer valve to make 250 panel 3.4 mTorr for Baratron gauge).

d) Wait for 8 minutes.

e) Turn off the power supply.

10. Real Deposition

a) Change Panel 250 to “Auto”.

b) Adjust Baffle valve to 30^0. (Baratron gauge should read 2.05mTorr.)

c) Test shutter before generating the plasma. (The pressure for no. 2 shutter is 50psi; the pressure for no. 7 is 5ps; the others’ is 30psi.)

d) Generate the plasma for one material we need.

e) Select material and thickness. Then click “Run”.

f) Finish sputtering. Turn off the power supply of the plasma. (“start” on the front panel is to control the power. Switch on the back panel is to turn on/off power supply.)

For MgO sputtering, there is some difference we need to keep in mind.

a) The panel 250 stays on “Manuel”.

b) Adjust Baffle valve to 60^0 and check the Baratron gauge is 0.7mTorr.

c) Test no. 7 shutter. (The pressure is 5psi.)

d) Adjust the power supply to 120w and switch the matching network to "auto" (there are two). (Check Manual→0.5, Tune→0.5, Load→0.5. When the plasma is on, switch to "auto" mode. And adjust Buffer valve to make 250 pannel 0.8mTorr for Baratron guage.).

e) Turn on the power supply.

f) Initialize rotate.vi and set it rotate 12 circles

g) Initialize the program.

11. After finishing sputtering

a) Change Panel 250 to "Manuel".

b) Turn off the flow on Panel 247 and power off Panel 247.

c) Adjust Baffle valve to 90^0.

d) Turn off the Bottom Motor and stepper motor (switch on the wall).

e) Close Nitrogen tank and Ar tank.

f) Turn off the water flow and water supply.

g) Wait for 45-60 minutes for the system to cool down.

12. Close the gate valve.

13. Vent the chamber by opening the valve of N_2 tank (the first one) and turning on the switch right behind the chamber.

14. Wait the pressure of the chamber to be 7.6×10^2Torr. Open the chamber and get the sample out.

The new sputtering operation procedure is described as below:

1. Carefully put the samples on the substrate holder and make sure that samples are sitting flat on the holders. Put the holders back on the top plate. And use nitrogen gun to clean the surface.
2. Align the pivots of the main substrate holder and the spindle from the bottom in the vertical direction. Then slowly lower the top plate and cover the chamber. Carefully low the cover with the main chamber and close it.
3. Use the main control panel. Turn on mechanical pump and then rough valve. Wait until the pressure below 100mTorr. Close the rough valve and turn off the mechanical pump.
4. Open the gate valve. To keep the valve gate to stay in its position, we use the gas provided by school on the wall, whose pressure is 60psi. However to move the gate valve, we use the 80psi gas from the nitrogen tank.
5. Wait the system to pump down at least for one day before the deposition.
6. Check the base pressure of the chamber. The pressure after one-day pumping should be around 3×10^{-8}Torr for record.
7. Before running any Labview program, check the cooling water for each gun.
8. Make sure the gas provided for all solenoids. Gas valve needs 30psi and shutters need 10psi.
9. Run Labview Program “Pre-sputtering”.

There is a default setting for this program. We sputter each pair of targets for 8 min. We have to keep two rules in mind if we need to use the program in a different setting.

1) Target 1, 2 and 3 are sharing one power supply. They can't work at the same time. There is the same situation for target 4, 5 and 6.
2) The time for common rotation should be longer than the total presputtering time by two minutes.

10. When the "Pre-sputtering" program finished, the program "system initialization" will pop out. Do the position alignment.
11. During the pre-sputtering program runs, fill in the program of "thickness deposition". Pay attention to the sequence, power, thickness and position of samples.
12. Run the program of "thickness deposition". During the deposition, stay with the system and observe the deposition. Record anything unusual in the log book.
13. After the deposition, run the program of "venting". Then wait for an hour and a half until the system cools down.
14. Open the nitrogen tank and switch behind the chamber to vent. Wait until the pressure of the chamber becomes atmospheric.
15. Lift the top plate and get all the samples out.
16. Close the chamber and pump it down.

Appendix C

The photolithography procedure for MTJ processing is all done by Karl Suss Mask aligner (Figure 3.7) in the cleanroom. The photolithography is described as follows:

1. Sample Cleaning.

   (a) Put the sample in Acetone, Methanol and DI water in sequence for sonication.

(b) Blow the sample dry with Nitrogen gun.

2. Spin Coating.

(a) Set the hot plate at 110^0C.

(b) Set the spin coating machine at 4000rpm/s, 4000rpm/s^2 and 30sec. These parameters can give 1.4μm thickness of photoresist.

(c) Put the sample in the center of vacuum holder and drop the photoresist on it. Carefully apply the photoresist to fully cover all the sample area.

(d) Run the program and put the sample on hot plate for 2 minutes.

3. Mask alignment and exposure.

(a) Set the aligner ready. Turn on the gas flow and power supply. Change the filter to 365nm light and Set the power to 275W. Wait the machine to warm up and there is a green light showing it is ready to use.

(b) Load the mask and the sample. Carefully align the sample with the effective mask area.

(c) Set the exposure time to 22 seconds.

(d) Expose. Before the exposure, lift the sample stage and make sure the mask and the sample are in tight physical contact. Vacuum the sample holder chamber and choose the contact mode to even reduce the gap between the sample and mask.

4. Development.

(a) Prepare the developer of AZ327.

(b) Remove the sample and develop it in the developer for 30 seconds. Actually the develop time depends on a lot. Carefully observe the color change of the sample surface is the only way to avoid over or under development.

(c) Rinse with DI water and blow the sample dry.

(d) Check the sample under microscope. If the sample is under development, repeat 4(b) for some time. If the sample is over development, repeat 1-4 again.

Appendix D

The ion milling process sequence is described as follows:

1. Sample loading.
   (a) Make sure to turn off the ion gauge and close the gate valve.
   (b) Vent the chamber using Nitrogen and wait until the atmosphere reaches.
   (c) Clean the ceramics holder to avoid any contamination during the ion milling process. Use vacuum grease to hold the sample and put the ceramics O-ring on top of it carefully. Secure the wafer.
   (d) Close the chamber.
2. System pumping down.
   (a) Rough down the chamber using mechanical pump. Wait until the pressure down to 150mTorr.
   (b) Close the rough valve and turn off the mechanical pump. Open gate valve.
   (c) Turn on the ion gauge. Wait about 1 hour until the pressure down to 2×10^{-6}Torr.
3. Processing Procedure.

(a) Turn on the cooling water.

(b) Turn on the rotation motor and set it to 22V.

(c) Open Argon gas line and Set the mass flow controller to auto mode. Wait until the pressure reads 1.8×10^{-4}Torr.

(d) Turn on the main power of ion milling current. If it is normal, the ion current and the neutralizer will automatically turn on in a few seconds. Wait two minutes for stabilization.

(e) Set the ion current source to 142mA. Turn on the neutralizer and adjust the ion current to be 0. Readjust a few times. Check the plasma voltage is 50V and the plasma current is 4.2mA.

(f) Open the shutter and set the sample plate to 80^0. Make sure the ion current is about 17mA to give the right etching rate.

(g) Wait for 8 minutes (The rate can change over the time. Calibration has to be done every three months.) Turn off the current source power. Set the sample plate vertical and close the shutter. Turn off the power of rotation motor.

(h) Turn off the mass flow controller and close Argon gas. Turn off the ion gauge and close gate valve. Turn off the cooling water.

(i) Wait 1 hour for cooling down the system and get the sample out.

Appendix E

The detail procedure for annealing is described as below:

1. Load the sample on the sample holder. Carefully align the sample to make sure the magnetic field will apply in the right direction.
2. Put all the holders with sample into the metal box. Readjust the position of the box.
3. Close the chamber and make sure the gas valve for venting is closed.
4. Rough the chamber using mechanical pump and wait until the pressure down to 1×10^{-1}Torr. Close the rough valve and open the gate valve.
5. Turn on the power supply of the turbo pump.
6. Wait until the pressure down to 2×10^{-6}Torr. It takes about 30 minutes.
7. Set the program of heater controller and turn on the heater. For MTJ annealing, usually the temperature will increase to 320^0C in 1 hour. This small increase step can help to avoid over heat. Then stay at 320^0C for 1 hour. After that naturally cool down.
8. The natural cool down takes about 12 hours. When the temperature is below 50^0C, turn off the heater. Close the gate valve and turn off the power supply of turbo pump. Vent the chamber and get the sample out. In order to protect turbo pump, wait another 20 minutes to turn off the mechanical pump.

Reference

1. M. Julliere, Physics letters A **54** (3), 225 (1975).

2. T. Miyazaki, T. Yaoi and S. Ishio, Journal of magnetism and magnetic materials **98** (1), L7 (1991).

3. T. Miyazaki and N. Tezuka, Journal of Magnetism and Magnetic Materials **139** (3), L231 (1995).

4. J. S. Moodera, L. R. Kinder, T. M. Wong and R. Meservey, Physical review letters **74** (16), 3273 (1995).

5. W. Butler, X.-G. Zhang, T. Schulthess and J. MacLaren, Physical Review B **63** (5), 054416 (2001).

6. J. Mathon and A. Umerski, Physical Review B **63** (22), 220403 (2001).

7. M. Bowen, V. Cros, F. Petroff, A. Fert, C. Martınez Boubeta, J. L. Costa-Krämer, J. V. Anguita, A. Cebollada, F. Briones and J. De Teresa, Applied Physics Letters **79** (11), 1655 (2001).

8. S. Yuasa, Journal of the Physical Society of Japan 77 (3), 031001 (2008).

9. A. Anguelouch, B. Schrag, G. Xiao, Y. Lu, P. Trouilloud, R. Wanner, W. Gallagher and S. Parkin, Applied Physics Letters **76** (5), 622 (2000).

10. B. Schrag, A. Anguelouch, S. Ingvarsson, G. Xiao, Y. Lu, P. Trouilloud, A. Gupta, R. Wanner, W. Gallagher and P. Rice, Applied Physics Letters **77** (15), 2373 (2000).

11. B. Schrag, A. Anguelouch, G. Xiao, P. Trouilloud, Y. Lu, W. Gallagher and S. Parkin, Journal of Applied Physics **87** (9), 4682 (2000).

12. L.-f. Li, X. Liu and G. Xiao, Journal of applied physics **93** (1), 467 (2003).

Chapter 4
Magnetic Tunneling Junction with Flux Concentrator

In this chapter we have introduced magnetic flux concentrator (FC) into our MTJs to significantly increase the magnetic sensing capability. The flux concentrator is a "soft" magnetic material with certain geometry working directly on the free layer of MTJ sensors as a magnetic field amplifier. Thin film of soft magnetic material $Co_{88}Nb_8Zr_4$ is successfully fabricated using sputtering technique. The new MTJ sensors including the thin-film FC of $Co_{88}Nb_8Zr_4$ are proposed based on our Comsol simulation, experimentally developed and characterized using linear transfer measurement. The sensitivity has been improved from 1%/Oe to 20%/Oe. Furthermore, we have included additional magnetic concentrators outside of the MTJ devices. With these approaches, we have increased the magnetic sensing capability of the MTJs significantly. Some preliminary test shows the sensitivity has been increased up to 500%/Oe.

4.1 Introduction

As we mentioned in last chapter, the sensitivity is given by $S = \frac{R_{\uparrow\downarrow}-R_{\uparrow\uparrow}}{R_{\uparrow\downarrow}+R_{\uparrow\uparrow}}\frac{1}{B_{sat}}$ where B_{sat} is the magnetic saturation field of free layer. Increasing MR and reducing magnetic saturation field are equally important to get large sensitivity. Scientists have been working on improving MR through developing new fabrication technique and searching new material for MTJs. For reducing magnetic saturation field, there is an effective method using flux concentrators. The flux concentrator is a "soft" magnetic material with

certain geometry working directly on the free layer of MTJ sensors as a magnetic field amplifier. Obviously, high permeability is the basic requirement for FC material. Geometrically the magnetic sensor is sitting in center between two flux concentrators and the gain factor (or amplification factor) is proportional to the length to gap ratio (h/Δ), shown in Figure 4.1[1, 2]. The sensitivity can be increased through increasing the length of the flux concentrators or reducing the gap. However, the length of flux concentrators is limited by the sensor space resolution. The gap is limited by the sensor dimension and photolithography resolution. All these factors have to be considered during our sensor design.

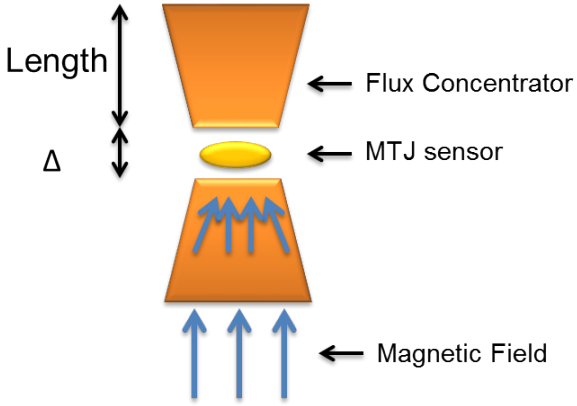

Figure 4.1 The ellipse represents our sensor and the trapezoid represents the flux concentrator. The gain factor is proportional to h/Δ where h is the length of the FC and Δ is the separation between two FCs.

4.2 Flux Concentrator Material $Co_{88}Nb_8Zr_4$

Based on wide literature search [3-5] $Co_{88}Nb_8Zr_4$ has been chosen to be the flux concentrator material. Even though some other materials in the bulk form also have high permeability and low coercivity, they have large magnetic anisotropy when they are fabricated in the thin film form. Amorphous CoNbZr is one of the few which has no

magnetic anisotropy in the thin film form. However, the thin-film CoNbZr with no anisotropy is hard to fabricate because all its magnetic properties are extremely sensitive to the fabrication condition, substrate condition and even its geometry [6-13]. Thin films of $Co_{88}Nb_8Zr_4$ have been successfully fabricated utilizing our high vacuum magnetron sputtering technique, and characterized using magnetometry measurement. The fabrication progress was briefly shown in Figure 4.2 and 4.3.

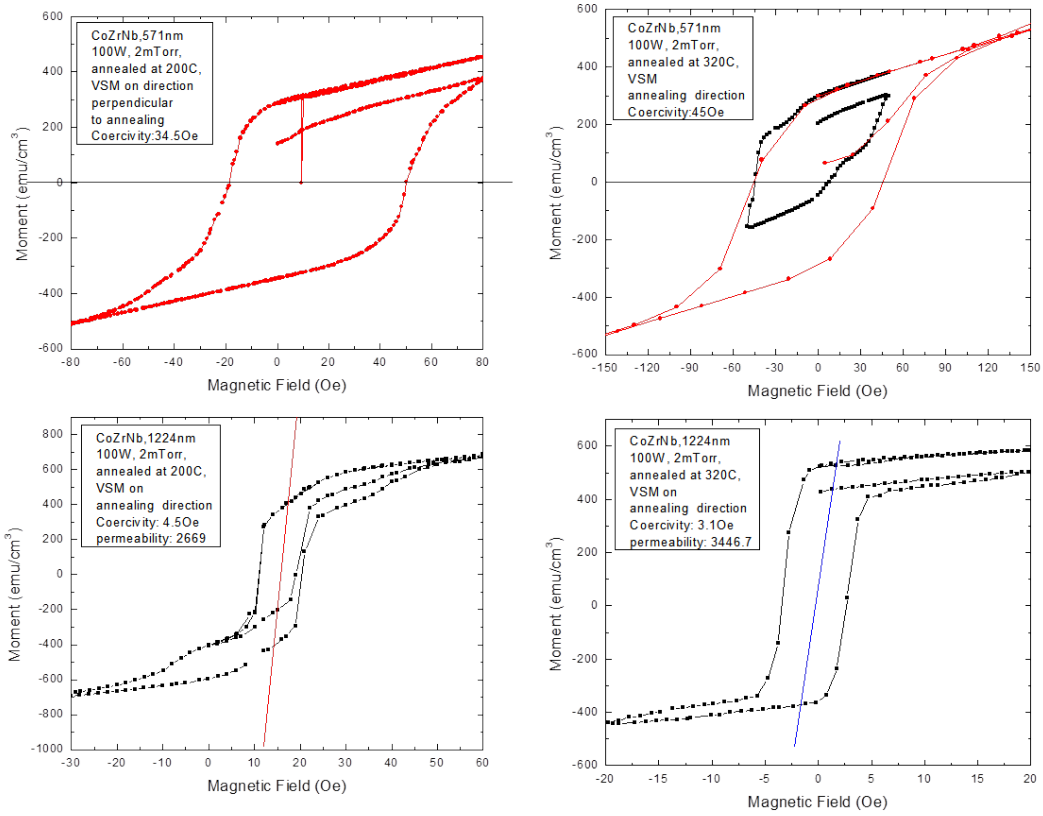

Figure 4.2 he VSM results for CoNbZr at different thickness. The sputtering pressure is 2mTorr and the DC sputtering power is 100W. Two films with thickness of 571nm and 1224nm have been made. VSM measurement along annealing direction and orthogonal to annealing direction has been done. Even though both films have large coercivity, thick film tends to give lower coercivity and permeability.

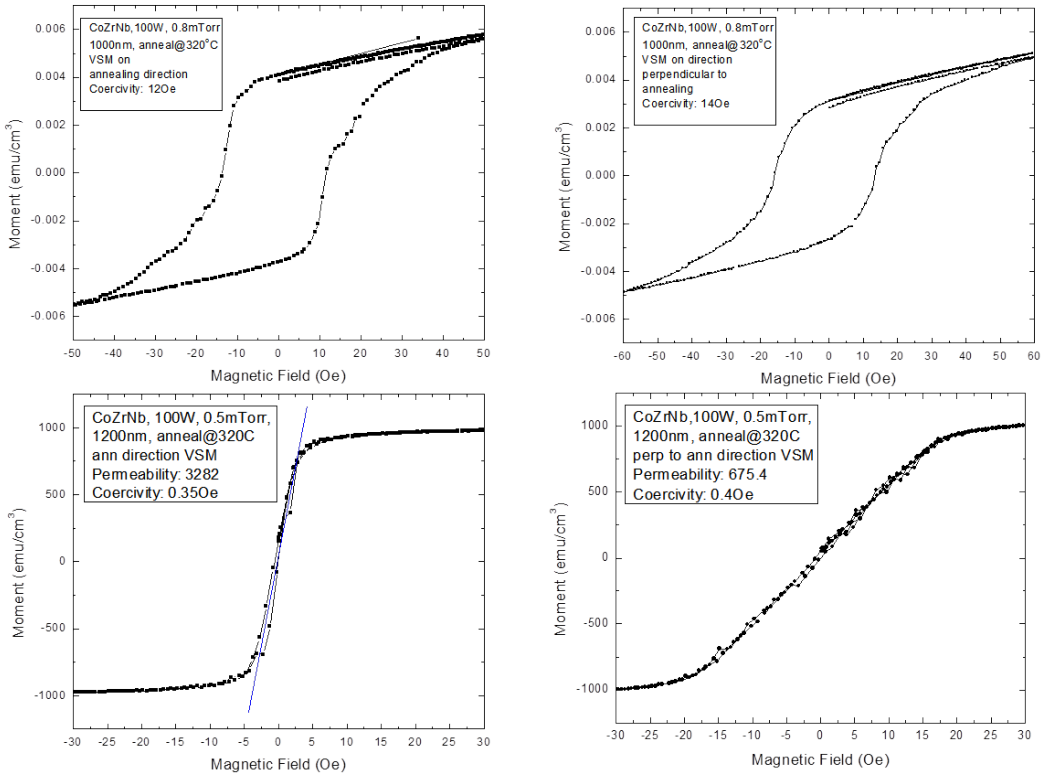

Figure 4.3 The VSM results for 1200nm CoNbZr at different sputtering pressure. Two 1200nm films are fabricated at the same sputtering power but different sputtering pressure. One is at 0.8mTorr and the other is at 0.5mTorr. Obviously 0.5mTorr one shows extremely low coercivity.

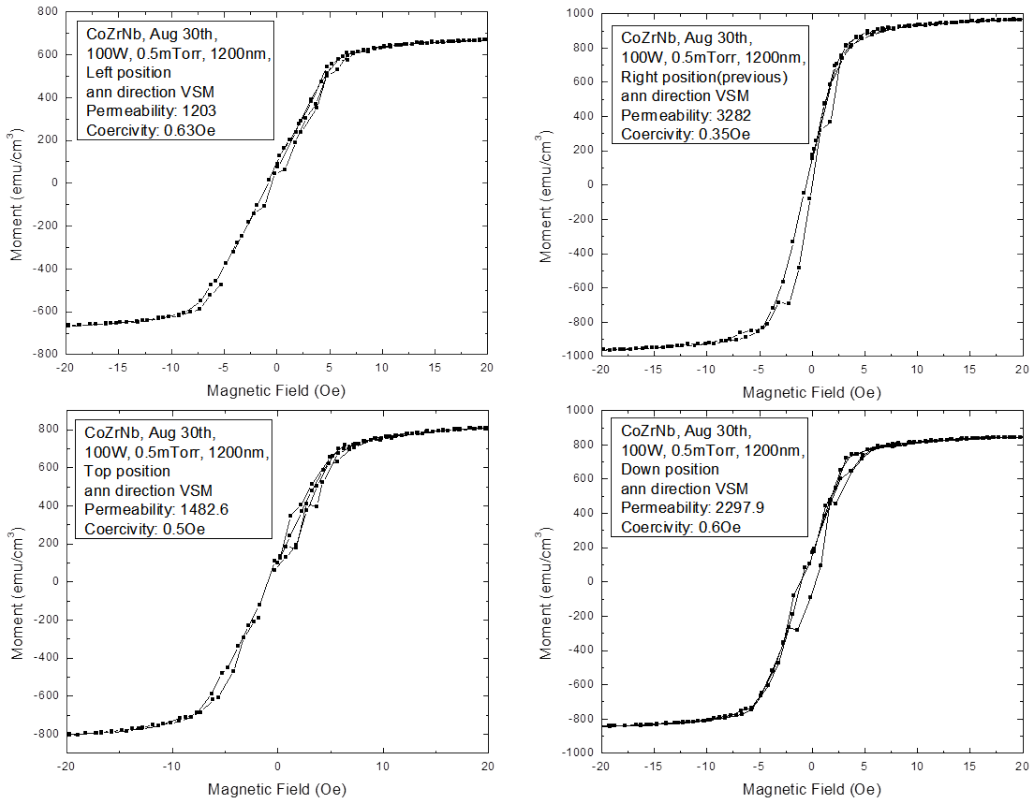

Figure 4.4 The VSM study on coercivity distribution. The CoZrNb will be sputtered over 2inch wafer. The magnetic property of CoZrNb all over the wafer area has been measured. Magnetron sputtering produces uniform and high quality CoZrNb thin film.

Through much effort, thin films of $Co_{88}Nb_8Zr_4$ with the best magnetic properties are fabricated at sputtering pressure of 0.6mTorr pure Argon, 63W DC power which corresponds to 0.15A current and 420V voltage. The whole wafer has the same quality and no local distribution is observed, shown in Figure 4.4. Annealing study shows that annealing has no contribution to the film quality if it is already high permeability and no coercivity as deposited film. This is a good property for generating devices. As we mentioned before, the magnetic annealing is the required step for fabricating MTJ devices. If the film properties of CoNbZr can be affected by annealing, it will be changed

during MTJs annealing process. Or if the film of CoNbZr requires annealing, its annealing process will change MTJ properties.

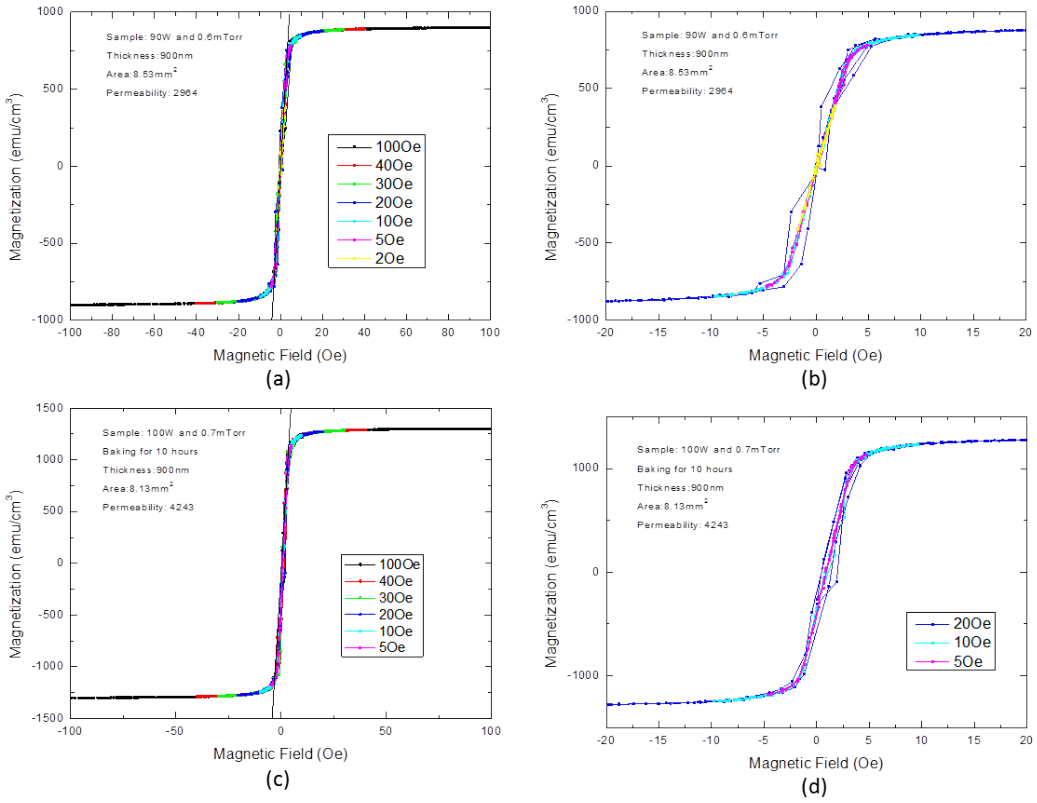

Figure 4.5 (a) and (c) show two example VSM results for good samples. (b) and (d) are the enlarged view with lower magnetic range. (There seems certain coercivity due to data fluctuation. However it is due to the swiping mode. The results have been verified using persistent mode using PPMS.)

Figure 4.5 already verified CoNbZr in continuous thin film form with low coercivity and high permeability is successfully fabricated utilizing our high vacuum magnetron sputtering technique. However, as we mentioned, the magnetic properties are also sensitive to the geometry because of shape anisotropy. This is already verified in Figure 4.2 where the magnetic anisotropy is affected by the film thickness. So far, continuous thin film of CoNbZr on fresh smooth SiO_2 wafer has been successfully fabricated. It is

still challenging to achieve the same magnetic properties for thin film with specific geometry on patterned or processed substrates. In our fabrication procedure, the FC thin film will be deposited in the last step using lifting off method. There is a lot of photoresist residue, observed by AFM, on the substrate after photolithography. Therefore, ion milling is introduced to remove the residue and activate the substrate area where $Co_{88}Nb_8Zr_4$ will be deposited. Finally, we can consistently fabricate $Co_{88}Nb_8Zr_4$ thin film on substrate which already went through MTJ patterning.

From Maxwell's equations in CGS units, material's permeability can be calculated by $\mu=B/H=4\pi M/H+1$ where B is the magnetic field and H is the magnetizing field. The material $Co_{88}Nb_8Zr_4$ has the permeability varying from 1000 to 7000 from different literature. In our result the permeability can reach 4.9×10^3 with nearly zero coercivity. Very small external magnetic field could induce huge magnetization in this material, which makes it the good material for flux concentrator.

4.3 Flux Concentrator and Its Photomasks

With the permeability of $Co_{88}Nb_8Zr_4$ extracted from VSM measurement, we performed simulation for a normal flux concentrator configuration using the software, Comsol Multiphysics. It verified that the gain factor (or amplification factor) is proportional to the length to gap ratio (h/Δ). A specific configuration result is presented in Figure 4.6 where the height of the trapezoid was set as 80 μm, the gap 4 μm, and the thickness of flux concentrator 2 μm. The external magnetic field can be amplified by a factor of 23.25 in its central gap.

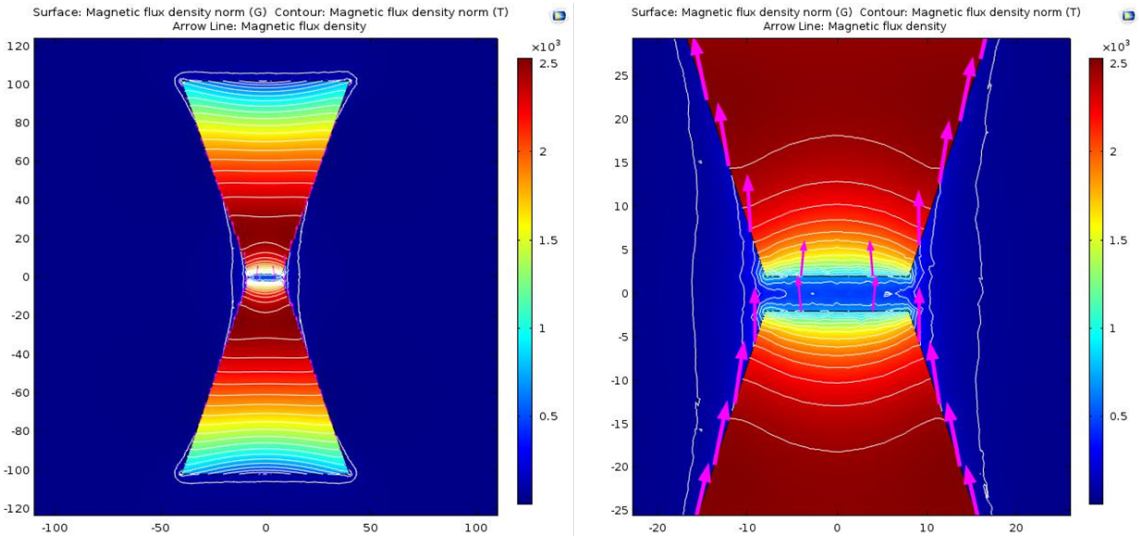

Figure 4.6 The Comsol simulation result.

The design is finalized based on the following parameters.

(1) The unit cell is 1mm by 1mm.

(2) The magnetic tunneling junction size is chosen to be 15um by 120um ellipse shape based on our previous study. Oval shape can provide the shape anisotropy which help to achieve linear and reversal transfer curve. The ratio between long and short axis of this oval shape has been optimized based on all the parameters as coercivity, dynamic range and noise level.

(3) The processing method is the photolithography. Our photolithography resolution defined by the equipment is about 5um. The dimension of electrodes has to be larger than 80um for wire-bonding or probe measurement.

Taking all the factors into consideration, we design 4 MTJs in series in the gap. Most of the area is used for flux concentrator except the least area needed for electrodes. The thickness of $Co_{88}Nb_8Zr_4$ is chosen to be 1um.

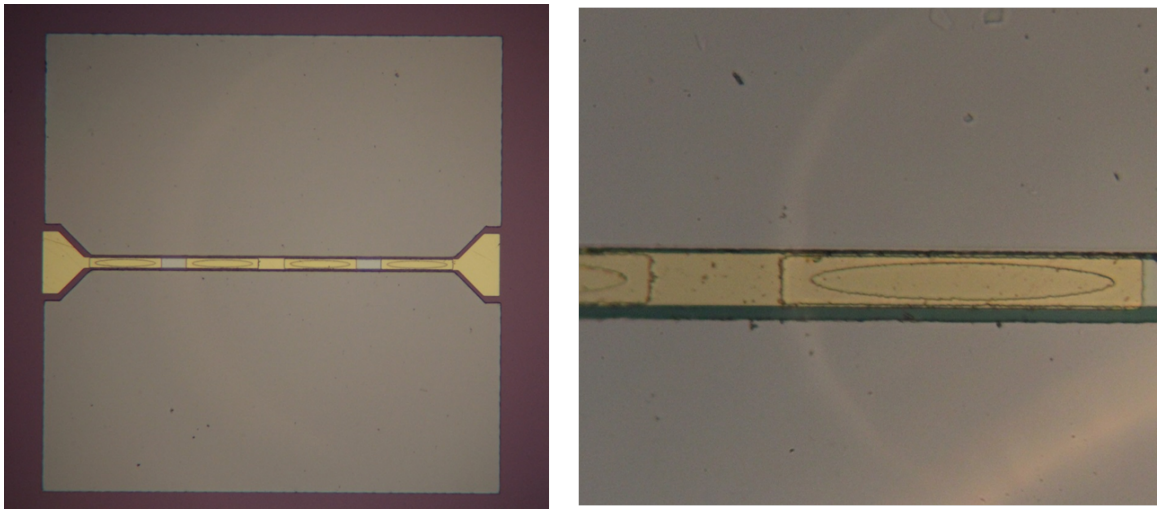

Figure 4.7 The photo image of our sample. The oval shape is the sensor area. The gold color is the electrodes. The flux concentrators are sitting aside.

4.4 Sample Fabrication

The MTJ fabrication is the same as before. The annealing direction is along the short axis to make it in sensor mode. The lift-off method is used for fabricating flux concentrators. Photolithography is first applied to open the window area for the material to be deposited. As we mentioned before, ion milling has to be used to remove the residue of photoresist in the window area before the deposition.

4.5 Characterization for MTJ sensor with Flux Concentrator

The linear transfer curve measurement is applied to study our sample because it can give MR ratio, coercivity, sensitivity and saturation field all together. Even though there are only 4 MTJ sensors in series, the sample is robust and the MR is generally as high as 100%. By incorporating FCs of $Co_{88}Nb_8Zr_4$, the coercivity has been reduced to around 0.3Oe and the sensitivity has been increased to around 15%/Oe to 20%/Oe. The

conventional MTJ sensors only have the sensitivity around 0.5%/Oe to 1%/Oe. In our group through annealing optimization we have achieved the MTJ sensors with sensitivity of 3.3%/Oe at room temperature [14]. There are a few measurement examples showing in Figure 4.8.

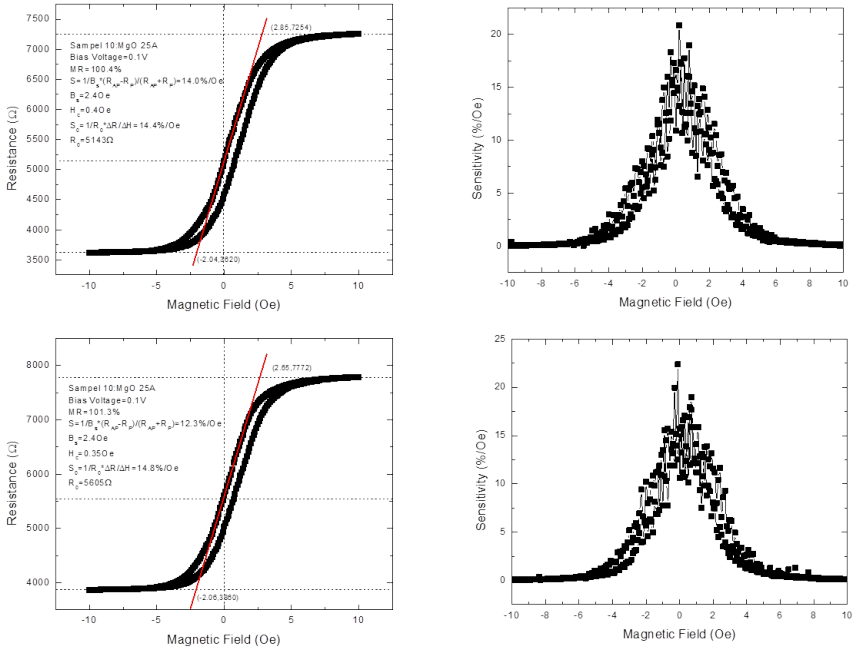

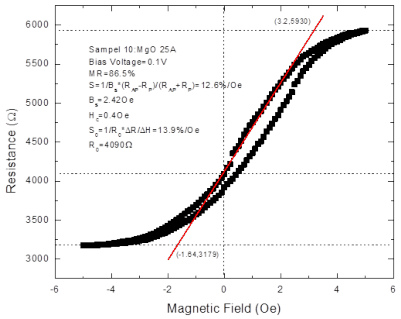
Sampel 10:MgO 25A
Bias Voltage=0.1V
MR=86.6%
S=1/B_s*(R_AP-R_P)/(R_AP+R_P)=12.6%/Oe
B_s=2.42Oe
H_c=0.4Oe
S_c=1/R_c*ΔR/ΔH=13.9%/Oe
R_c=4090Ω
(3.2,5930)
(-1.64,3179)
Resistance (Ω)
Magnetic Field (Oe)

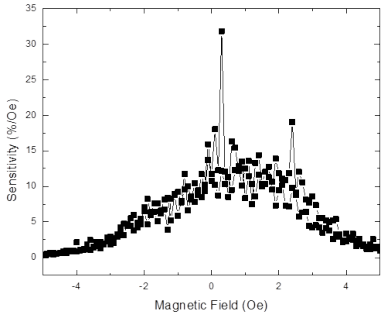
Sensitivity (%/Oe)
Magnetic Field (Oe)

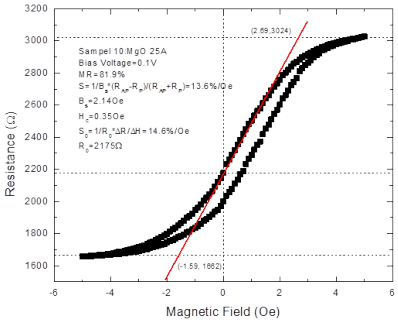
Sampel 10:MgO 25A
Bias Voltage=0.1V
MR=81.9%
S=1/B_s*(R_AP-R_P)/(R_AP+R_P)=13.6%/Oe
B_s=2.14Oe
H_c=0.35Oe
S_c=1/R_c*ΔR/ΔH=14.6%/Oe
R_c=2175Ω
(2.69,3024)
(-1.59,1662)
Resistance (Ω)
Magnetic Field (Oe)

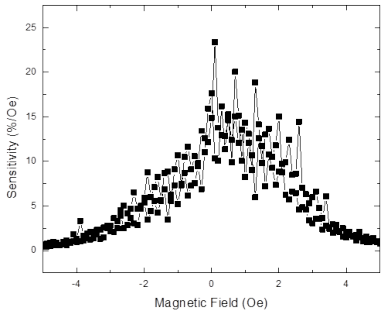
Sensitivity (%/Oe)
Magnetic Field (Oe)

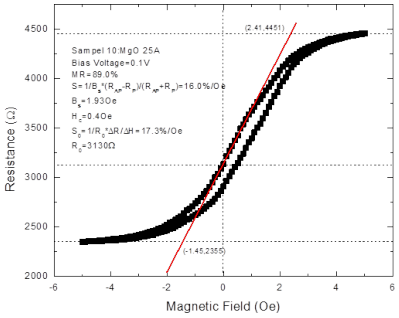
Sampel 10:MgO 25A
Bias Voltage=0.1V
MR=89.0%
S=1/B_s*(R_AP-R_P)/(R_AP+R_P)=16.0%/Oe
B_s=1.93Oe
H_c=0.4Oe
S_c=1/R_c*ΔR/ΔH=17.3%/Oe
R_c=3130Ω
(2.41,4451)
(-1.45,2355)
Resistance (Ω)
Magnetic Field (Oe)

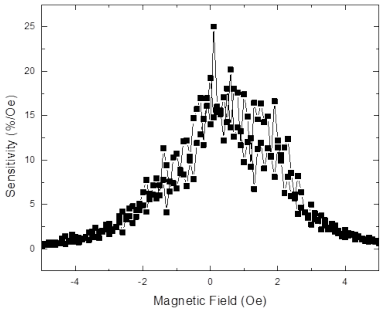
Sensitivity (%/Oe)
Magnetic Field (Oe)

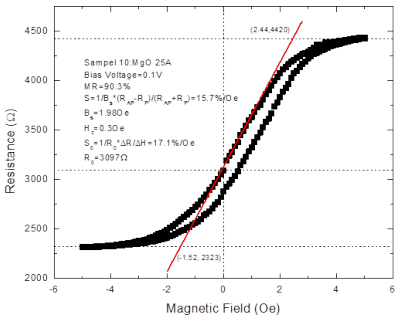
Sampel 10:MgO 25A
Bias Voltage=0.1V
MR=90.3%
S=1/B_s*(R_AP-R_P)/(R_AP+R_P)=15.7%/Oe
B_s=1.98Oe
H_c=0.3Oe
S_c=1/R_c*ΔR/ΔH=17.1%/Oe
R_c=3097Ω
(2.44,4420)
(-1.52,2323)
Resistance (Ω)
Magnetic Field (Oe)

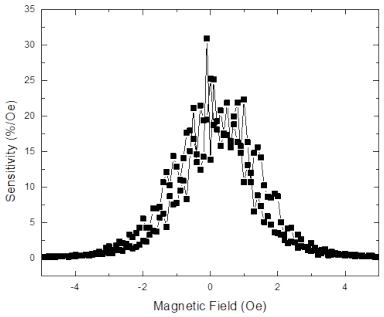
Sensitivity (%/Oe)
Magnetic Field (Oe)

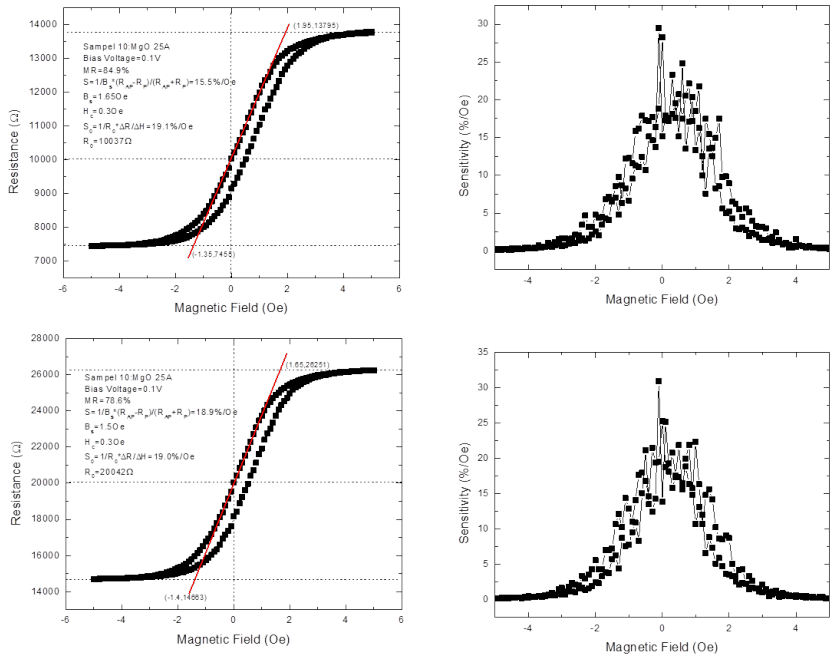

Figure 4.8 The examples of measurements of linear transfer curve measurement (on the left) and the dynamic sensitivity (on the right). The coercivity has been reduced to around 0.3Oe and the sensitivity has been increased to 15%/Oe.

4.6 Double Stage Flux Concentrator

In order to further increase the sensitivity, we have included additional magnetic concentrators outside of the MTJ devices. Conetic, $Ni_{77}Fe_{14}Cu_5Mo_4$, is soft magnetic material which is also used in our free layer of MTJs. A pair of Conetic pieces is placed on top of thin-film FCs. The thickness is 0.025 inch. The needle width is 1mm and the maximum width is 1cm. A few pairs with different length have been measured. The sensor is sitting in the center of the gap between two Conetic pieces. Figure 4.9 shows the image of Conetic pieces and the configuration of the double stage flux concentrator.

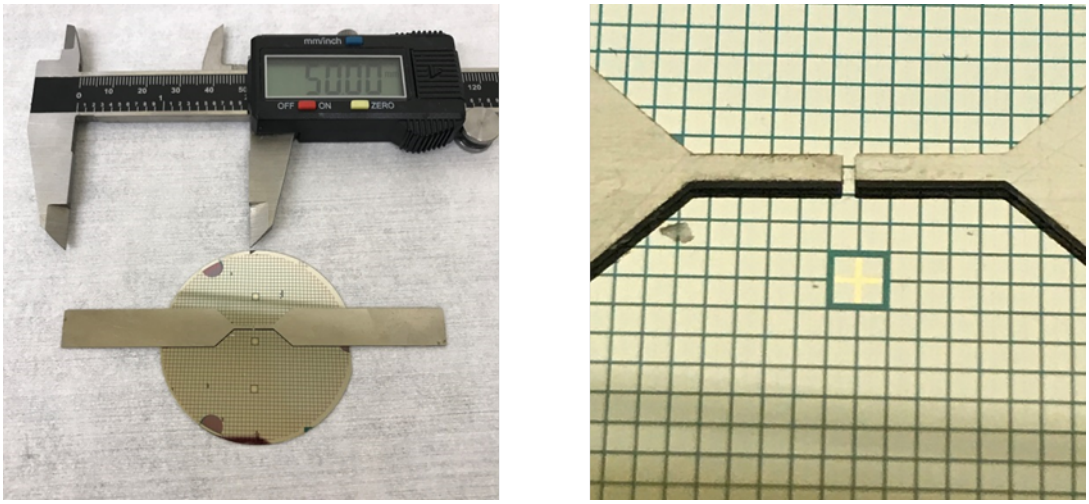

Figure 4.9 The images of our secondary flux concentrator made by Conetic material. The measurement is done through a breakout board with the wire bonding.

A small piece of the sample was fixed on a breakout board. The wire bonding was made between sample electrodes and pads of the breakout board. Two Conetic pieces were carefully aligned along the short axis of the sensors under the microscope and mounted tight using glue. The separation can be adjusted manually. The magnetic field was provided by a large Helmholtz coil to make sure magnetic field uniform over the sample and Conetic pieces area.

First of all, the magnetic properties of Conetic were measured using VSM shown in Figure 4.10. VSM measurement was carried along the short axis and long axis for a small rectangular piece. There is no obvious coercivity for both orientations. Even though the permeability is low for that small piece, the permeability of the large piece will be different since it is shape-dependent.

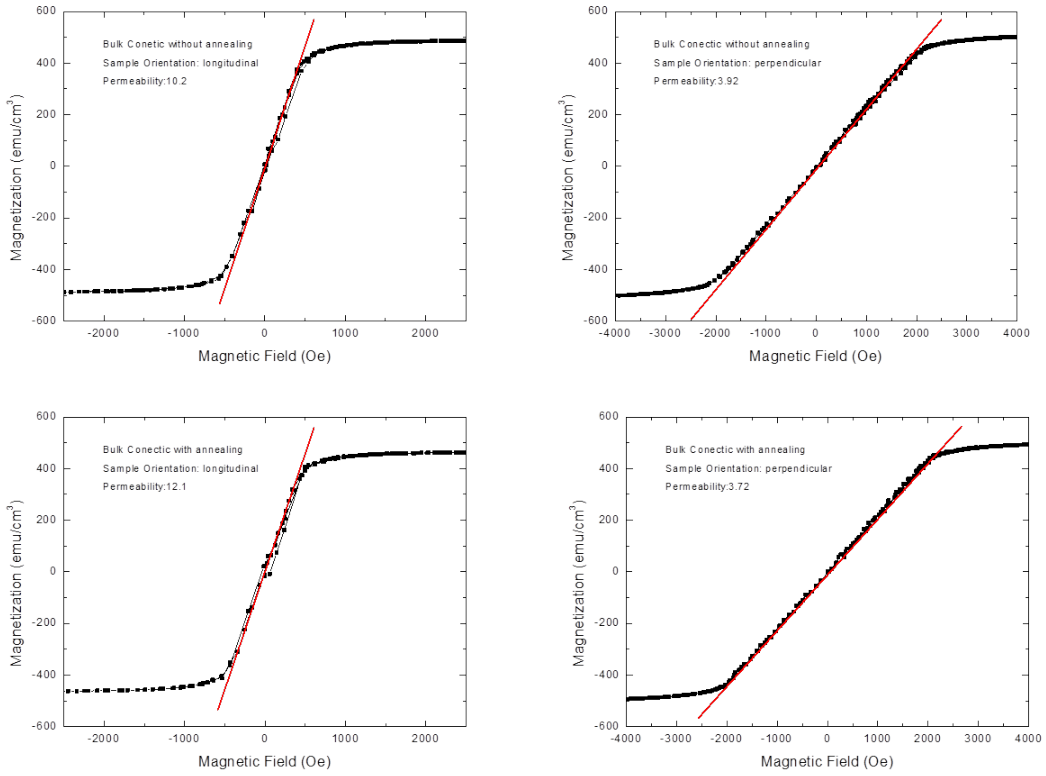

Figure 4.10 The VSM measurement of Conetic metal piece. The size is 1×5mm. VSM measurement is carried out along both short axis and long axis. There is no coercivity for both directions. The slopes which represent the permeability are different.

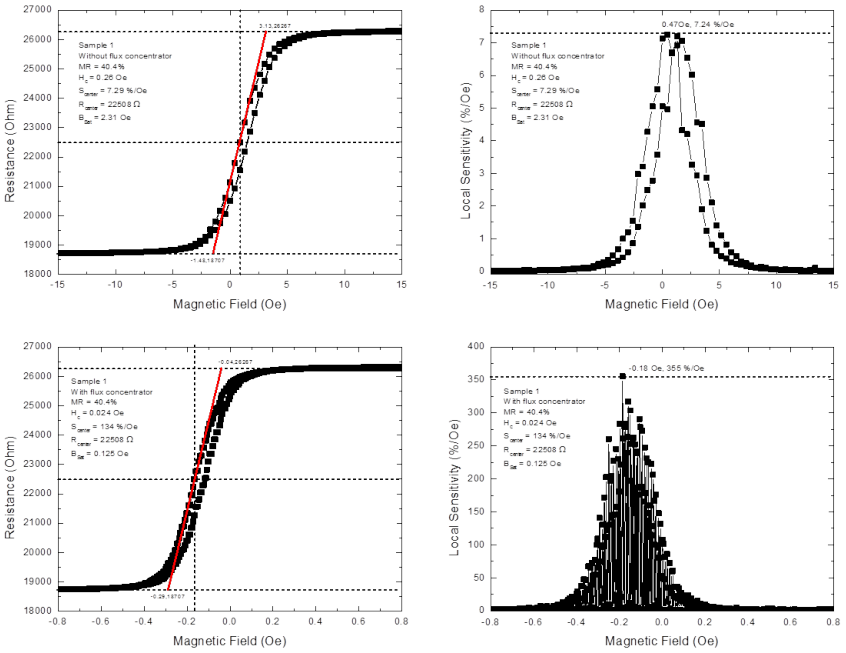

(a) Sample 1.

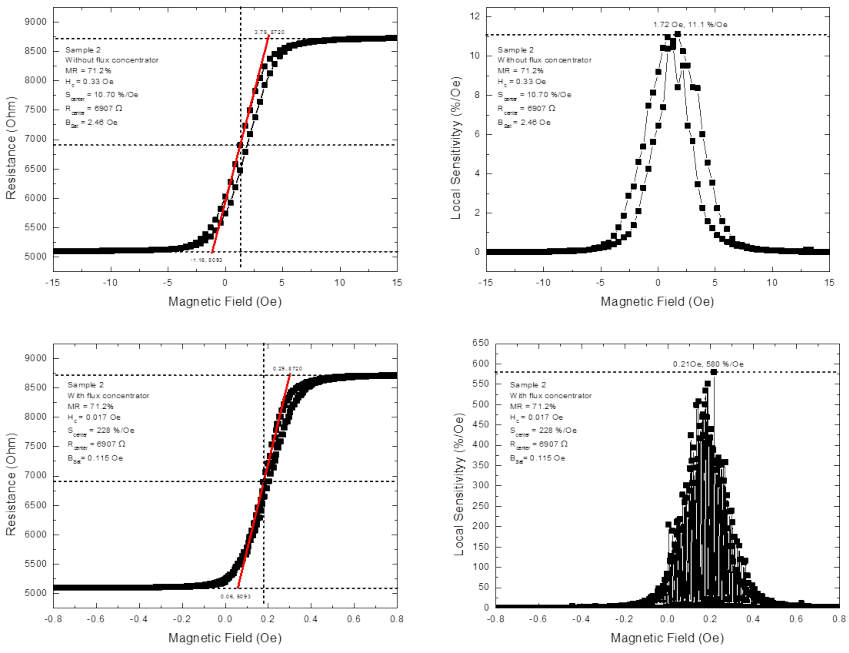

(b) Sample 2.

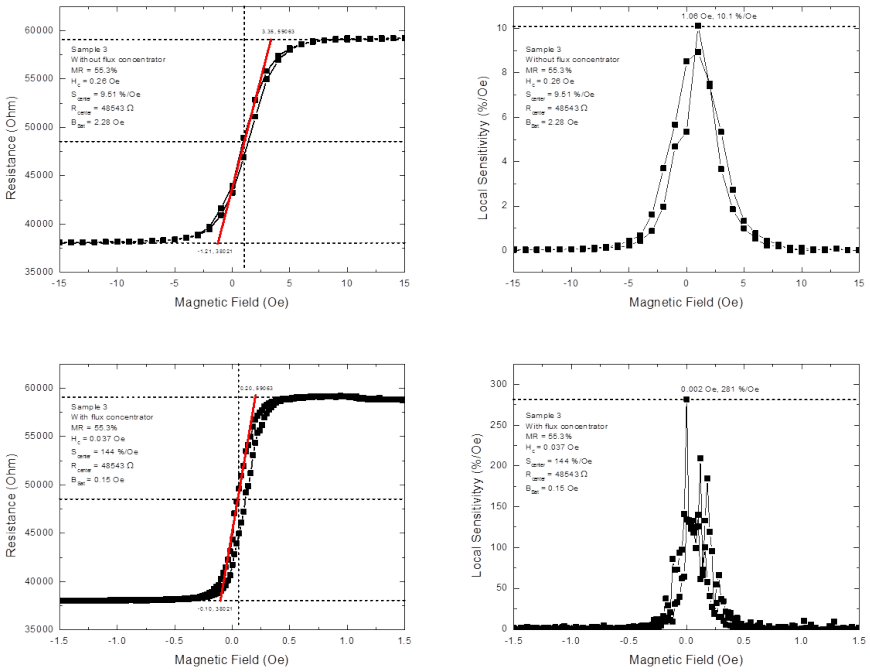

(c) Sample 3.

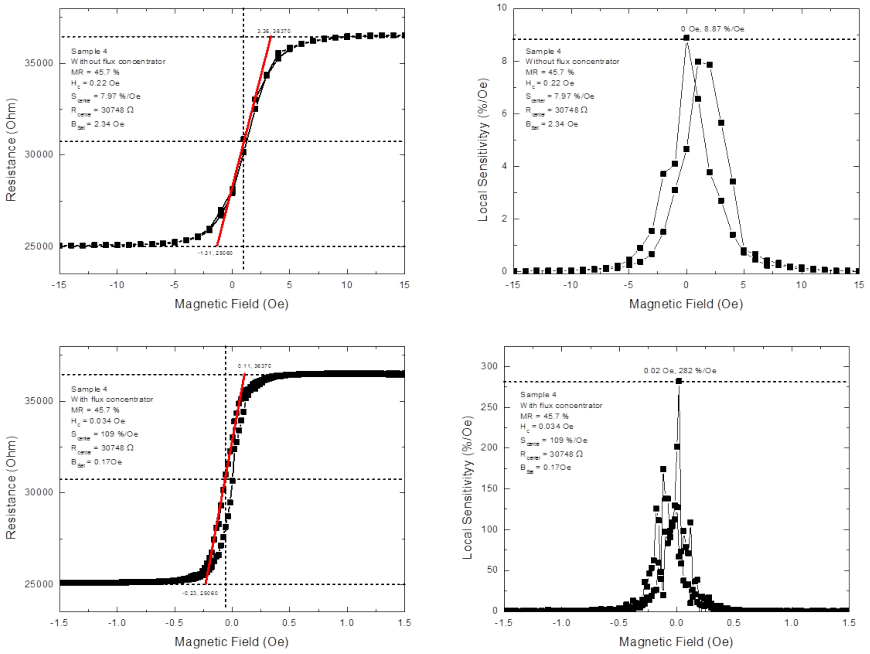

(d) Sample 4.

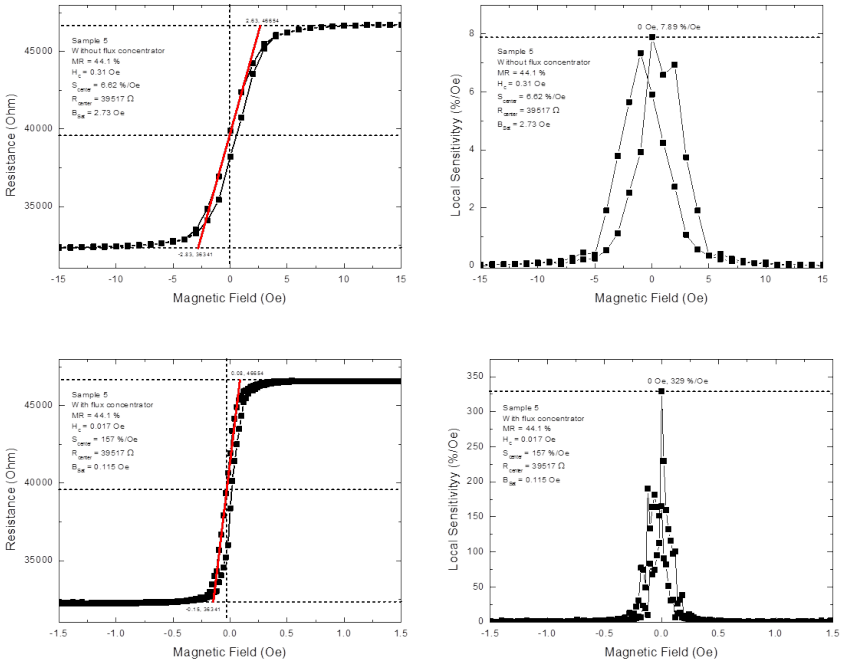

(e) Sample 5.

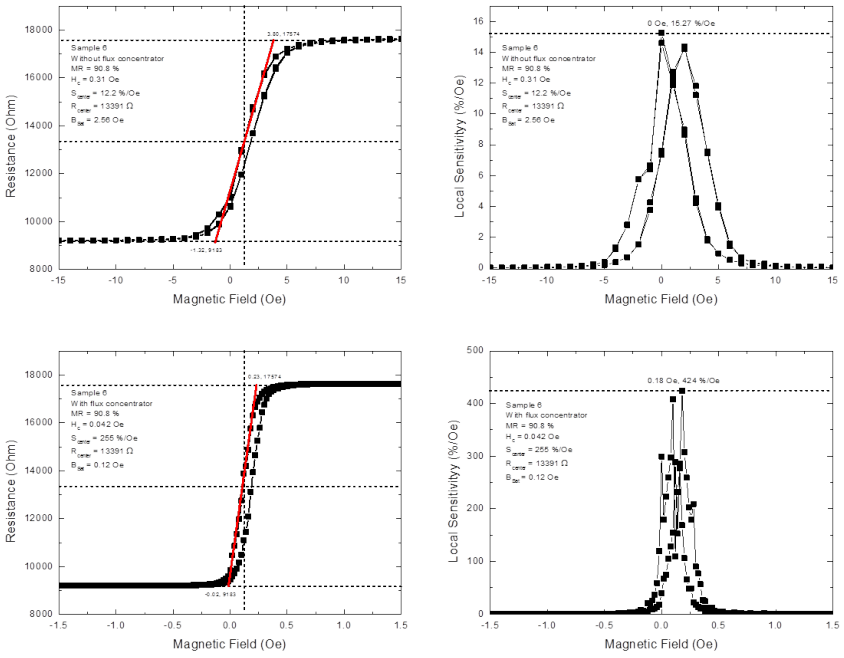

(f) Sample 6.

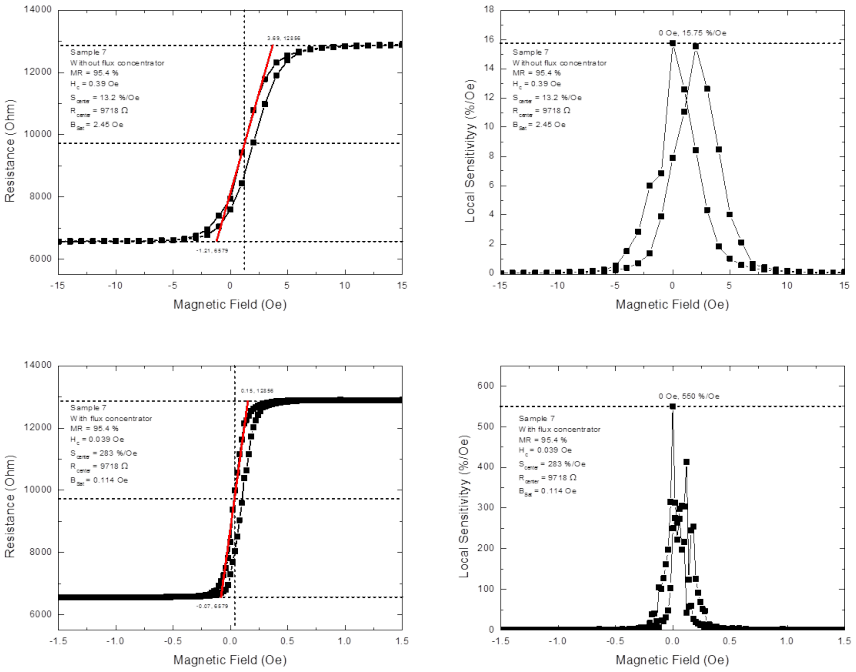

(g) Sample 7.

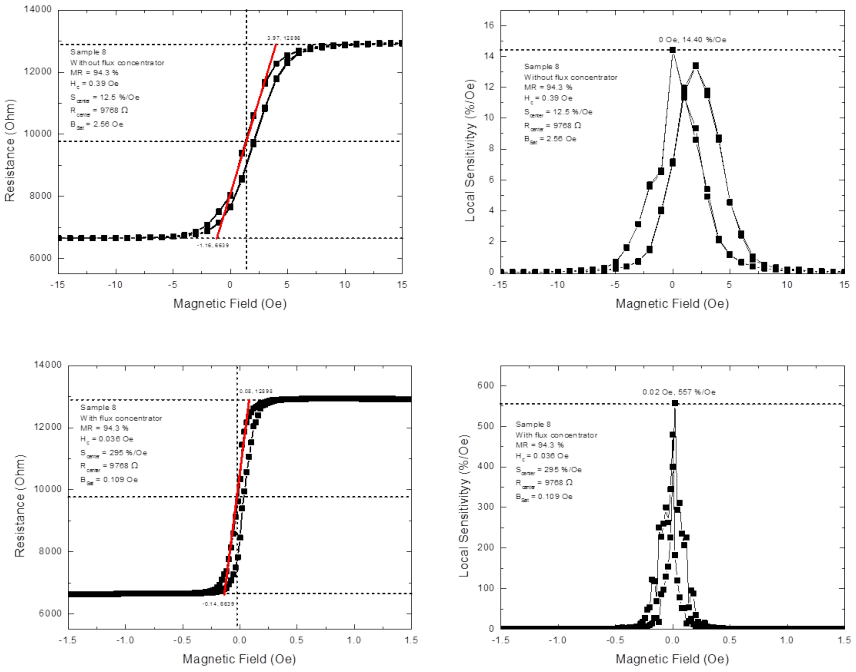

(h) Sample 8.

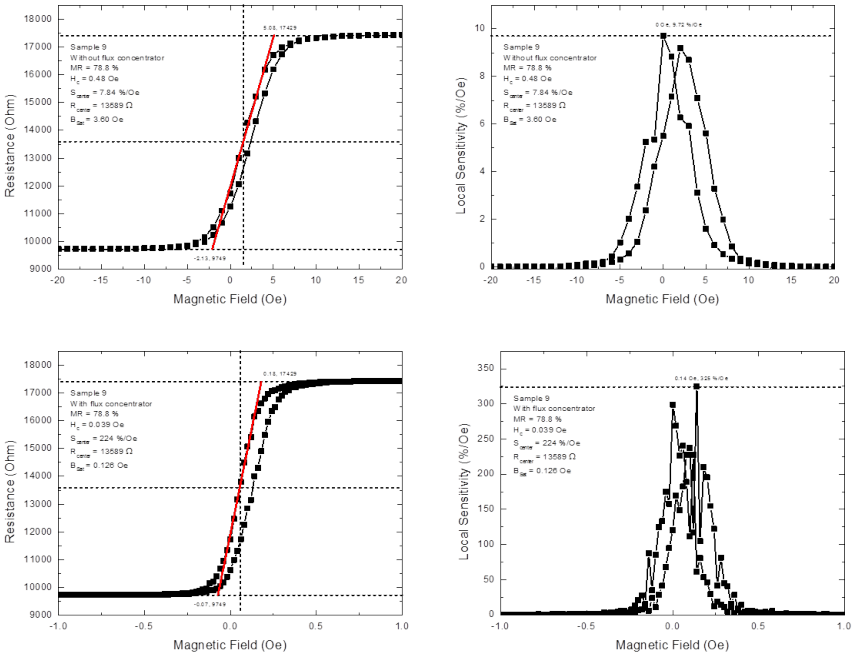

(i) Sample 9.

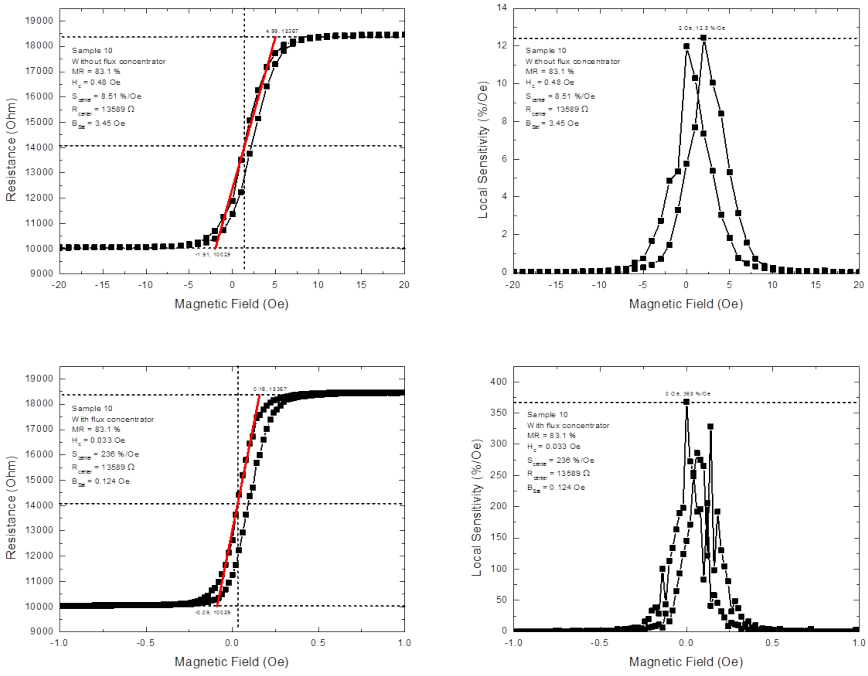

(j) Sample 10.

Figure 4.11 For each sample, the top left is the transfer curve measurement only with FCs of NbCoZr and the top right is the local sensitivity. The bottom left is the transfer curve measurement with the double-stage FCs including both thin-film FCs and Conetic pieces. The bottom right is the local sensitivity.

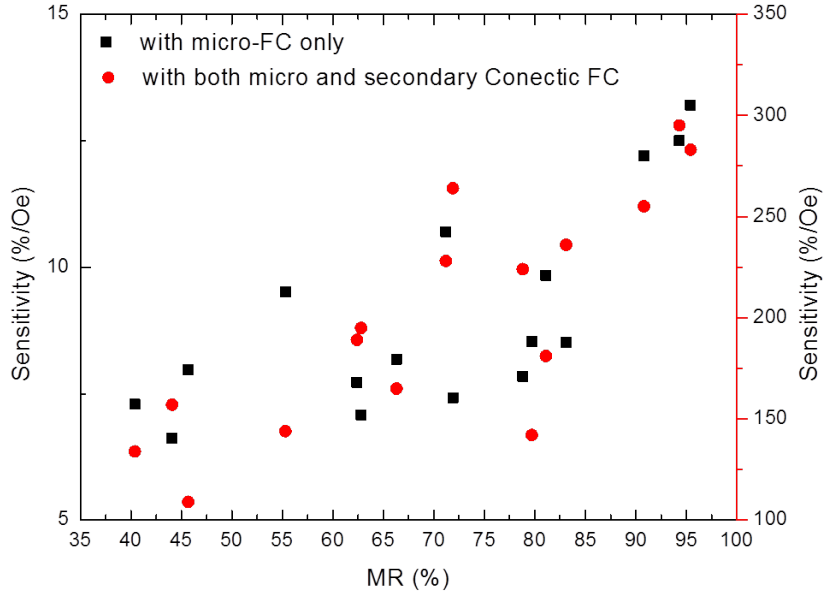

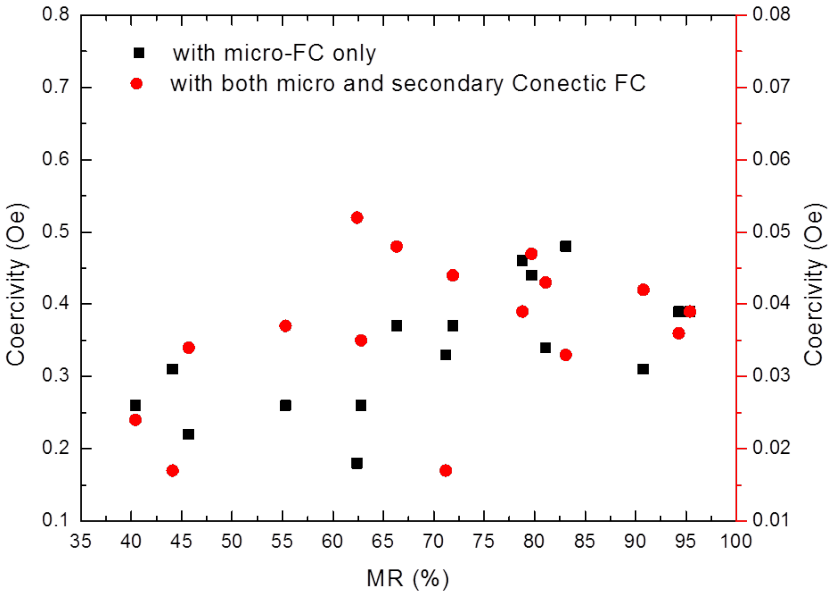

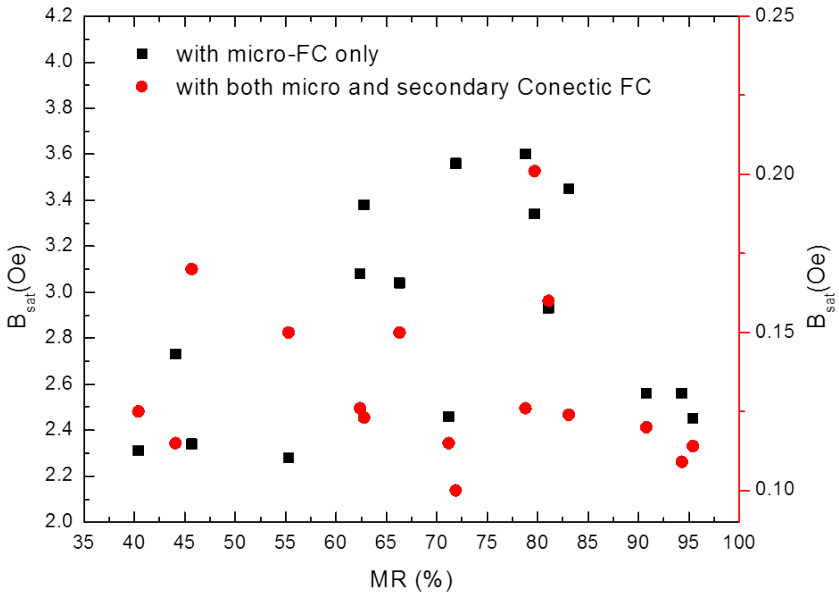

Figure 4.12 The statistical plot of sensitivity, coercivity and saturation field for each sample with thn-film FCs only and both two-stage FCs. These three parameters have been tremendously improved.

For each sample, two transfer curves with and without the secondary FC stage (Conetic pieces) are measured. A few examples are presented in Figure 4.11. The separation between two Conetic pieces is roughly 0.5mm. With these two-stage FC, the sensitivity has been increased to 100~300%/Oe and the coercivity has been reduced to 0.02~0.05Oe.

4.7 Summary

In conclusion, we successfully used FC method and improved performance of our MTJ sensors. Thin film of $Co_{88}Nb_8Zr_4$ with high permeability and no coercivity has been fabricated using magnetron sputtering system. Furthermore, it was successfully added to our MTJ sensors through photolithography method. The sensitivity was increased to

20%/Oe and the coercivity was reduced to 0.3Oe. Based on this new design, we added additional magnetic concentrators made of Conetic alloy outside of our MTJ devices. The sensing capability has been significantly increased. The best sensitivity we achieved was 557%/Oe, which is 500 times larger than the conventional MTJs. The magnetic saturation field was only around 0.1Oe. This is the best performance sensor ever reported without biasing field. We are expecting even further improvement if we can optimize all geometric parameters.

Reference

1. B. Kaplan and U. Suissa, Radio Science **33** (6), 1517 (1998).

2. P. M. Drljača, F. Vincent, P.-A. Besse and R. S. Popović, Sensors and Actuators A: Physical **97**, 10 (2002).

3. A. Guedes, J. Almeida, S. Cardoso, R. Ferreira and P. Freitas, IEEE transactions on magnetics **43** (6), 2376 (2007).

4. T. Takahashi, M. Yoneda and M. Naoe, Japanese Journal of Applied Physics **28** (3R), 379 (1989).

5. T. Takahashi, N. Ikeda and M. Naoe, Journal of Applied Physics 69 (8), 5011 (1991).

6. H. De Wit, C. Witmer and F. Dirne, IEEE transactions on magnetics **23** (5), 2123 (1987).

7. M. Miura, H. Katahashi, K. Muramori and M. Kajiyama, IEEE Transactions on Magnetics **24** (5), 2215 (1988).

8. Y. Shimada and N. Saito, Japanese journal of applied physics **25** (3R), 419 (1986).

9. K. Choh, J. Judy and J. Sivertsen, Journal of applied physics **64** (10), 5495 (1988).

10. Y. Kim, K. Ishiyama and K. Arai, IEEE transactions on magnetics **35** (5), 3394 (1999).

11. T. Takahashi, N. Ikeda and M. Naoe, Journal of Applied Physics **69** (8), 5011 (1991).

12. F. Machizaud, G. Suran, M. Rivoire and F. Dirne, Journal of materials science **26** (11), 3025 (1991).

13. I. Trindade, D. Leitao, Y. Pogorelov, J. Sousa, R. Chaves, S. Cardoso and P. Freitas, Applied Physics Letters **94** (7), 073501 (2009).

14. D. Mazumdar, X. Liu, B. Schrag, W. Shen, M. Carter and G. Xiao, Journal of applied physics **101** (9), 09B502 (2007).

Chapter 5
A Heterojunction composed by doped Mott Insulators

In this chapter a heterojunction composed by $La_{1.9}Sr_{0.1}CuO_4$ thin film on a 0.5wt% Nb doped $SrTiO_3$ single-crystal substrate was fabricated using high vacuum magnetron sputtering system with a high-temperature heater. All the experiment details were reviewed. The component thin film and the substrate were characterized independently. We studied the heterojunction's rectification and temperature dependency. In the end, the capacitance of the junctions over a broad frequency range under different bias voltages were investigated and discussed.

5.1 Motivation and Introduction

The bulk properties of doped Mott insulator material have been investigated for decades. For example, scientists have conducted good studies about how the doping level will affect the superconducting temperature of bulk system $La_{2-x}Sr_xCuO_4$. Because of the fabrication difficulty, the heterojunctions composed by doped Mott insulators have not attracted too much attention compared to their bulk system. However, interesting phenomena are highly expected in this artificial interface composed by this strong correlated electron system.

More recently, a few theoretical works about heterojunctions composed of doped Mott insulators have predicted some distinguishing properties, for example, high quantum efficiency [1] and high-frequency rectification [2]. More and more experimental works also verified the unconventional interesting interfacial properties [3, 4].

We chose to study a heterojunction composed by a $La_{1.9}Sr_{0.1}CuO_4$ thin film on a 0.5wt% Nb doped $SrTiO_3$ single-crystal substrate because of the simplicity. We conducted theoretical simulations and experimental characterization of these heterojunctions. Most of the literature is focused on how superconductivity affects the characteristics of heterojunctions. The change of the junction resistance, capacitance and diffusion voltage are typically observed during the occurrence of superconductivity [3, 5]. In our system, $La_{1.9}Sr_{0.1}CuO_4$ is non-superconducting due to oxygen deficiency. We reported the synthesis of a heterojunction of $La_{1.9}Sr_{0.1}CuO_4$ thin film on 0.5wt% Nb doped $SrTiO_3$ and investigated the electrical transport and capacitance properties.

5.2 Experimental Methods

The principal experimental techniques were introduced in the sequence of the fabrication of the heterojunction comprising of a $La_{1.9}Sr_{0.1}CuO_4$ thin film on a 0.5wt% Nb doped $SrTiO_3$ single-crystal substrate. They include the equipment setup, target preparation, substrate pretreatment, multilayer deposition, thermal annealing, lead deposition, photolithography and ion milling etching.

5.2.1 Equipment Setup

$La_{1.9}Sr_{0.1}CuO_4$ films were deposited on treated (001) orientated 0.5wt% Nb doped $SrTiO_3$ single crystal substrates using our magnetron sputtering system. The deposition happens when the substrate is sitting at 800^0C. The sputtering pressure is 20mTorr with 50% oxygen in argon. We were only able to do the deposition when the substrates were sitting in ambient temperature. In order to do high-temperature deposition, modification has to be done to our sputtering system.

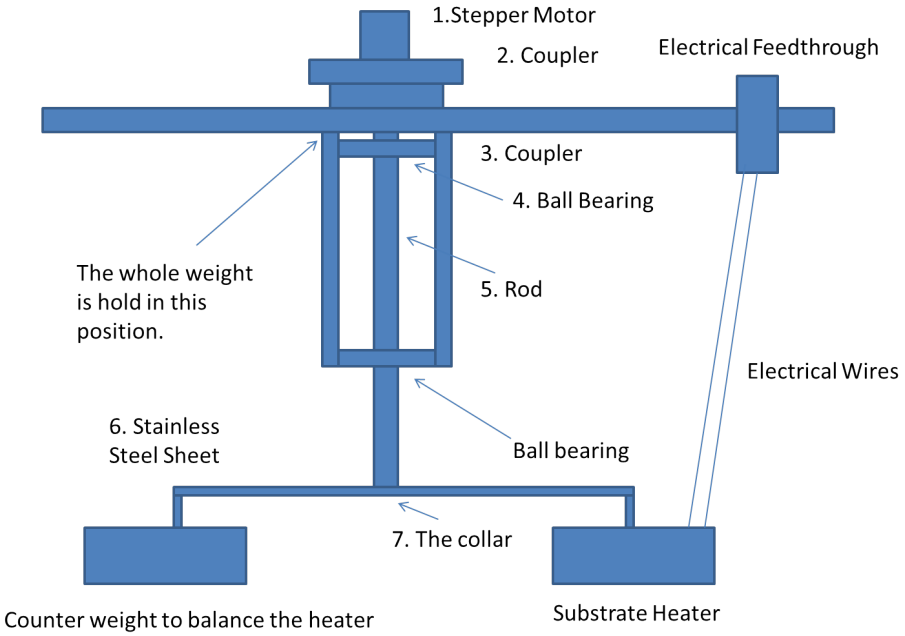

Figure 5.1 Illustration of high-temperature substrate holder.

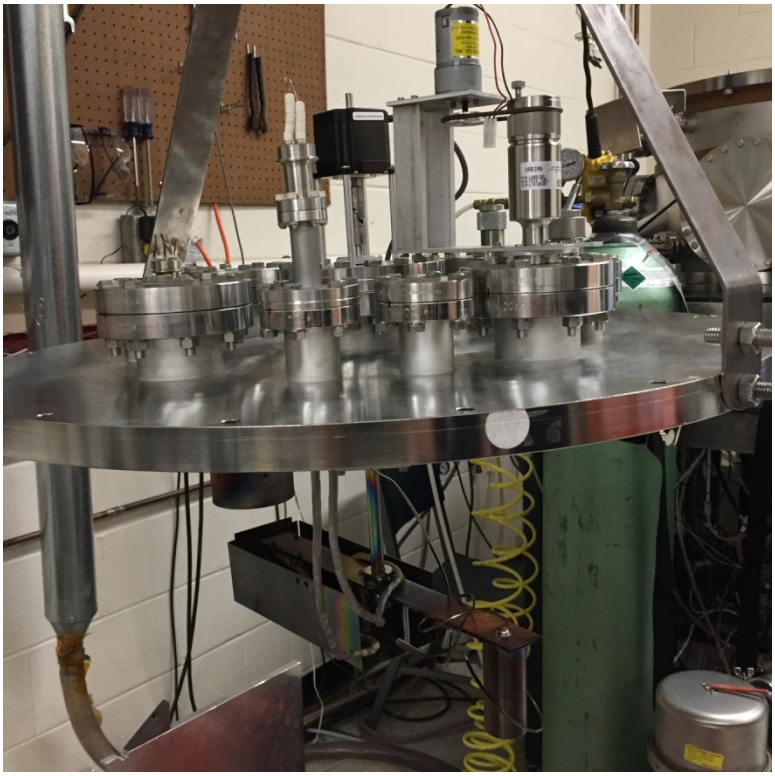

Figure 5.2 The picture of modification done to the vacuum chamber.

In order to realize the high temperature deposition, a high temperature substrate heater has to be installed inside the vacuum chamber with a position controller. A stepper motor was installed outside of the chamber and through a vacuum rotary feedthrough it can provide accurate position control for the substrate heater. The heater was purchased from MeiVac Inc. It was made by special material which can be used in high vacuum systems and can provide the temperature up to 950^0C. The design is presented in Figure 5.1. The heater power supply, sitting outside of the chamber, was connected to the substrate heater in the vacuum through an electrical feedthrough. During the deposition, the substrate attaching to the heater was rotated to the target place by the stepper motor through computer control.

5.2.2 Target Preparation

$La_{1.9}Sr_{0.1}CuO_4$ target was prepared using the traditional solid state reaction method. The target which can be applied in our sputtering system has a 2 inch diameter with 1/8 inch thickness. Based on this target's dimension and atomic ratio, the amount of pure La_2O_3, $SrCO_3$ and CuO powder can be calculated. All the powders were carefully weighted and well mixed in a clean mortar. The mixture is a critical step to create a good quality target. A 5-ton weight was applied to compress the powders into the target shape. The compressed target was placed in the oxygen furnace and annealed at 950^0C in air for 12 hours [6, 7]. After this, the reaction happened thoroughly and the target became black. Before installing the target into the sputtering system, XRD was applied to check the resulting compounds of the target to make sure no contamination or impurities.

5.2.3 Substrate Pretreatment

In this project, 0.5wt% Nb doped $SrTiO_3$ (NSTO) single-crystal is selected as the substrate. It is a common commercial substrate. However, there are a few tricks to make good use of it.

The commercial NSTO substrate usually contains both SrO-terminated and TiO_2-terminated regions. TiO_2-teminated NSTO substrates are the prerequisite for reproducible epitaxial film growth [8, 9] because TiO_2 in anatase phase can provide smaller lattice mismatch. A fully TiO_2-terminated NSTO can be achieved through a chemical and subsequently thermal treatment. The treatment procedure is as follows:

1. Clean

Sonicate in acetone for 5 min, rinse in Methanol, Sonicate in D.I. water for 5 min.

2. Etch

Sonicate in D.I. water for 10 min at room temperature.

Dip in BHF (pH ~4.0) for 35 seconds.

Rinse in D.I. water.

Rinse in Methanol.

3. Anneal

Anneal in air 950°C for 1 hour and naturally cool down to the room temperature.

During this process, SrO can react with H_2O and CO_2 to form $SrCO_3$ and $Sr(OH)_2$ which then dissolve in Buffered HF, leaving the pure TiO_2-terminated surface.

The miscut of the substrate will affect the annealing time dramatically. A small difference in miscut has a significant influence on the terrace length. The lower miscut can cause an exponential increase of the terrace length and the annealing time. In our treatment procedure, 1-hour annealing time is specifically for a miscut between 0.1^0-0.2^0. When we order the substrates, we have to specify the material, doping level and orientation of the substrate, and the miscut.

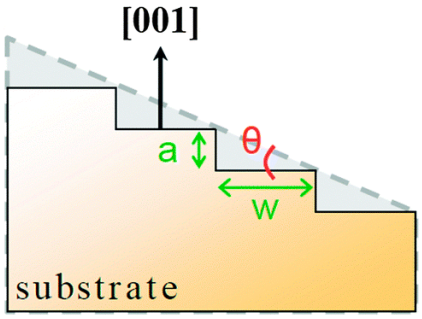

Figure 5.3 Illustration of the definition of miscut θ. The miscut can determine the terrace length w by a/tanθ where a is the unit cell height.

The morphology of the NSTO substrate, before and after the treatment, was checked using atomic force micrograph (AFM). The images are shown in Figure 5.4. After the treatment, NSTO showed a clean surface without visible particles. The AFM results also verified the terrace height which is 0.4nm. So far, pure TiO_2-teminated NSTO substrates have been obtained.

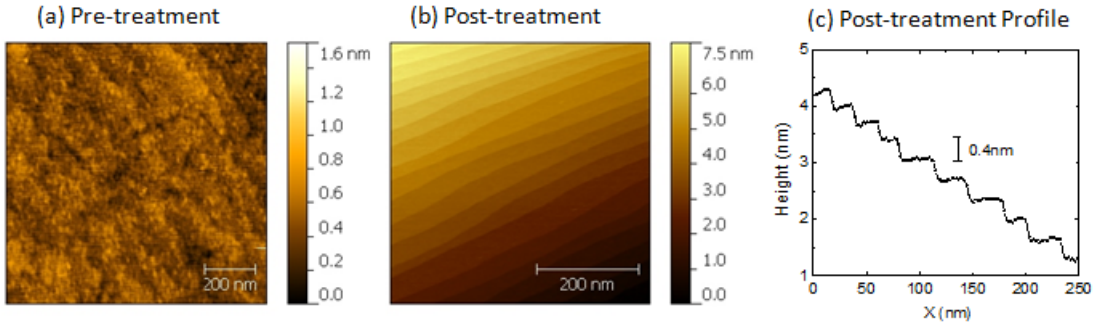

Figure 5.4 a) Pre-treatment. b) Post-treatment. c) Profile.

5.2.4 Multilayer Deposition

Usually, pulsed laser deposition [4, 10] was used to grow thin films of high-temperature-superconductive cuprates. We used a high-temperature magnetron sputtering method. Through extensive literature search listed in Table 5.1 and systematic experimental testing shown in Figure 5.8, the deposition was performed with the substrate temperature of 800^0C at a pressure of 20mTorr with 50% oxygen in argon.

	Reference	Film/Substrate	Temperature(C)	Partial Pressure O2	Partial Pressure Ar	Annealing condition	Depositon Rate	Deposition Condition	Quality
Sputtering	JJAP Vol 24, No 4, April 1987	LaSrCuO4/ SrTiO3	700	40mTorr	40mTorr	Aneal in Air at 800C for 8 hours			good
Sputtering	Supercond. Sci. Technol. 12 (1999) 344–347	LaSrCuO4/ SrTiO3	820	130mTorr	520mTorr	annealed at 420C for 20min at 0.8atm O2(600Torr)	25~30 Angstrom/min		good
PLD	APL 102, 112601 (2013)	LaSrCuO4/ SrTiO3	760	32Pa(240mTorr)			2nm/min	4cm between target and substrate	good
PLD	APL 102, 111606 (2013)	LaSrCuO4/ Nb SrTiO3	770	250mTorr		400C for 30min at 400Torr		2J/cm2 and 4Hz	good
PLD	JJAP 50 (2011) 093101	LaSrCuO4/ LaSrAlO4	770	240mTorr		400C for 30min at 400Torr		2J/cm2 and 4Hz	good
PLD	Modern Physics Letter B (2013) 1350005	LaSrCuO4/ Nb SrTiO3	760	32Pa(240mTorr)				4cm between target and substrate,600 mJ in laser energy	good
PLD	Powder Diffraction 28 (S1), September 2013	LaSrCuO4/ SrTiO3	680~760	30Pa(225mTorr)					good

Table 5.1 The literature search for the fabrication condition.

After we found the deposition temperature and pressure, the sample quality was still inconsistent. We suspected there was some position dependency. Through some control experiments, the epitaxial film was found to strongly depend on the relative position between the substrate and the sputtering plasma or target. The off-center deposition was extremely important. In Figure 5.5, the substrate holder was placed 10^0 off from the target and 5 samples were loaded to different positions. These 5 samples were deposited under the same temperature and sputtering pressure. XRD was applied to these 5 samples shown in Figure 5.6 and 5.7. The best epitaxial film was generated from Position 1. There was no epitaxial film in Position 3 and 4 which were directly hit by the plasma. In order to get consistent high-quality film, the substrate holder must be placed 10^0 off from the target and the substrate loaded to Position 1. In MTJ fabrication, the substrate is a rotating 2-inch Si wafer. However, for this high-temperature substrate holder, there is no rotation function and the off-center deposition becomes even more important. The deposition rate was given by low angle XRD measurement shown in Figure 5.8.

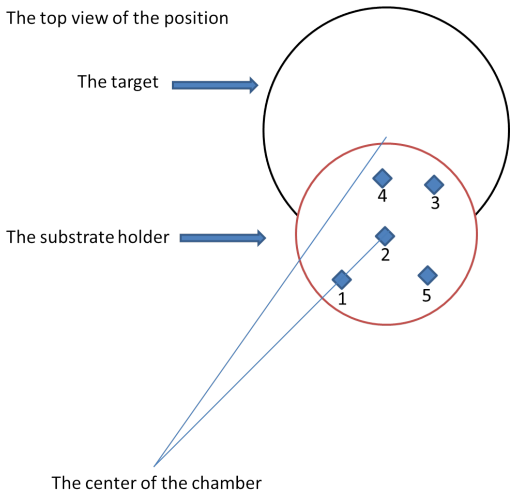

Figure 5.5 The topview of the target and substrate holder. 1,2,3,4 and 5 represent the substrates.

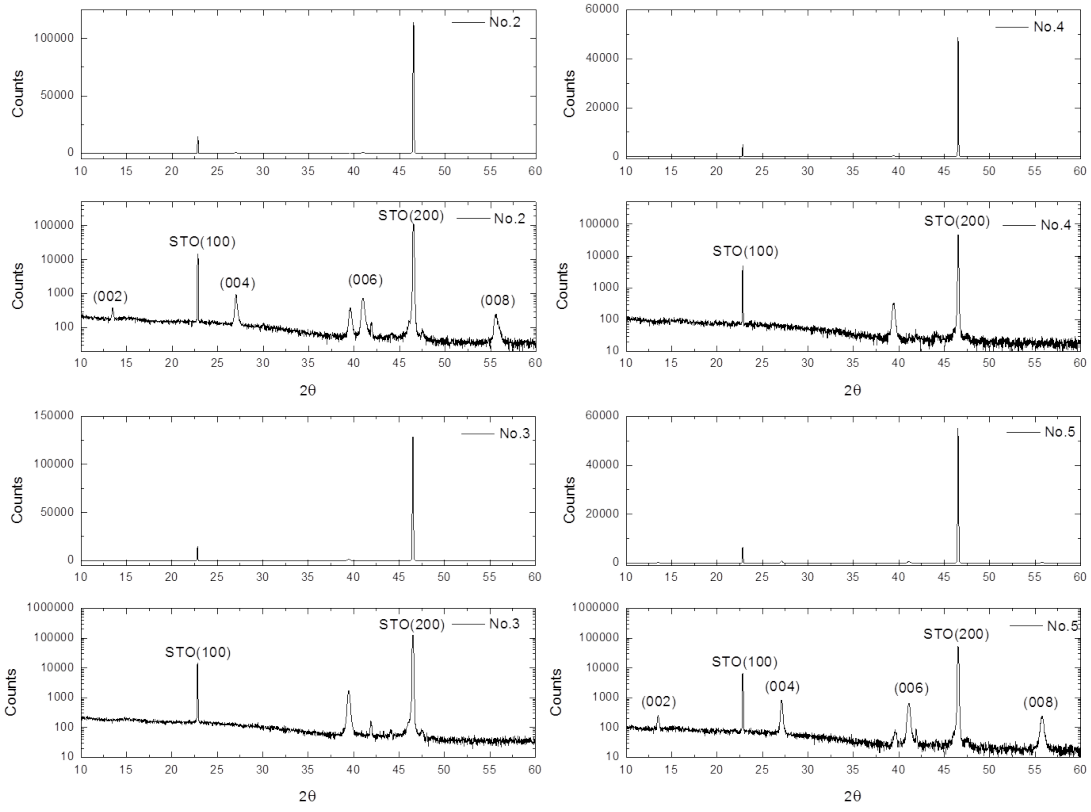

Figure 5.6 The XRD Results for Samples loaded in Position 2, 3, 4 and 5. The results are presented in both linear and logarithmic scale. For all these positions, except the epitaxial peaks, there are always some other peaks.

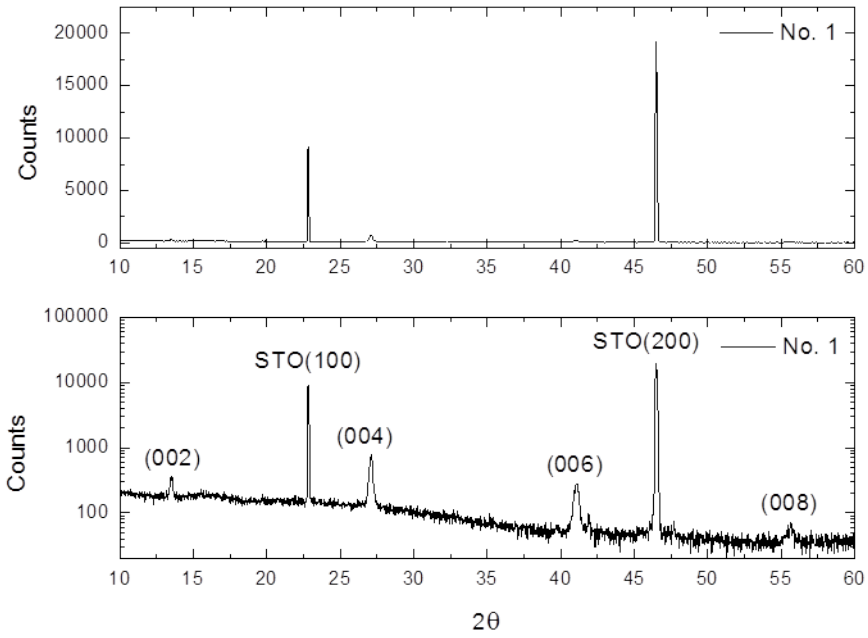

Figure 5.7 The XRD Results for sample loaded in Position 1. In both linear and logarithmic scale, only (00X) peaks showed up. The film deposited is epitaxial.

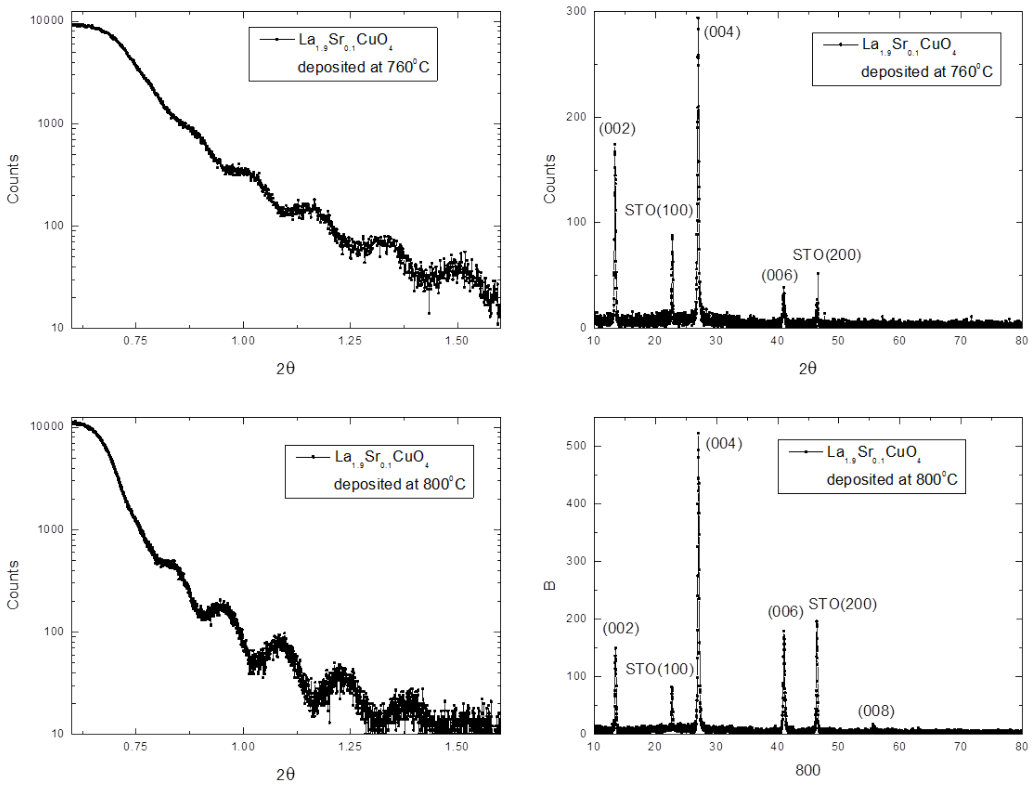

Figure 5.8 The low and high angle X-ray measurement of $La_{1.9}Sr_{0.1}CuO_4$ deposited at 760°C and 800°C.

5.2.5 Thermal Annealing

After the film was deposited using the sputtering system, the sample was actually in the oxygen-deficiency condition. The sample has to be annealed in 450^0C for an hour in air before the deposition of contact leads. Right after the annealing, the sample will be loaded back into the sputtering system for Ti and Au deposition.

5.2.6 Lead Deposition, Photolithography and Ion Milling

In order to keep the interface clean, Ti and Au were first deposited on the LSCO surface. Later photolithography and ion milling methods were applied to create isolated device for

measurement. The lift-off method is prohibited because the surface of LSCO will be first exposed to photoresist and developers. The interface can be contaminated by these chemicals which will make the sample performance hard to explain.

5.3 Characterization of $La_{1.9}Sr_{0.1}CuO_4$ film, 0.5wt% doped Nb $SrTiO_3$ Substrate and their Heterojunctions.

5.3.1 Characterization of $La_{1.9}Sr_{0.1}CuO_4$ film

In order to measure the resistivity and carrier concentration of LSCO film, it was deposited on a treated (001) $SrTiO_3$ single-crystal substrate using the same deposition and annealing condition. Hall bar patterns were brought onto the LSCO thin film through photolithography and ion milling. The measurement was carried out using PPMS from 20K to 300K. In the resistivity measurement shown in Figure 5.9, our material does not exhibit superconducting behavior due to oxygen deficiency. In Figure 5.10, the Hall coefficient slightly decreases with the increase of temperature, while carrier concentration shows the opposite trend.

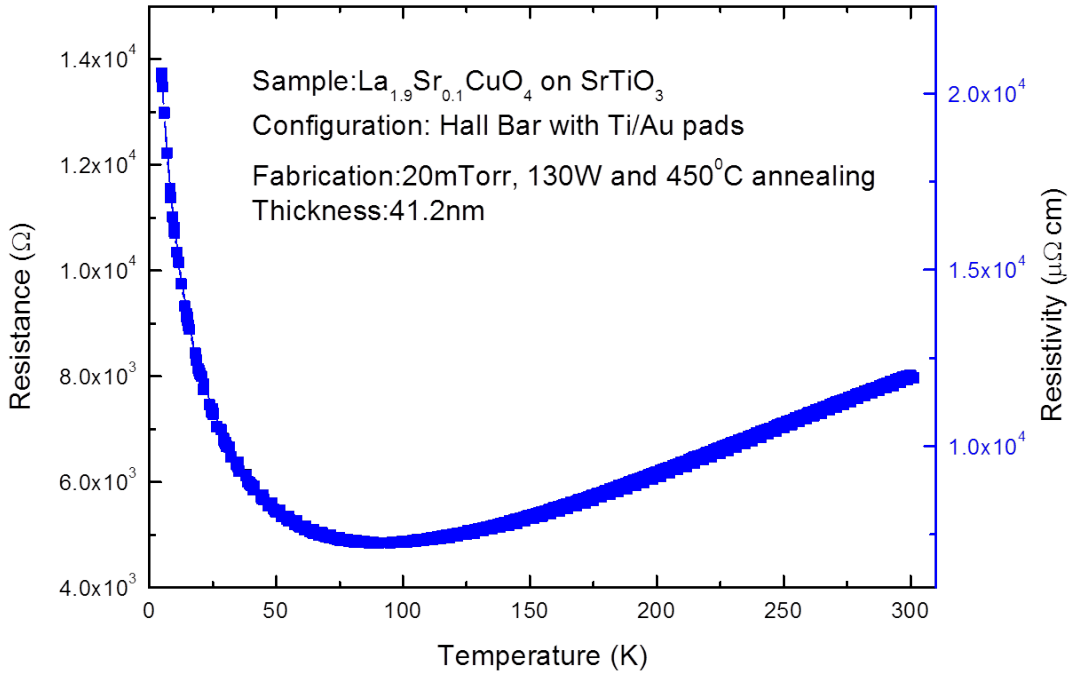

Figure 5.9 The temperature dependency for Resistance of LSCO film on substrate STO. The sample fabrication condition is presented in the figure. The resistivity is calculated based on the resistance, sample thickness and hall bar dimension.

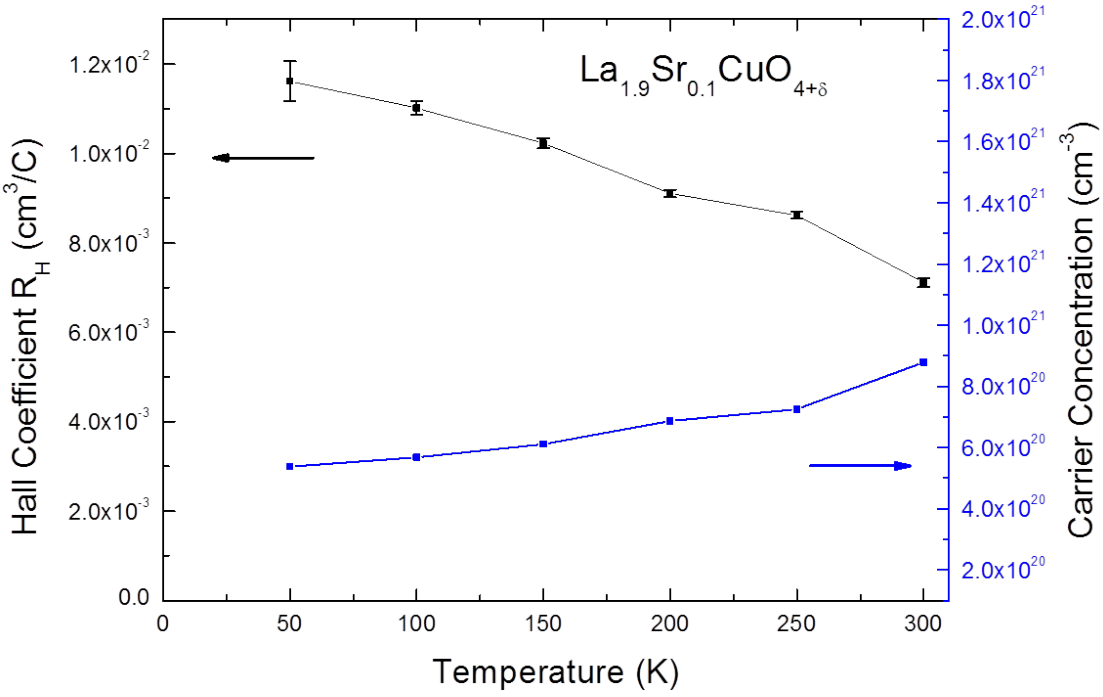

Figure 5.10 The temperature dependency for Hall coefficient and carrier concentration of LSCO film on STO. The Hall coefficient is calculated using $R_H = \frac{V_H t}{IB}$ where V_H is the hall voltage, t sample thickness, B magnetic field applied perpendicular to the sample surface and I longitudinal current. B and I is the applied number when we set up the measurement. V_H is the measured number. The carrier concentration is calculated using $n = \frac{1}{eR_H}$ where e is the charge of electron.

5.3.2 Characterization of 0.5wt% doped Nb $SrTiO_3$ Substrate

Similar studies [11] were conducted for 0.5wt% doped Nb $SrTiO_3$ substrate after treatment. The dimension of the substrate is 5×5×0.5mm. The resistivity and carrier concentration were measured using the Van der Pauw method. The results were presented in Figure 5.12 and Figure 5.13. The resistivity, Hall coefficient and carrier concentration

are almost temperature-invariant, and the negative sign of the Hall coefficient was observed, which is consistent with electrons being the charge carriers.

The resistivity and carrier concentration measured were used to calculate the mobility of the charge carriers using $\rho(T) = \frac{1}{\mu(T) e N_d(T)}$ where ρ is the resistivity, μ is the mobility and N_d is the carrier concentration. The mobility results were presented in Figure 5.11 and Figure 5.14.

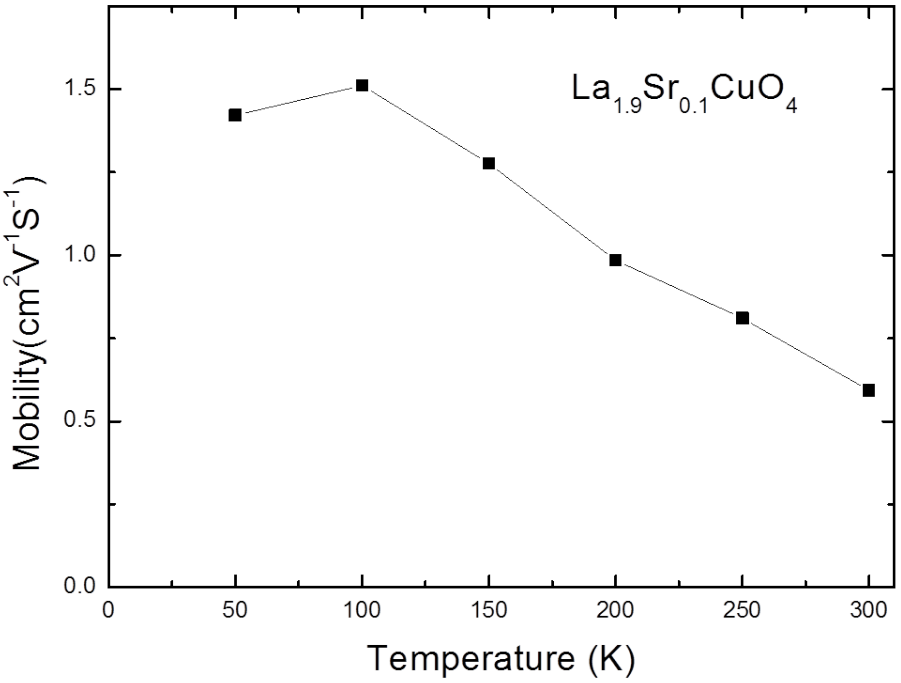

Figure 5.11 The temperature dependency for mobility of LSCO film. This is the same sample presented in Figure 5.9 and Figure 5.10. The mobility is calculated based on the results from Figure 5.9 and Figure 5.10.

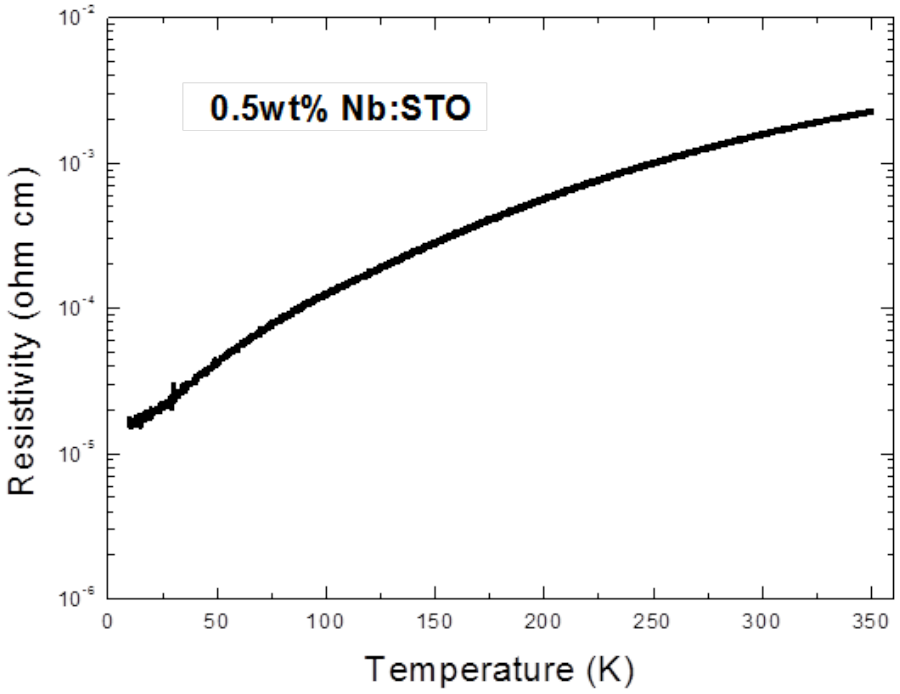

Figure 5.12 The temperature dependency for Resistivity of treated NSTO substrate.

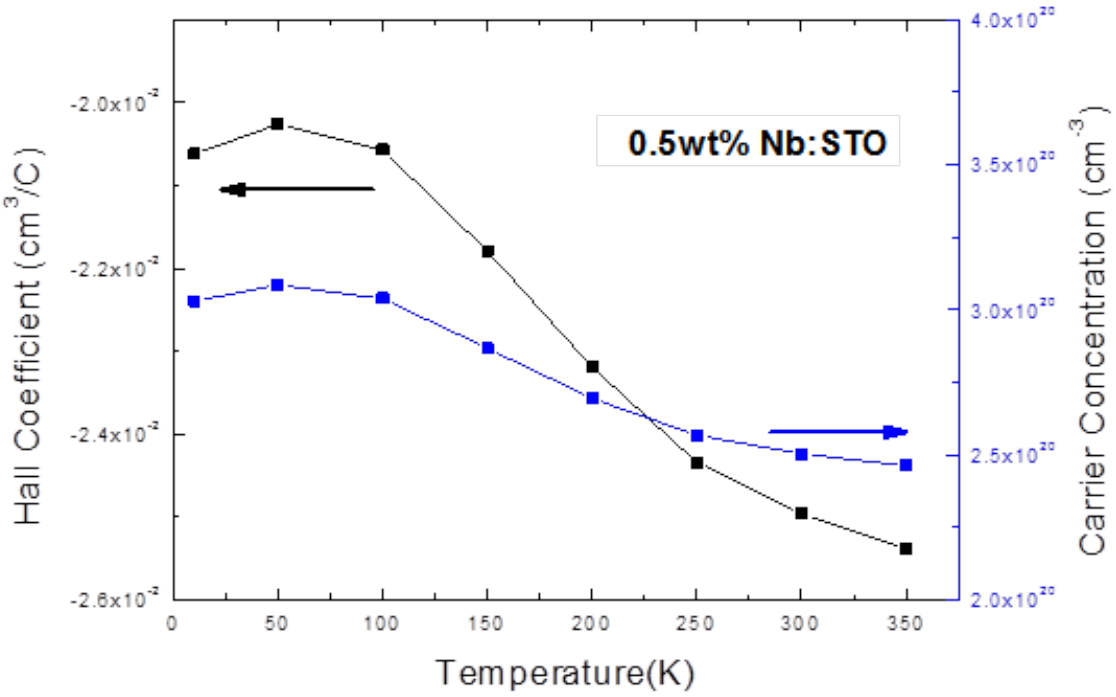

Figure 5.13 The temperature dependency for Hall coefficient and carrier concentration of treated NSTO

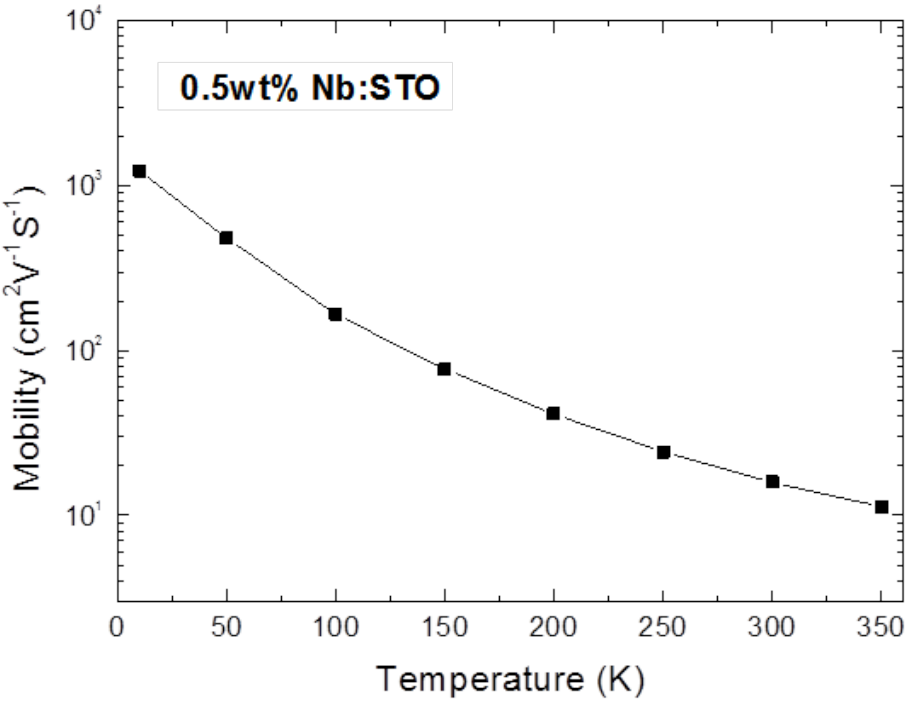

Figure 5.14 The temperature dependency for mobility of treated NSTO substrate.

So far, the epitaxial film of $La_{1.9}Sr_{0.1}CuO_4$ on single crystal (001) $SrTiO_3$ was successfully fabricated and characterized. The treated 0.5wt% doped Nb $SrTiO_3$ substrate was also characterized to get resistivity, Hall coefficient, carrier concentration and mobility. Compared to the results from some other studies, these parameters are consistent. The good quality of these two components gives us confidence in the heterojunctions.

5.3.3 I V Characteristics

Equipment capability has to be checked before we started to measure I-V curves at different temperature. The temperature capability was provided by PPMS. However, the intrinsic resistance mode didn't reach our measurement requirement.

(1) Equipment Set up

The resistant of the heterojunctions varies from 10Ω and 100KΩ under the whole bias voltage range. So we picked up two standard resistant, 10Ω and 20KΩ and measured their I-V curves using both PPMS and Keithley 2400 source meter. The measurement results were presented in Figure 5.15. PPMS result was much worse than the one using Keithley. Therefore, PPMS only provided the temperature environment and I-V measurement was carried by Keithley through the official adaptor from Quantum Design Company.

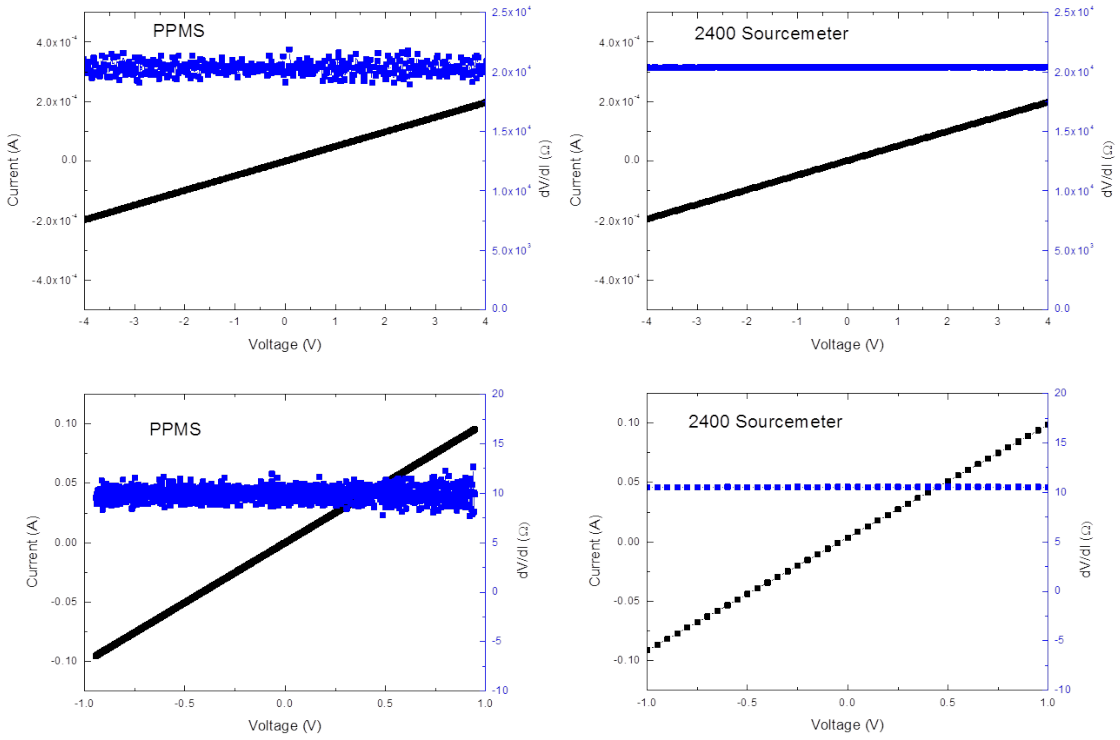

Figure 5.15 The comparison between PPMS and 2400 source meter measuring the standard resistant 20KΩ and 10Ω. For 20KΩ, PPMS measurement showed a lot of fluctuation. Since our junction resistance can vary from 10Ω to 100KΩ and requires that equipment's stable performance over the whole range, Keithley 2400 is the better choice.

(2) Measurement Mounting

The sample is mounted on the PPMS holder shown in Figure 5.16. According to the sign of Hall coefficient which has been measured earlier, LSCO film is actually p-type and the substrate is n-type. Therefore, positive voltage was applied to the top electrode neighboring the LSCO film and negative voltage was applied to the bottom electrode neighboring the substrate. All the connections were realized by wire bonding.

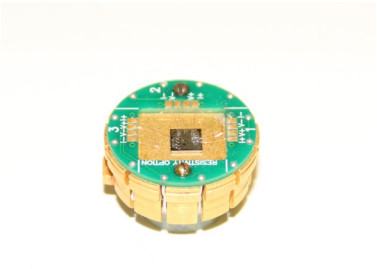

Figure 5.16 Sample Mounting. The sample was placed on PPMS holder using silver paste. Connections were realized through wire bonding.

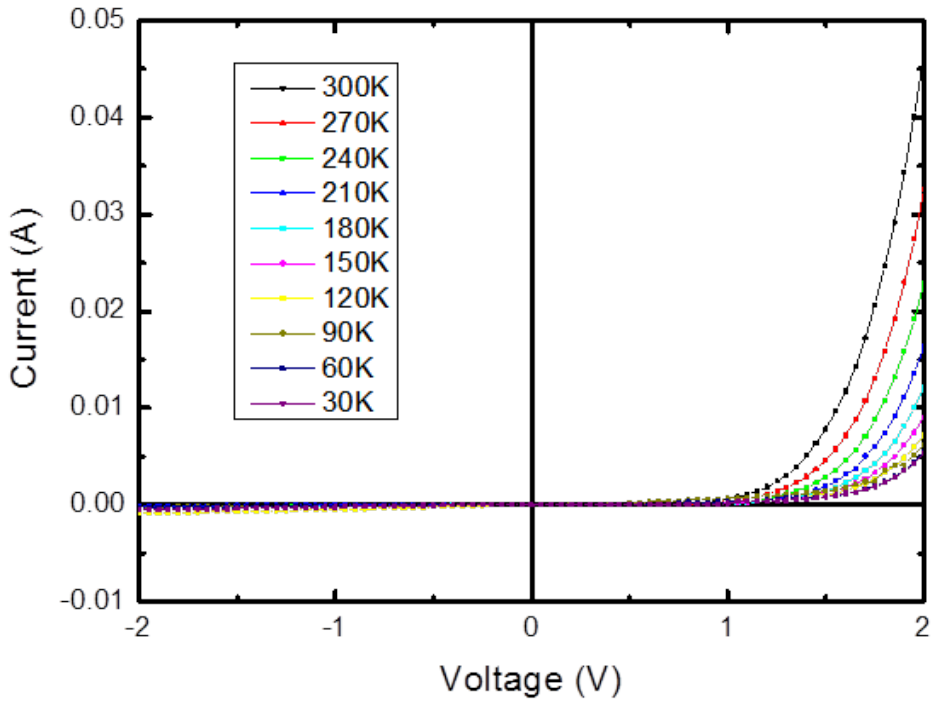

Figure 5.17 One example of I-V curves of LSCO/NSTO at different temperatures. During the measurement, the voltage started from 0, increased to +2V, then decreased to -2V and went back to 0. The corresponding current was recorded.

(3) Discussion

Figure 5.17 showed the heterojunctions had strong rectifying capability at different temperature. The turn-on voltage increased with temperature decreasing. According to the resistivity and hall coefficient we measured earlier, LSCO is metal and NSTO is n-type semiconductor. The heterojunction of LSCO and NSTO can be treated as a Schottky barrier and conventional thermionic emission theory is applied to characterize it. The forward current for the junction is described using the following equation:

$$I = I_0 e^{\frac{eV}{NkT}}$$

N is the non-ideality constant.

$$I_0 = AA^0T^2e^{\frac{e\phi_B}{kT}}$$

A, A^0 and k are sample area, the Richardson constant ($1.202\times10^6 Am^{-2}K^{-2}$) and Boltzmann constant. ϕ_B is the Schottky Barrier height. I_0 is called the reserve saturation current, which is a direct indictor of the quality of junctions.

The similar measurement in Figure 5.17 was carried out for another three heterojunctions. Schottky Barrier height ϕ_B and non-ideality constant N was extrapolated using the equation $I = I_0 e^{\frac{eV}{NkT}}$. Schottky Barrier height ϕ_B was observed to decrease with temperature. By doing quadratic fitting, the following equations were obtained:

$\phi_{B1} = -6.48\times10^{-7}T^2+2.45\times10^{-3}T+3.27\times10^{-18}$

$\phi_{B2} = 5.96\times10^{-6}T^2+3.95\times10^{-4}T+2.98\times10^{-2}$

$\phi_{B3} = 2.87\times10^{-6}T^2+1.18\times10^{-3}T+9.55\times10^{-3}$

The temperature dependency of non-ideality constant was also obtained. The room temperature non-ideality constant N is 2.7, 3.7 and 5.3 for these three junctions. The value is significant from the ideal junction, but these have been observed in those doped semiconductor junctions. This could be due to the barrier inhomogeneity [12] and interface states [13]. For our heterojunctions, non-ideality constant was observed to increase with temperature decreasing shown in Figure 5.19. It was observed to satisfy the empirical equation $N=1+T_0/T$. By fitting our measurement, we can get $N_1=2323/T+1$, $N_2=7106/T+1$ and $N_3=2822/T+1$.

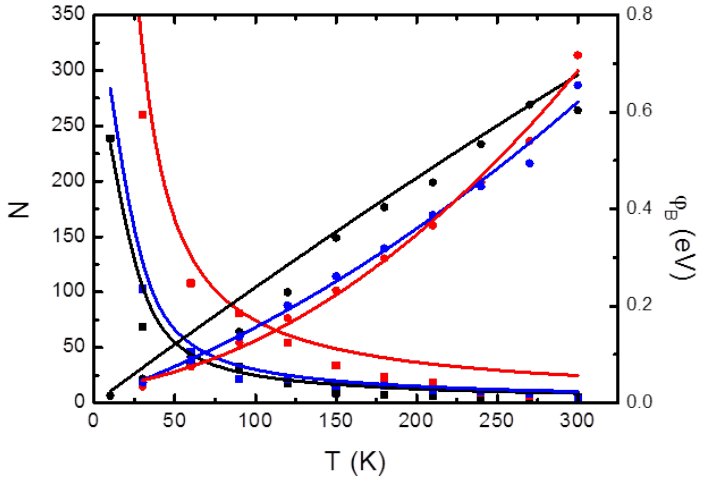

Figure 5.18 The non-ideality constant N and Schottky Barrier height ϕ_B were extrapolated and presented from the temperature-dependent I-V curve of three independent junctions.

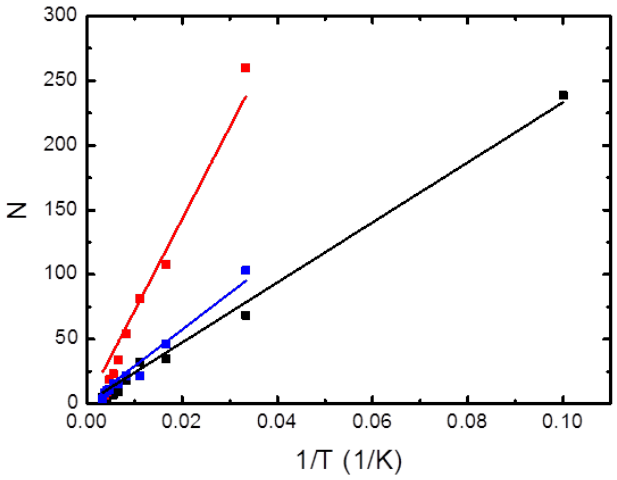

Figure 5.19 The dependence of non-ideality constant N on temperature. N is proportional to the reciprocal of temperature T for these three independent junctions.

(4) Correlation Study

At room temperature, heterojunctions under different fabrication condition were characterized using I-V curve method. For the best heterojunction we found, the non-ideality factor was 2.0 and the reserve saturation current I_0 was only 1.6×10^{-12}A. The reverse saturation current I_0, resistance R at 0 bias voltage and non-ideality constant N were extrapolated and presented in Table 5.2. The universal area resistance RA was used to get rid of the sample area difference. The correlation study showed the junctions with large resistance intended to give low reverse saturation current. By fitting the measurement, the correlation between I_0 and RA was obtained following $\log(I_0)=2.49-1.04\times\log(RA)$. Similarly non-ideality constant was observed to be small for the junctions with low reverse saturation current. The empirical equations, $N=8.70+0.68\times\log(I_0)$ and $N=9.48-0.58\times\log(RA)$, were obtained for our measurement. The significance for this correlation study is for the operation. Only through measuring the junction resistance in the low bias voltage region, its non-ideality constant and reverse saturation current can be

estimated. This will protect the heterojunctions from exposing them to large bias voltages and quickly find out the quality of heterojunctions.

In Table 5.2, the characteristics of heterojunctions were observed to be affected by the ion milling process. Ion milling was the last step to create isolated dot-shape heterojunctions. The ion milling depth was carefully calibrated and well controlled. The heterojunctions with good I-V characteristics went through over etching and intensive side-wall cleaning procedure. The possible reason could be the impurities and contamination on side wall of the heterojunctions or on the substrate were removed during this over etching process.

	Dot Number	R at 0V (Ω)	RA (Ω*μm^2)	I_0 (A)	N
Under Etching	5	7.9×10^{6}	2.48×10^{11}	3.4×10^{-9}	2.5
	13	5.5×10^{5}	1.73×10^{10}	6.2×10^{-8}	3.6
	3	7.0×10^{4}	2.20×10^{9}	2.5×10^{-7}	4.3
	6	2.8×10^{4}	8.79×10^{8}	5.6×10^{-7}	4.9
Just Right	14	8.2×10^{6}	2.57×10^{11}	3.8×10^{-9}	3.2
	12	4.3×10^{6}	1.35×10^{11}	1.0×10^{-8}	3.1
	6	7.2×10^{6}	2.26×10^{11}	4.6×10^{-9}	3.0
	3	1.1×10^{5}	3.45×10^{9}	9.2×10^{-9}	3.0
Over Etching	5	1.4×10^{7}	4.40×10^{11}	2.8×10^{-9}	2.9
	6	1.3×10^{7}	4.08×10^{11}	3.4×10^{-9}	3.1
	9	2.3×10^{6}	7.22×10^{10}	1.4×10^{-8}	3.2
	7	9.6×10^{5}	3.01×10^{10}	1.1×10^{-9}	3.4
More Over	4	1.9×10^{8}	5.97×10^{12}	2.1×10^{-10}	2.2
	10	5.1×10^{7}	1.60×10^{12}	5.1×10^{-10}	2.0
	5	2.2×10^{7}	6.91×10^{11}	1.4×10^{-9}	2.3
	11	1.0×10^{6}	3.14×10^{10}	3.7×10^{-8}	3.3
	new1	2.2×10^{8}	6.91×10^{12}	1.69×10^{-10}	2.17
	New 2	2.4×10^{8}	7.54×10^{12}	1.53×10^{-10}	2.15

Table 5.2 Resistance at 0 bias voltage, RA constant, reverse saturation current and non-ideality constant were presented for junctions under different ion milling conditions.

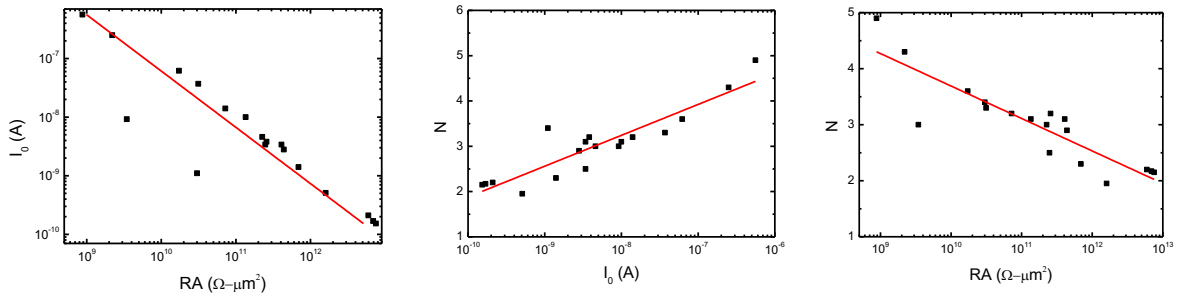

Figure 5.20 Correlation study for I_0, RA and N.

5.3.4 C F Characteristics

The room temperature C-F characteristics of LSCO on NSTO junction measured under different bias voltages were measured and presented in Figure 5.21. For each bias voltage, capacitance was measured with frequency changing from 40Hz to 0.5MHz with 50mV oscillation amplitude. In Figure 5.21 the direct capacitance distribution was presented in a contour plot.

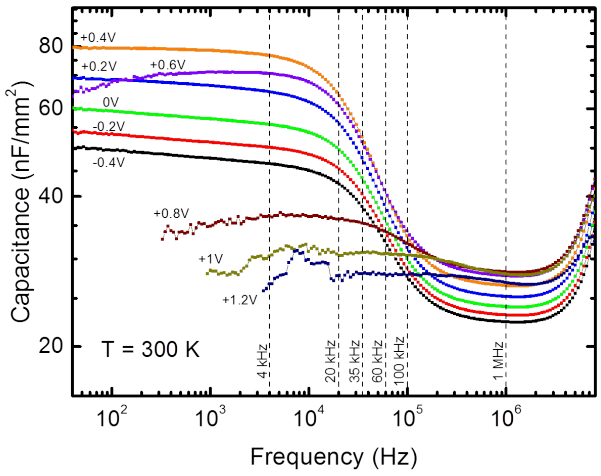

Figure 5.21 C-f characteriscs of a LSCO/NSTO heterojunction at different bias voltages. It was measured using Agilent 4292A Impedance Analyzer shown in Figure 5.23. The junction was set under certain bias voltage and went through c-f scan. The frequency was presented in the logarithmic scale.

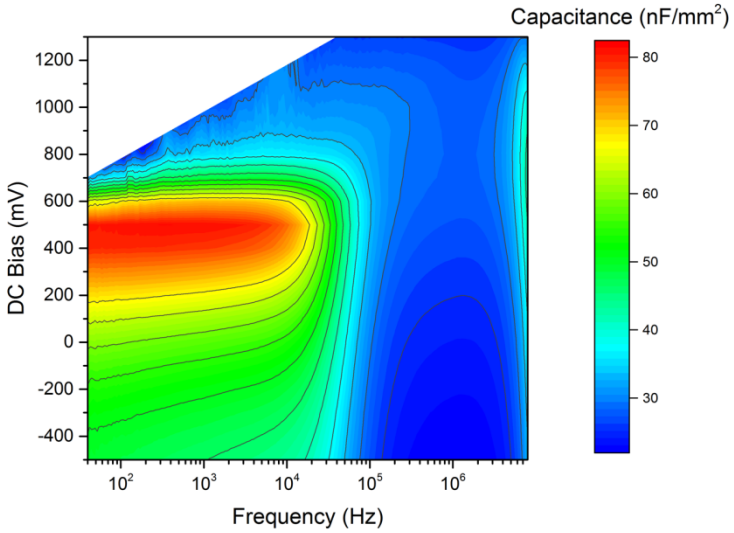

Figure 5.22 Capacitance contour plot versus DC bias and frequency.

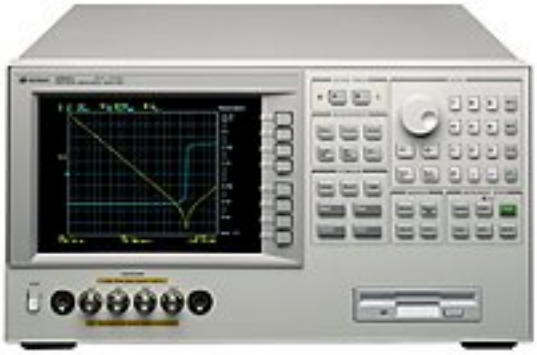

Figure 5.23 The image of Agilent 4292A Impedance Analyzer

During the measurement, the sample was fixed on the breakout board and placed in a sealed metal box. The electronic wires and connectors are all specific for high frequency measurement. The wires have to be as short as possible. Before connecting the sample in the measurement circuit, the rest circuit has to be measured and calibrated. Agilent

4292A has the capability of removing the contribution by these connecting wires and provide accurate results only contributed by the sample.

In Figure 5.21, the capacitance is clearly frequency-dependent under all bias voltages. This could be explained by considering this heterojunction as a Schottky barrier with deep-level impurities [14]. Basically the heterojunction's capacitance is contributed from two kinds of capacitances. One is the conventional depletion capacitance and the other is the capacitance due to the deep-level impurities. In the low frequency range, these two capacitances both contribute. In the high frequency range, the capacitance due to the deep-level impurities gets lower and depletion capacitance dominates. According to the study [14], the frequency-dependent capacitance for a Schottky barrier with deep-level impurities can be expressed as $C = C_{hf} + \frac{C_{lf} - C_{hf}}{1+\omega^2\tau_{ef}^2}$ where C_{hf} is the capacitance in high-frequency limit, C_{lf} is the capacitance in low-frequency limit and τ_{ef} is the effect time constant. The fitting results are presented in Figure 5.24. In the room temperature, C_{lf} of the heterojunction is strongly dependent on the bias voltage while C_{hf} is relatively constant with different bias changing.

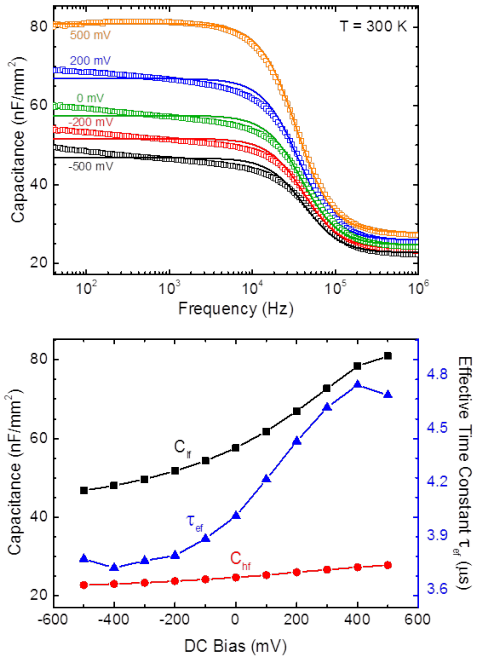

Figure 5.24 The upper image: measured capacitance and fitting value versus frequency at difference DC bias voltages; The lower image: C_{hf}, C_{lf} and τ_{ef} obtained from the fitting versus DC bias voltage.

In the reverse bias region of a Schottky barrier, the capacitance can be calculated using the equation $\frac{1}{C^2} = \frac{2}{A^2}\frac{V_d - V}{q\varepsilon_0\varepsilon N}$ if the junction area A, the permittivity ε and the carrier density N of the semiconductor, the diffusion potential at zero bias V_d are available. In the reverse bias range, a C^{-2} -V plot at 4KHz and 20KHz frequency were presented in Figure 5.26. Through fitting the curve using $\frac{1}{C^2} = \frac{2}{A^2}\frac{V_d - V}{q\varepsilon_0\varepsilon N}$, the diffusion potential was obtained. At 4KHz V_d was 0.86V while V_d was 1.08V at 20 KHz. This indicated the diffusion potential was also frequency-dependent.

In the forward bias region of a Schottky barrier, the capacitance becomes difficult to explain or even measure because there is large shunt conductance existing in the barrier. In Figure 5.25, bias voltage-dependent capacitance was extrapolated for each frequency. The capacitance clearly decreases with frequency increasing. As we mentioned earlier, it is due to the relaxation mechanism. There is capacitance peak in the forward region in Figure 5.25. It can be explained by considering the Schottky barrier with deep-level impurities and the series-resistance effect [15]. For the junction in the forward bias, in the low frequency region, not only the depletion capacitance and the capacitance due to deep level impurities have to be considered, but also an insulator capacitance. In the high frequency region, only the depletion capacitance and the insulator capacitance will contribute.

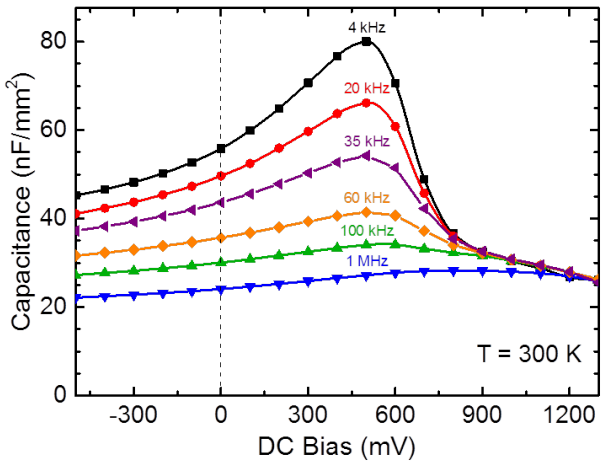

Figure 5.25 C-V plots at different frequencies.

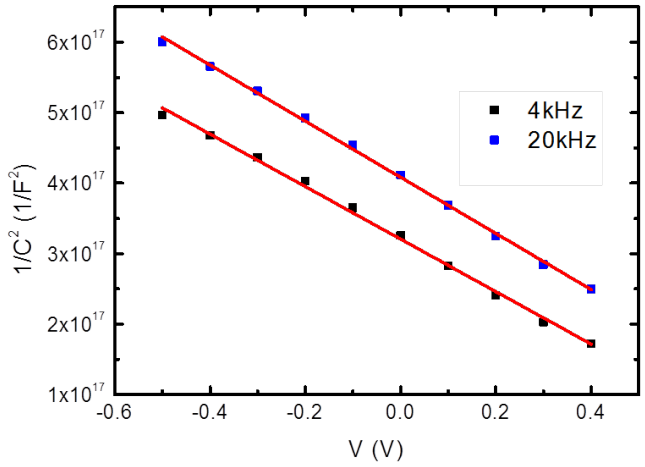

Figure 5.26 $1/C^2$ –V plots at f = 4 kHz and f= 20 kHz

5.4 Commercial Schottky Diode and Single-crystal Solar Cell

The high-performance Schottky diode, SDM40E20LA from the Diodes Incorporated Company, and one monocrystalline silicon solar cell were also studied for comparsion. The normalized capacitance is presented in Figure 5.27. For the Schottky diode, the capacitance is also frequency-dependent and systematically increases with the forward bias voltage. The performance of the common monocrystalline silicon solar cell shows similar frequency-dependent capacitance characteristics as our heterojunctions. The high-performance Schottky diode is homogeneous and there is no frequency dependent for capacitance. In Figure 5.8, for both the commercial Schottky diode and the solar cell, their capacitances increase in the forward bias region. This is completely different from our LSCO/NSTO heterojunction.

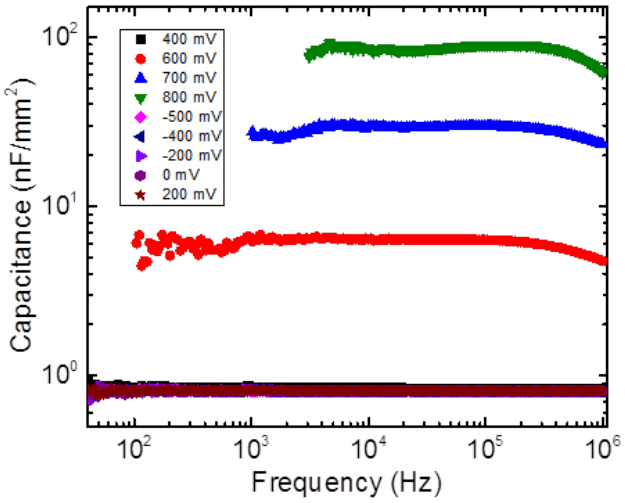

(a) Commercial Schottky Diode

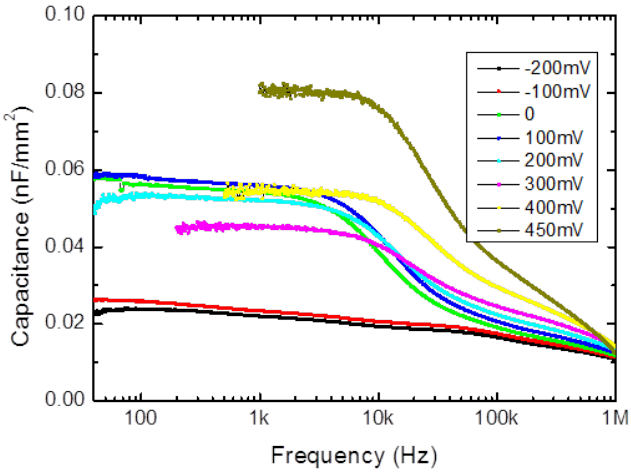

(b) Single-crystal Solar Cell

Figure 5.27 (a) C-f curves of Commercial Schottky Diode under different bias voltages. (b) C-f curves of solar cell under different bias voltages.

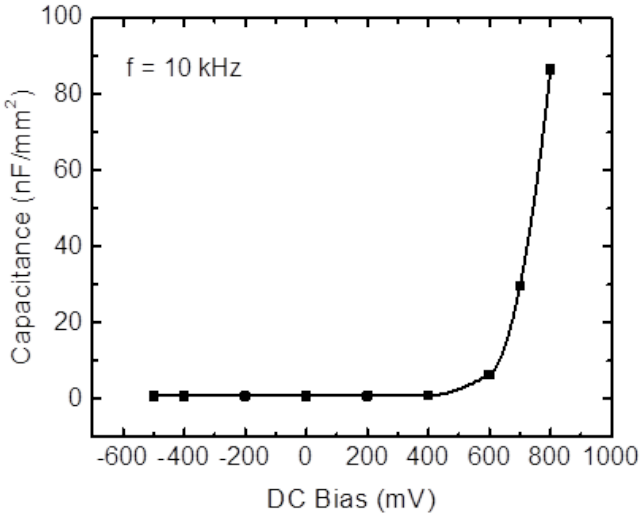

(a) commercial Schottky diode

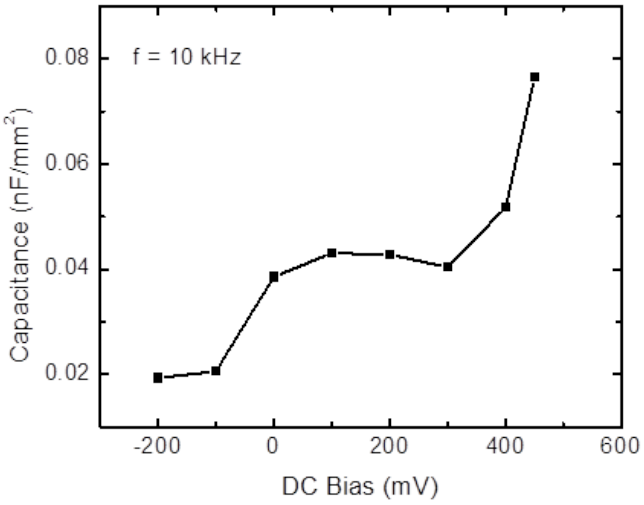

(b) commercial solar cell

Figure 5.28 (a) C-V curve of commercial Schottky diode at f =10kHz. (b) C-V curve of commercial solar cell at f = 10kHz.

5.5 Conclusion

We successfully achieved the synthesis of high-quality heterojunctions of epitaxial $La_{1.9}Sr_{0.1}CuO_4$ thin films on a 0.5wt% Nb doped $SrTiO_3$ single-crystal substrate using high temperature magnetron sputtering system. In the absence of the superconductivity, our heterojunctions show good rectification and expected temperature dependency. At room temperature, we have investigated the capacitance of the junctions over a broad frequency range and bias voltage range. The results were explained by considering the LSCO/NSTO junctions as a Schottky barrier with deep-level impurities. This doped Mott insulator system is quite different from traditional p-n heterojunctions and exhibited interesting interfacial properties. Our work has built a foundation for the further development of Mott insulator-based junctions as viable high frequency diodes and solar rectification energy conversion devices.

Reference

1. E. Manousakis, Physical Review B **82** (12), 125109 (2010).

2. F. C. Sabou, N. Bodington and J. Marston, presented at the Lester Eastman Conference on High Performance Devices (LEC), 2012 (unpublished).

3. J. Shi, Y. Zhao, H. Zhang and X. Zhang, Applied Physics Letters **92** (13), 132501 (2008).

4. Y. Zhang, P. Li, G. Wang, Y. Xing, D. Wu, J. Shen, M. Lei and W. Tang, Applied Physics Letters **102** (11), 112601 (2013).

5. J. Sun, C. Xiong, Y. Zhang and B. Shen, Applied Physics Letters **87** (22), 222501 (2005).

6. G. Rietveld, M. Glastra and D. Van der Marel, Physica C: Superconductivity **241 (**3-4), 257 (1995).

7. K. Sreedhar and P. Ganguly, Physical Review B **41** (1), 371 (1990).

8. M. Kawasaki, K. Takahashi, T. Maeda, R. Tsuchiya, M. Shinohara, O. Ishiyama, T. Yonezawa, M. Yoshimoto and H. Koinuma, Science, 1540 (1994).

9. G. Koster, B. L. Kropman, G. J. Rijnders, D. H. Blank and H. Rogalla, Applied Physics Letters **73** (20), 2920 (1998).

10. B.-S. Li, A. Sawa and H. Okamoto, Applied Physics Letters **102** (11), 111606 (2013).

11. K. Rana, V. Khikhlovskyi and T. Banerjee, Applied Physics Letters **100** (21), 213502 (2012).

12. J. H. Werner and H. H. Güttler, Journal of applied physics **69** (3), 1522 (1991).

13. W. Ramadan, S. Ogale, S. Dhar, L. Fu, S. Shinde, D. C. Kundaliya, M. Rao, N. Browning and T. Venkatesan, Physical Review B **72** (20), 205333 (2005).

14. Y. Zohta, Solid-State Electronics **16** (9), 1029 (1973).

15. P. Chattopadhyay and S. Sanyal, Applied surface science **89** (2), 205 (1995).

Chapter 6
Conclusion

MgO-barrier magnetic tunnel junction has been widely used in spintronics industry, for example information storage devices and thin film magnetic sensors. However, the application of MgO-barrier MTJ sensors is limited by its sensing capability. We have systematically studied different MgO-based MTJ multilayer structures. Each thin-film layer's contribution to the MTJ performance has been isolated and improved. MTJs with large tunneling magnetoresistance ratios (TMR) have been successfully fabricated using a magnetron sputtering system through the optimization of layer structures. The geometry of the MTJ sensor and magnetic annealing process has also been optimized.

The magnetic flux concentrator is introduced into our MTJs to significantly increase the magnetic sensing capability. Thin films of a special "soft" magnetic material ($Co_{88}Nb_8Zr_4$) has been successfully fabricated utilizing our high vacuum magnetron sputtering technique, and characterized using magnetometry measurement. The permeability of as-deposited $Co_{88}Nb_8Zr_4$ can reach 5000 and there is no obvious coercivity from VSM measurement. The magnetic flux concentrators have been added to the MTJ using lithography techniques. The sensitivity has been increased to 20%/Oe and the coercivity reduced to 0.3Oe. Furthermore, we have included additional magnetic concentrators, made by $Ni_{77}Fe_{14}Cu_5Mo_4$, outside of the MTJ devices. With these approaches, we have increased the magnetic sensing capability of the MTJs significantly. The sensitivity of our new MTJ sensor can reach 557%/Oe.

Based on the same magnetron sputtering technique, we have successfully developed high-quality heterojunctions of epitaxial $La_{1.9}Sr_{0.1}CuO_4$ (LSCO) thin films on a 0.5wt% Nb doped $SrTiO_3$ (NSTO) single-crystal substrate. In order to make this junction, we modified our sputtering system and installed a high temperature substrate holder inside the chamber. During the sputtering the substrate can be heated up to 950^0C and this further improves our fabrication capability. We made the $La_{1.9}Sr_{0.1}CuO_4$ target using the traditional solid state reaction method and the quality of our target were verified by XRD. Before we start to characterize the fabricated heterojunctions, these two materials have been made in the same fabrication condition and characterized. The heterojunction shows good rectification and expected temperature dependency. We have investigated the capacitance of the junctions over a broad frequency range and bias voltage range. The results were explained by considering the LSCO/NSTO junctions as a Schottky barrier with deep-level impurities. This doped Mott insulator system is quite different from the traditional p-n heterojunctions and exhibited interesting interfacial properties.